Towards Personalized Cancer Therapy: Microfluidic Approaches for Drug Screening

Chi-Ting Chang

A dissertation

submitted in partial fulfillment of the

requirements for the degree of

Doctor of Philosophy

University of Washington

2014

Reading Committee:

Albert Folch, Chair

Barry Lutz

Raymond J. Monnat Jr.

Program Authorized to Offer Degree: Bioengineering

University of Washington

Abstract

Towards Personalized Cancer Therapy: Microfluidic Approaches for Drug Screening

Chi-Ting Chang

Chair of the Supervisory Committee:

Professor Albert Folch

Department of Bioengineering

The ability to predict a patient's response to chemotherapy is a major challenge in oncology. Despite the years of research and development with countless investments, clinical trials in oncology still experience high failure rates, resulting in patients suffering from severe side effects with little benefits. Therefore, there is a critical need to tailor chemotherapies to individual patients. Personalized approaches could lower treatment toxicity, improve patients' quality of life, and ultimately reduce mortality. In order to pursue personalized chemotherapy, advanced technologies and tools are urgently needed.

One of the major challenges in oncology is tumor heterogeneity from individual patients. To demonstrate the potential for quantifying tumor heterogeneity, we developed a simple approach by using a user-friendly microwell array device to allow for tracking key cell behaviors from large numbers of single cells. We demonstrated the utility of these arrays by quantifying the proliferation and senescence of isogenic cells which expressed or had been depleted of the human Werner syndrome protein. Our results allowed us to reveal and quantify cell-to-cell heterogeneity in proliferation and senescence during clonal growth.

Current drug testing assays are either based on cell lines, which enable high-throughput screening but lack the physiological relevance of the tumor microenvironment, or xenograft models which are time- and resource-intensive and may lack important tumor components. As a result, drug candidates that emerge from drug screening cannot accurately predict how drugs act in patients to select the best possible treatment. Therefore, we propose to use intact tissue slices and biopsies which preserve the tumor microenvironment for drug screening. To allow for testing large numbers of compounds on intact tissues, we developed a microfluidic device that integrates live tissue slice cultures with an intuitive multi-well platform that allows for exposing the slices to multiple compounds at once or in sequence.

In order to demonstrate our microfluidic platform, we performed the response of live mouse brain slices to a range of drug doses in parallel. Drug response was measured by imaging of markers for cell apoptosis and for cell death and was quantified by the fluorescence intensity and cell counts from epifluorescence and confocal microscopy images, respectively. We further extended the application by producing tumor slices and biopsies from mouse xenografts to demonstrate selevtive drug testing on mouse xenograft slices. Our drug testing results demonstrated the feasibility to allow for identifying the subset of therapies of greatest potential value to individual patients, on a timescale rapid enough to guide therapeutic decision-making.

Acknowledgements

This work would not have been established without many support. I want to first thank my advisor, Dr. Albert Folch, for giving me the opportunity to work in his lab and providing valuable experience and knowledge during my PhD process. In addition to my lab experience, I want to thank Dr. Albert Folch again for giving me a chance to work on this exciting and meaningful project. In this collaborative work, I was very pleased to have two fantastic mentors, Dr. Raymond Monnat Jr. and Dr. Robert Rostomily, who provided me me resources and gave me guidance to move the project forward. I would also like to thank both Dr. Albert Folch and Dr. Raymond Monnat Jr. for their vision in using intact tissues for cancer diagnostics and their constant source of support, knowledge, and encouragement. I would like to thank for my other committee members, Dr. Jean Campbell, Dr. Burry Lutz, and Dr. Deok-Ho Kim for their guidance and expertise to help me through the PhD process. Additionally, I would like to thank Dr. Andrei Mikheev for supporting the xenograft materials and Dr. Nirveek Bhattacharjee for being a good mentor in the lab.

There are too many to thank individually, but I would like to thank all Folch lab members who not only helped me through my PhD, but made my graduate school experience memorable. In addition to my experience in the lab, I would like to thank all my close and lifelong BIOE friends who made my last 6 years enjoyable outside of the lab. I would like to thank my family for the massive support. Lastly, I would like to give very special thanks to my fiancée, Elizabeth Montgomery, for giving me encouragement and making the last few years of my life so special.

Table of Contents

List of Figures

Chapter 1. Introduction and Summary

1.1 Motivation and Significance

In 2014, approximately 1,700,000 new cancer cases are expected to be diagnosed, and about 600,000 Americans are expected to die of cancer [1]. The treatment options for cancer patients are limited to surgery, radiation, and chemotherapy, used alone or in combination. Among these treatments, chemotherapy, either with traditional cytotoxic drugs or newer targeted drugs, is the final option of treatment for the patients. Currently, high-throughput compound screening to identify drug candidates is mostly based on two-dimensional (2D) cell culture systems. On average, the development of a single drug costs a pharmaceutical firm more than 800 million dollars [2]. However, about 95% of potential therapeutic agents demonstrate insufficient anticancer activity in clinical trials, resulting in a significant waste of time and money [3].

In addition to the complexity of this disease, many additional factors are also responsible for the high failure rate in the development of anticancer drugs and the inaccuracy in predicting drug responses in patients. One of the major factors is the use of cell line and mouse models as drug screening tools in an attempt to predict efficacy in humans, which may be inadequate and fundamentally flawed [4]. Moreover, these pre-identified agents entered into clinical trials may not only show ineffective responses but also expose patients to risks from toxic compounds, waste their time, and decrease their quality of life during the treatment. A major potential problem which has been identified with existing cell lines and mouse xenograft models is the lack of a tumor microenvironment compared to the original tumors [5]. The cell lines enable high-throughput screening but lack the physiological relevance of the tumor microenvironment. On the other hand, xenograft models which are time- and resource-intensive, and may lack other important tumor components such as host-derived microvasculature, immune cells and stromal cells.

The National Cancer Institute has identified that “current methods to assess potential cancer treatments are cumbersome, expensive, and often inaccurate” [6]. Due to the inadequacies of these existing models, there is an urgent need for the development of

more robust and practical drug screening techniques for preclinical testing and drug development. Ideally, these new techniques should significantly reduce development costs, obtain and quantify the results rapidly, and improve the accuracy of the predictions. In order to address these techniques, the focus of this thesis is to develop novel techniques for drug testing by using microfluidic technologies. With the existing understanding of cancer biology, our approaches and goals have the potential to improve beyond current drug testing models, and ultimately benefit cancer patients.

1.2 Summary

The purpose of the work presented in this dissertation is to advance current cancer drug testing models using microfluidic technology. Chapter Two provides sufficient background related to current drug testing models, the tumor microenvironment, and the techniques which allow for retention of the tumor microenvironment for improved drug testing models. Chapter Three demonstrates a simplified version of a clonogenic assay using a microwell array device with potential applications in the study of the tumor heterogeneity on single cell clonal behaviors. Chapter Four focuses on the methods and techniques for *ex-vivo* intact tissue culture, which preserves the original cellular architecture. Chapter Five focuses on a new microfluidic platform that integrates with the *ex-vivo* intact tissue culture for high-throughput drug screening. We explicitly describe the fabrication techniques, explain the theory behind the technology, and experimentally demonstrate the novel integration of a microfluidic device and the organotypic tissue slice culture. Chapter Six focuses on the complete method of utilizing our microfluidic device for high-throughput drug screening. We demonstrated parallel drug testing on an intact tissue slice, data acquisition, and quantitation and analysis in detail. Chapter Seven focuses on a patient-derived glioblastoma xenograft model. We generated tumor slices from a xenograft tumor for drug testing and then used microfluidic device to demonstrate proof-of-concept with the xenograft model. Finally, chapter Eight focuses on the limitations and future directions of this work from the aspects of device technology and medicine.

1.3 Major Contribution in This Thesis

We propose a method to directly use patient tumor samples, in the form of tumor biopsies or tumor slices under organotypic culture for drug screening. We have developed a microfluidic device which allows for large–scale drug testing on intact tissue with the goal of producing more physiologically relevant testing results compared to existing *in-vitro* models. Our approach has the potential to improve upon current personalized drug testing systems to more accurately inform doctors about the best drug candidate for a given patient. Furthermore, this approach is of particular interest to pharmaceutical companies because it allows for the analysis of meaningful samples taken directly from patients with different types of tumors, in a short period of time and with less labor. The use of our approach should accelerate the progression of potential new chemotherapeutic agents to clinical trials. In addition, this approach may also be applied to the future drug development from the laboratories of pharmaceutical companies to help to shorten development time and to make clinical trials both more efficient and safer for patients.

Chapter 2. Background

2.1 Motivation

The majority of cancer patients have to suffer through a chemotherapy treatment as a last attempt to battle the disease and prolong their lives. As the fact stands, the drugs given to these patients do not provide long-term benefits and are often chosen without fully calibrating the outcomes. This "blind" treatment results in patients suffering serious side effects from the drugs with minimal efficacy. To improve upon the current state-of-the-art drug testing models, we need to understand the weaknesses of the current models and identify the limitations of the current technology in order to design better alternative models and approaches.

2.2 Cancer Treatment: Chemotherapy and Targeted Therapy

Chemotherapy and targeted therapy are the most commonly used treatments in cancer. Chemotherapy is normally given as the standard of care based on the type of cancer, but with severe side effects. Targeted therapies focus on a subset of molecules that can interfere with specific molecules or pathways involved in tumor growth and progression [7]. Because targeted therapy is more specific to cancer cells, it may be more effective than the traditional chemotherapy with fewer side effects. Both treatments have the same purpose of destroying or stopping the growth of cancer. However, the effectiveness of the treatment varies based on the complexity of the tumor, and different patients with the same type of cancer can have widely differing responses to the same treatment. Despite advances in therapeutic compounds, the personalized testing of drugs on tumors from specific patients is becoming the focus of efforts towards predicting drug efficacy. Therefore, developing a cancer model that has predictive power and allows for the testing of drugs from individual patients should be a focus towards improving cancer therapy.

2.3 Cancer Models for Drug Testing

2.3.1 Dissociated tumor cell culture model

In the past several decades, studies using cell lines and xenografts have significantly improved the understanding of cancer tumor behavior [8-10]. These advanced cell culture

tools and imaging systems used with cell lines remain the most accessible and popular model for investigating tumor cell resistance to chemotherapy drugs. However, established cancer cell lines, which are grown in 2D cell culture dishes and may be stored for long periods, evolve and change from the original cellular conditions and thus may be an inappropriate model for evaluating drugs. More specifically, recent studies have shown that the expression of a specific set of genes associated with drug resistance was very different in cell lines than in tumor samples representing the same cancer types [11]. Tumor-derived primary cell lines in their first few passages have shown high genomic similarity in many cases [12-15]; however, the disruption of the tumor microenvironment is a major factor in the difference in drug efficacy on cell cultures versus animal models or human trials [16].

2.3.2 Three-dimensional cell culture model

Co-culture and three-dimensional (3D) cell culture environments tend to have characteristics which are more physiologically relevant to live tissues than 2D cultures. As the tumor cells co-exist with other types of cells and grow in a 3D environment, both culture methods can better recapitulate the tumor physiology than traditional cell cultures. Compared to the planar cell culture, 3D cell culture has been shown to more accurately influence cell morphology, gene/protein expression, signal transduction, proliferation, migration, and drug tolerance [17-21]. Many existing technologies have been developed for *in vitro* 3D cell culture, including suspending cells in a matrix such as collagen I or Matrigel or culturing cells within biomaterial scaffolds that can be fabricated into desired shapes from a variety of materials [22]. These improved cell culture models have accelerated the discovery of tumor-stromal, ECM interactions and cell-cell signaling, have led to realization of the complexity of the tumor microenvironment, and to the use of intact tumor tissues as a potential powerful tool for cancer research.

2.3.3 Mouse xenograft model

In-vivo mouse models have been used to study cancer biology and screen therapeutics for efficacy, toxicology, and pharmacokinetics. Xenograft models using mice as hosts to mimic the tumor-growing environment are by far the most convincing models for drug

testing. Two methods to generate xenografts are the injection of tumor cells under the skin of a mouse (subcutaneous model) [23] and the injection of tumor cells into anatomically-relevant locations of a mouse (orthotopic model) [24]. In order to efficiently initiate the tumor growth in mice, immunocompromised (T-cell knockout) or severely immunodeficient (SCID, T- and B- cell knockout) mice are required to prevent immune-responses to the injected cells during tumor growth. However, the measurements of response to therapy including the growth rate of the tumor, tumor shrinkage/regression, and survival, do not provide any understanding of the cell-killing mechanisms of the drugs [25, 26]. Furthermore, measures of tumor shrinkage/regression has been reported to not be predictive of efficacy [27], and subcutaneous tumor models that do not represent relevant sites of human tumors are also not predictive when used to test responses to anti-cancer drugs [28]. When primary tumors are used as an orthotopic xenograft model, there is a stronger predictive response value, especially when a clinically relevant drug dosage is used [29-31]. However, it is difficult to follow tumor growth in orthotopic models, which require the development of additional imaging techniques. Furthermore, these models are time-consuming, expensive, and technically challenging, resulting in difficulties in transitioning from a research tool to a clinical drug testing tool. Consequently, xenografts are limited in their use as preclinical models for drug testing.

As a whole, while animal models are the most biologically relevant systems, they represent the most difficult systems in which to study new targets. Testing new compounds in animal models is limited by the need for skilled personnel. Animal models are also expensive and increasingly unpopular for drug testing based on ethical issues.

2.4 The Tumor Microenvironment

In the early cancer research, scientists focused only on the cancer cells themselves. However, in the past couple of decades, evidence has shown that a tumor is not just a mass of individual cancer cells. A cancer tumor is composed of immune cells, endothelial cells, and cancer associated fibroblasts hosted in an extracellular matrix (ECM) arranged in a highly disorganized manner, which form its unique tumor microenvironment responsible for the malignancy of the tumor progression [32] (Fig. 2.1).

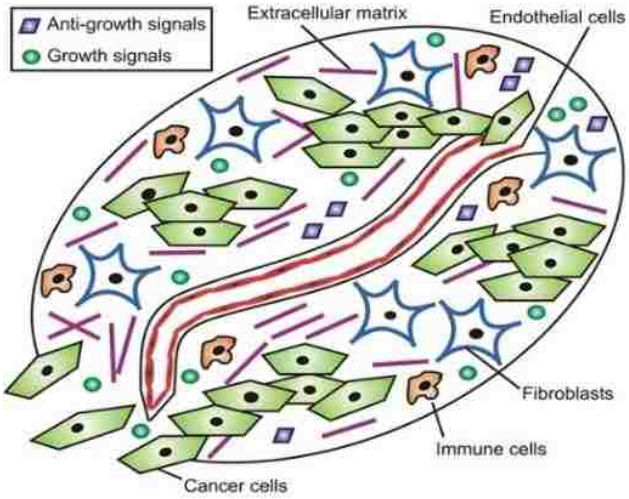

Figure 2.1: The tumor microenvironment.
A solid tumor is composed of various types of cells which are different from the original cell types, the functions of which are typically altered by the tumor cells. This complex and disorganized structure is known as the "tumor microenvironment" which is self-maintained by inducing angiogenesis and producing its own growth factors. These signaling interactions in this environment allow the tumor cells to become insensitive to anticancer drugs and antigrowth signals.

This complexity of the tumor microenvironment causes tumor cells to mutate, to invade into the healthy tissue and to become a lethal disease. Furthermore, these components of the tumor microenvironment play a critical role in determining the responsiveness to chemotherapy. For example, the adhesion of cancer cells to ECM and to fibroblasts by direct contact significantly reduces the sensitivity to chemotherapy drugs [33, 34]. Co-culture of non-small cell lung cancer (NSCLC) cells and breast cancer cells created by plating onto monolayers of astrocytes induce resistance to chemotherapy [35]. Tumor endothelial cells, the main targets of anti-angiogenic therapies, are genetically abnormal and acquire drug resistance in the tumor microenvironment [36]. Furthermore, one recent study has found that the growth factors released by fibroblasts may allow cancer cells to escape from the drugs [37]. This finding was shown experimentally by pairing the co-culture of 23 stromal cell types and 45 cancer cell lines with 35 anticancer drugs using high throughput screening to detect stroma-mediated resistance. As a result, hepatocyte growth factor (HGF) was discovered as a receptor activator, and there is a significant correlation between HGF released by stromal cells and innate resistance to BRAF, a gene

which is responsible in tumor cell growth, inhibitor treatment. Unexpectedly, several findings even suggest that some of the survival signals may come from tumor cells dying in response to radiation therapy [38]. As evidence mounts that the surrounding stromal cells and ECM play a key role in tumorigenesis and tumor progression [39], it has become clear that dissociated tumor cell culture models cannot faithfully replicate the complexity of tumor biology. Accordingly, the preservation of the tumor microenvironment should be a fundamental element in future models for drug testing.

2.5 Organotypic Tumor Slice Culture Preserves Tumor Microenvironment

Organotypic slice culture was invented based on the need for maintaining tissue integrity in the study of cell-cell interactions, and was first used by Warburg for studying tumor metabolism in 1923 [40]. This method was then quickly adopted by neurobiologists for studying the physiological and pharmacological properties of neural interactions from different brain regions [41]. In 1979, Haas introduced a simple method for organotypic slice culture by using a porous membrane with continuous medium perfusion from underneath [42]. In 1991, Stoppini simplified the technique further by using a commercially available membrane well insert, requiring only the periodic change of culture medium [43]. In this porous membrane culture, an air-fluid interface is created by placing the tissue slice on top of a porous membrane, with the cell culture medium located below the membrane. Thus, the tissue is left in contact with air to allow for efficient oxygen transport and maintain good viability. The tissue is hydrophilic and is in contact with humidified air, so it remains moist and allows for the sufficient nutrient and oxygen transport to the tissue. This simple method opens the gate for organotypic slice culture in a wider variety of tissue types including brain slices, liver slices, mammalian retina slices etc., allowing for the preservation of the original tissue structure. This culture technique has also been adapted by oncologists for the purpose of preserving tumor microenvironment as a preclinical model for drug screening [44].

In the last decade, increasing numbers of cancer groups have been utilizing tumor tissue slice approaches that may better replicate tumor physiology for pharmacodynamic and cancer biology studies. Many laboratories have adopted the “organotypic” tissue culture

technique [45] (i.e., on porous membrane supports) with great success [46-50]. In a recent study from Massimo Loda's group, the organotypic slice culture not only preserves tissue 3D architecture and cell viability, but also retains the pathway activity in which the treatment of PI3K inhibitor (PI3K/Akt signaling pathway activity is affected by epithelial-stromal interactions) in lung and colon cancer slice culture models showed a reduction of p-Akt and p-S6RP levels and induced a partial decrease in tissue proliferation and viability [51]; the results were reproduced with other tumors and inhibitors, demonstrating that it is possible to test the effects of therapeutic agents in viable tumor tissue with preserved microenvironments. Another recent finding using human glioblastoma slices under organotypic culture showed that therapeutic outcomes varied by patients and not by O^6-methylguanine-DNA methyltransferase (MGMT) in which the finding demonstrated the apoptotic activities to temozolomide (TMZ) treatment is independent from (MGMT) promoter methylation [46]. (MGMT promoter methylation has been shown to decrease the effectiveness of the TMZ treatment to patients [52-54]).

2.6 Microfluidics for Intact Tissue Cultures

Microfluidics is a rapidly developing field which is utilized in a wide variety of biological studies. This developing technology has the advantages over traditional culture techniques in using smaller reagent volumes, requiring shorter reaction or response times, enabling automation, and allowing for parallel operation [55]. One of the major features of microfluidics is laminar flow, fluid flow through microchannels with low Reynolds numbers in which fluids do not mix turbulently and thus can be spatiotemporally controlled and predicted at small scales. These features enable the creation of biomimetic environments and the study of biological behaviors. Thus, microfluidics has potential use in preclinical models for drug testing in significantly improving preclinical models for drug testing.

The use of microfluidic devices for studying intact tissues is a relatively new research field which involves a series of challenges [56]. The intact tissue samples (tissue slices or biopsies) cannot be submerged in a static culture chamber as in the majority of devices

used for dissociated cells. These samples require oxygenated medium perfusion or exposure to air in order to allow for proper oxygen/nutrient transport given the thickness of the tissue. Hence, the design of the microfluidic devices needs to accommodate this culture condition in addition to other functional criteria.

A major microfluidic device design used to maintain the viability for intact tissue cultures has included a simple culture chamber in conjunction with microchannels to allow the continuous perfusion and collection of the medium [57, 58]. However, this design has only demonstrated limited functionalities compared to microfluidic devices which have been demonstrated for use with dissociated cell culture. Other microfluidic devices have shown the potential for delivering reagents locally to intact tissues [59-62]. Nevertheless, the high flow rates needed to maintain laminar flow patterns with minimal diffusive broadening, low throughputs, short-term exposure, low viability, and channel obstructions by air bubbles and tissue debris are limitations and concerns for practical use in the preclinical field.

2.7 Personalized Chemotherapy: A Preclinical Drug Testing Model

A major challenge of personalized chemotherapy is the ability to accurately predict drug responses in cancer patients. As recently as this past decade, many researchers believed models using either cell lines created from patient tumors [63] or patient-derived mouse xenografts [64] would have a high degree of relevance for drug testing. Nevertheless, the lack of tumor microenvironment from the cell lines and the difference in hosts between mice and humans raise concerns [65]. Presage Biosciences has pioneered a method which uses a microneedle array device with the ability to infuse multiple drugs into living tumors, allowing for the identification of drug candidates for treatments. However, the requirement of large solid tumors, risk of *in vivo* implantation, and low-throughput drug selection are major bottlenecks in this technology. Overall, the use of intact tumor tissue slices and biopsies has the advantages of undergoing low-passage growth, preserving the tumor microenvironment, allowing high-throughput drug screening, allowing the use of standard microscopes, and the ability to quickly obtain chemosensitivity response results.

Chapter 3. *In-vitro* Clonogenic Assays using a User-Friendly Microwell Array Device

3.1 Summary

In this chapter, we demonstrate an *in vitro* cell culture model to allow for measuring cell proliferation and senescence from a large population of single cells. For this assay, we developed a user-friendly microwell array device to allow for the tracking of growth behaviors from large numbers of single cells. The tracking of each microwell and cell was performed using automated microscopy based on the known positions and spacings of the microwells. The proliferation and senescence data from the single cells was then quantified using a straightforward model to reveal cell-to-cell heterogeneity within a large population. In order to demonstrate the ability to differentiate two different cell populations using this assay, we depleted the WRN gene from one population of the same type of cells, which has shown effects on cell proliferation and senescence compared to the cells without depletion. As a result, our assay based on this simple approach can quickly measure cell proliferation and senescence from large numbers of single cells and has potential application to study tumor heterogeneity based on single-cell growth behaviors.

3.2 Introduction

In vitro cell culture models play an important role in cancer research. In addition to their role in improving understanding of cancer biology, a variety of in vitro cell culture assays developed in the past several decades enable cytotoxicity studies to be performed in a quantitative manner. Additionally, the effects of drugs on cancer cells can be studied based on key cell behaviors, which may have significant relevance in tumor progression.

Among all the cell behaviors, cell proliferation, death and senescence are key determinants of the growth of cell populations [66-68]. Cell-to-cell heterogeneity in proliferation, growth potential, morphology, and response to therapy have long been noted in both normal and tumor cell populations [69]. An important challenge in better understanding tumor cell populations and their response to therapy is to improve our

understanding of cellular heterogeneity. An important experimental approach to the analysis of cellular heterogeneity has been the use of single cell-derived cultures, often referred to as clonal cultures, to reveal and quantify differences in cellular behavior. One widely used version of this approach in both toxicology and cancer cell biology is to determine the colony-forming efficiency (CFE) of individual cells after treatment with a drug or therapeutic agent [70]. This assay has been further elaborated with the development of specialized cell culture plates to array and then follow the growth of large numbers of single cells over time. A prominent early example of this approach was the development of microdroplet culture plates for HLA typing of human lymphocytes by Terasaki and colleagues [71] which were subsequently used to follow the proliferation of individual lymphocytes. Widely used contemporary examples of this approach to cell culture miniaturization and the analysis of single or small numbers of cells can be seen in the many assays and protocols adapted to be performed in 96-well plates [72].

We have extended this approach by developing polydimethylsiloxane (PDMS) microwell arrays which have been designed to facilitate the seeding of single cells in microwells. The arrays are chemically bonded onto dry cell culture dishes before addition of any solutions. The growth and senescence of many parallel cultures initiated from single cells can then be monitored using conventional cell culture and imaging equipment and protocols. In order to demonstrate the ease of use of microwell arrays, we fabricated and used 512-well and 900-well microarrays to characterize the proliferation and senescence of isogenic human cells which either expressed or had been depleted of the Werner syndrome protein WRN. This human RECQ helicase plays important roles in DNA replication, recombination and genome stability assurance [73-75]. Heritable inactivating mutations in the *WRN* gene cause Werner syndrome, a cancer predisposition syndrome with features of premature aging [76]. The loss of WRN function in somatic cells leads to marked suppression of cell proliferation, an increase in the probability of cellular senescence and selective sensitivity to cell killing by several important classes of cancer chemotherapeutic agents [76, 77].

The use of PDMS-based microwell arrays allowed us to rapidly collect data on the proliferation, senescence or death of large numbers of isogenic WRN+ and WRN-depleted cells. These data were used to develop a simple quantitative model of the growth of populations of cells as a function of WRN protein expression. We developed this as a standard exponential growth model of the same general type as was recently reported by Tyson *et al* [78], with the important differences that our model uses senescence in place of quiescence, and does not allow cells to return from senescence to the reproductive state. The growth rate, r, can be estimated from the change in cell number over time across many wells. The ratio of senescent to live cells can be used to estimate the contribution of senescence to growth rate differences between cell types as defined by WRN protein expression.

3.3 Materials and Methods

3.3.1 Fabrication of PDMS-Based Microwell Device

Masters for casting microwell cell arrays were generated by using standard photolithography to pattern SU-8 (Microchem, Newton, MA) microposts on a silicon wafer. Each microwell has dimensions of 500 μm (square edge or round well diameter) with a wall height of 400 μm and edge-to-edge well spacing of 500 μm. Microwell arrays are cast on SU8 masters by pouring uncured PDMS over the master followed by exclusion molding [79] with a release liner (3M, MN), then baking at 70ºC for at least 2 hrs (Fig. 3.1a). Exclusion molding allows open wells to be made in PDMS, while the release liner allows physical handling and transfer of the resulting PDMS membrane while retaining the molded features with high resolution. PDMS microwell arrays are bonded to polystyrene cell culture dish by first treating the culture dish with oxygen plasma, followed by treatment with 1% aminopropyltriethoxysilane (APTES) solution for 20 min followed by a distilled water rinse and drying with an air gun [80]. The PDMS microwell array is oxygen plasma-treated before being bonded to the silane-modified culture dish at room temperature (Fig. 3.1b). After bonding, the pre-formed open microwells are revealed by peeling the release liner from the PDMS surface. Microwell arrays were then UV-sterilized and oxygen plasma-treated to ensure that APTES is etched off the polystyrene growth surface. The arrays is then coated with 20 mM poly-D-

lysine for 2 hours followed by three washes with phosphate buffered saline (PBS) prior to being used (Fig. 3.1c).

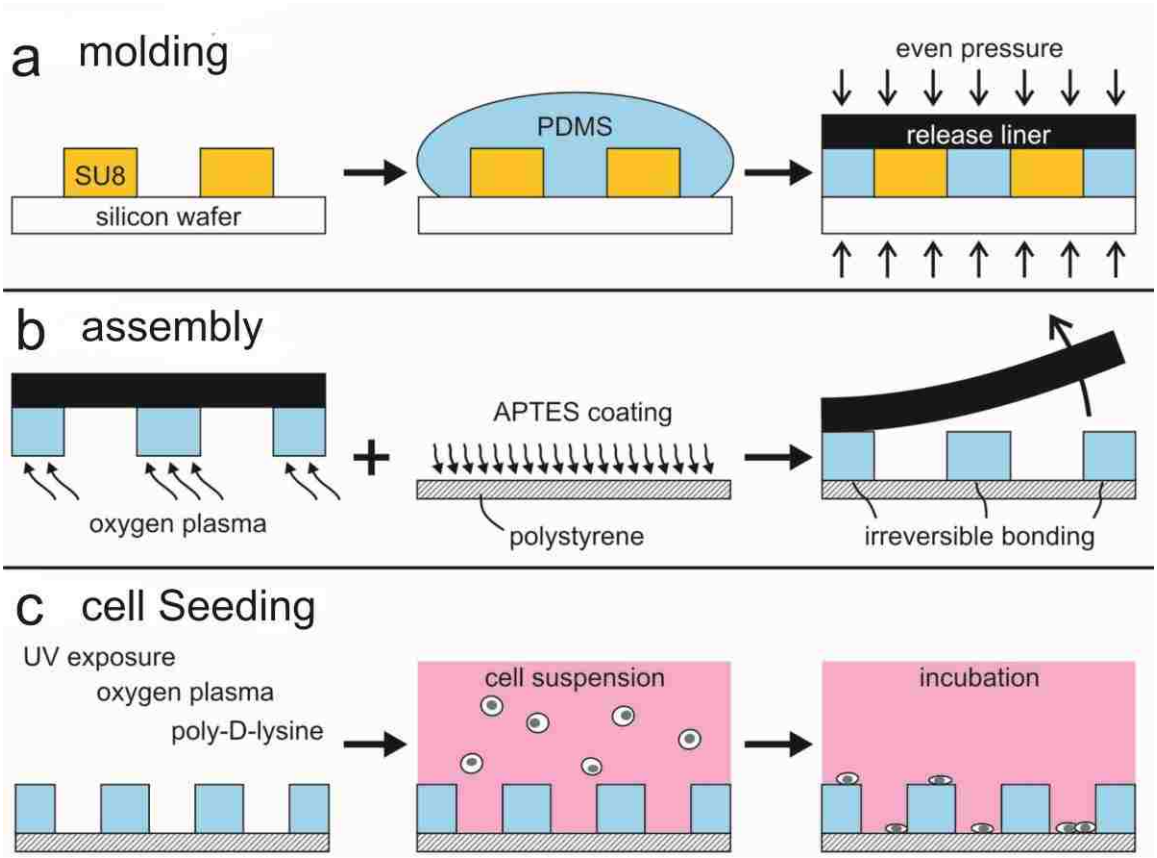

Figure 3.1: Fabrication of 900 well PDMS microwell arrays.
(a) Molding of PDMS microwell array by exclusion molding. (b) Assembly of a PDMS microwell array to a polystyrene dish. A PDMS microwell array is surface-treated and bonded to a conventional 10 cm polystyrene cell culture dish. PDMS microwell array membranes can also be bonded or conformed onto other cell culture-compatible pre-coated or pre-patterned substrates. (c) Cell seeding protocol. Arrays are surface-treated prior to cell seeding by UV sterilization, oxygen plasma treatment to generate a hydrophilic surface, and finally poly-D-lysine surface coating. Cell seeding is done in cell culture medium (20 mL) seeded over the microwell array in culture dishes under unit gravity for 2 hr.

3.3.2 Cell Culture

GM639 SV40-transformed human fibroblast cells were obtained from the National Institute of General Medical Sciences (NIGMS) Human Genetic Mutant Cell Repository (Camden, NJ) and cultured in Dulbecco's modified Eagle's medium supplemented with

10% (v/v) fetal bovine serum (Hyclone Laboratories, Logan, Utah), penicillin (100 units/mL), and streptomycin (100 µg/mL) in a humidified 5% CO_2 incubator at 37°C.

3.3.3 Cell Seeding

Our microwell device has an array of open-well design which allows for the cell seeding directly from the top of the wells. When cells are seeded randomly onto the device, the number of cells per well (N) can be described as a discrete random variable following Poisson distribution (given below) with parameter λ, which is equal to the expected value of the variable N.

The probability mass function for N = 1 (1 cell/well), which is maximized at λ = k = 1, is equal to 0.3679 (36.79%). Hence, our calculations, together with pilot experiments, indicated that seeding microwell arrays in 10 cm round polystyrene cell culture dishes using 20 mL of culture medium containing 1000 cells/mL maximized the frequency of wells seeded with single cells (which was approximately 37%).

3.3.4 Automated Tracking of Single-Cell Clonal Expansion

The dimension of an individual microwell is designed to fit within the field of view from a 20X objective on an epifluorescent microscopy. Therefore, cell numbers and morphology in each microwell can be readily observed from each phase-contrast images without the need of additional cell tracers. A Nikon inverted microscope with Perfect Focus™ system (Melville, NY), a motorized x-y control and imaging software were used to automate the imaging of clonal expansion of single cells in microwell arrays. Arrays were imaged every 24 hrs over 7 days, where each imaging cycle involved ≤ 20 min (~1 second per well) on the imaging stage. This short observation period minimized changes in temperature and in cell culture medium pH. Images from each well were individually reviewed to count cells over each experiment.

3.3.5 Assessment of Cell Viability and Senescence

GM639 cells that die during clonal growth develop a rounded morphology and detach from the microwell, and are easy to identify by a combination of phase contrast imaging and live-dead staining (LIVE/DEAD cell viability assay, Invitrogen, Carlsbad, CA). In this assay dead cells that lose plasma membrane integrity are stained with red-fluorescent ethidium homodimer-1 (EthD-1), whereas live cells are stained with green-fluorescent calcein-AM. This combination of staining and imaging allowed us to identify both viable and dead cells in microwell cultures.

Senescent cells also fail to proliferate, but remain viable and metabolically active despite the absence of cell division [68]. Potentially senescent fibroblast cells are easy to identify on the loss of proliferative potential and the basis of their distinctive so-called 'fried-egg' morphology alone (Fig. 3.2a), and can be further confirmed by staining for senescence-associated beta-galactosidase (SA-βgal) activity [81]. Identifying both dead and senescent cells can be addressed by LIVE/DEAD assay staining followed by fixation with 4% para-formaldehyde prior to SA-βgal staining (Fig. 3.2b).

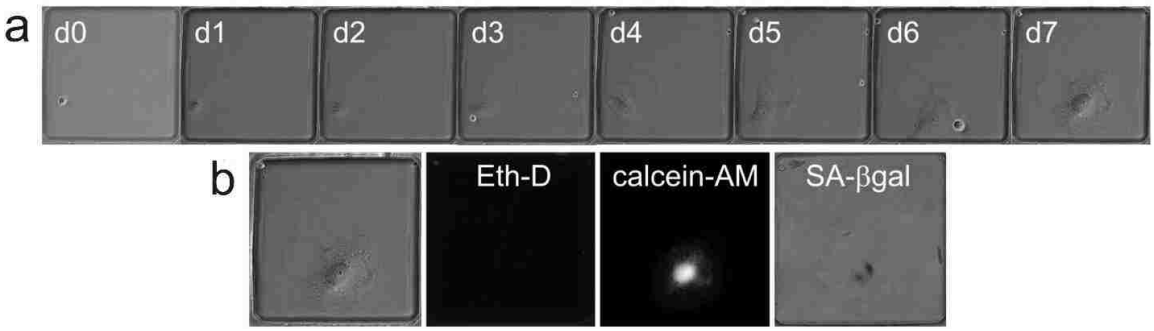

Figure 3.2: Microwell imaging and cell staining to distinguish among live, dead and senescent cells.

(a) Phase contrast microscopy reveals potential senescent cells which have a 'fried egg' morphology with greatly extended cytoplasmic projections and a rounded up, centrally-placed nucleus (arrows). Senescent cells may also have more than one nucleus, possibly the result of cytokinesis failure [82]. (b) A single viable cell which excludes EthD-1 but is stained by calcein-AM and SA-βgal staining.

Our microwell arrays use standard cell culture dish formats, and thus once seeded are easy to image using conventional automated microscope stages. Single wells and cells

can be tracked by the automated capture of phase contrast images. This procedure allows cell proliferation to be analyzed over time without the need for cell staining, while minimizing disruptions to the culture medium or growth conditions.

3.3.6 Depletion of WRN Protein

The WRN protein in GM639 human fibroblasts was depleted by transducing cells with a WRN-specific shRNA-expressing lentivirus at multiplicity of infection (MOI) of 10 for 24 hrs, followed by an additional 72 hrs of selection for transduced cells with puromycin (1 µg/mL) [77]. The extent of depletion of the WRN target protein was quantified by Western blot analysis followed by densitometry using Kodak Molecular Imaging software. We chose an MOI = 10 and 90-95% WRN depletion based on prior data [73, 77] to reveal WRN-dependent cellular phenotypes without severely compromising cell proliferation.

3.3.7 Modeling for the Analysis of Clonal Expansion

We employed a standard exponential model for population growth which is derived by assuming that growth is proportional to the population at time t and that the growth rate, r, equals birth rate (r_1) minus senescence rate (r_2) minus death rate (r_3), as in Tyson *et al* [78]. The resulting model for the population in a well at time t is then $P(t) = P_0\ exp(rt)$ where P_0 is the population on Day 0, which translates to the log-linear model $\ln(P) = \ln(P_0) + rt$. The growth rate for each well is estimated using least squares linear regression to obtain r directly from the slope estimate. The distribution of these r's was estimated using the density function in "R Project" (a publicly-free, statistical software, www.rproject.org). In order to estimate the senescence rate r_2, note that if P_s is the number of accumulated senescent cells at time t, then the solution to the first order differential equation $dP_s = r_2 \times P(t)dt$ is $P_s(t) = r_2/r\ P(t)$, from which it follows that $r_2/r = P_s(t)/\ P(t)$ for all t. Hence, r_2/r was estimated as the mean number of senescent cells per well divided by (total number of cells – number of senescent cells), the divisor being the estimate of the number of dividing cells. Note that this estimator assumes that all cells moving to the senescent state are countable on Day 7. In actuality, some senescent cells

may be lost by Day 7. Because r_2/r is independent of t, it may be advisable to count senescent cells at earlier time points in future experiments, bearing in mind the trade-off between accuracy from a larger sample size per well and the loss of senescent cells. We estimate $r + r_2 = r_1 - r_3$ by $(r_2/r + 1) \times r$. A similar argument shows that the ratio of non-dividing single-cell wells to dividing single-cell wells on Day 0 estimates $r_2 + r_3$. We then can estimate both the birth rate $r_1 = r - (r_2 + r_3)$ and the death rate $r_3 = r_1 - (r_1 - r_3)$ to deconvolve r into its three components. All analyses were done using R. These analyses derive useful and appropriate equations, and provide proof-of-principle to help guide future experiments and the modeling of results.

3.4 Troubleshooting

Our initial design for trapping single cells to perform single-cell clonal expansion contained small suction channels connected to individual open microwells. This suction channel idea to was inspired by the patch clamp chip [83], in which a small microchannel was used to trap and aspirate a single cell. We took the same approach by connecting the trapping channels to an array of 512 open microwells, as illustrated in Fig. 3.3a. Each well contains a small aperture connected to a suction channel (Fig. 3.3b). When suction is applied, a single cell is trapped against the aperture, and untrapped cells were removed by washing with buffer solution. These steps result in a higher percentage of single cells in individual wells. The single-cell trapping efficiency is about 52% in the wells using this active trapping method and 34% in the wells without active trapping (Poisson distribution).

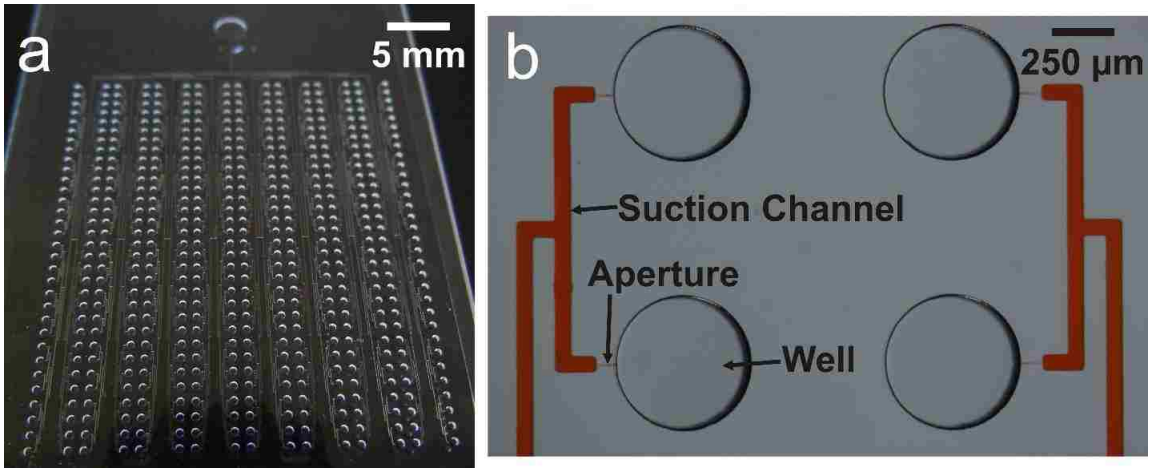

Figure 3.3: 512 well PDMS microwell arrays with active single cell trapping.
(a) Single-cell trapping and clonal expansion device, showing 16 x 32 well array. All the channels are connected in a binary form to allow to ensure equal channel resistance to a single control inlet. (b) Micrograph detail showing four wells. Vacuum channels and apertures are filled with red dye to improve visualization. Dimensions (width x height) – wells: 500 x 300 µm, channels: 50 x 75 µm, apertures: 5 x 2 µm.

However, the major concern with this method was that the cells may become physically damaged from the suction generated by the vacuum. This potential damage raises concerns for cell proliferation experiments. Furthermore, we have encountered difficulties in releasing the cells away from the apertures. Therefore, the trapped cells were often stuck in the apertures (Fig. 3.4) and thus lost viability over time.

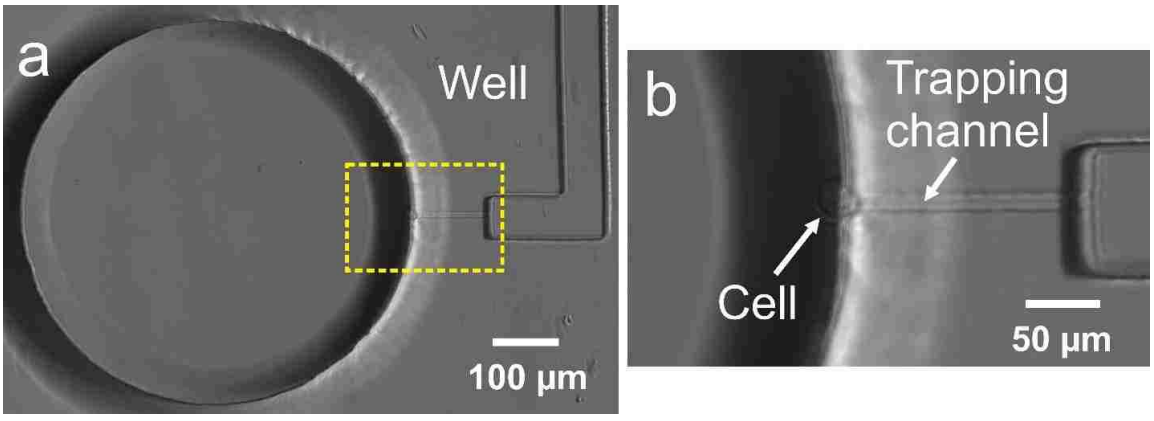

Figure 3.4: Single cell trapping causes cells to become stuck in the apertures.
(a) A single cell was trapped in an aperture within an open well. (b) Zoom-in image from the yellow-dashed box in (a) shows a part of the cell body is squeezed into the trapping channel due to vacuum suction.

Multiple published methods for trapping single cells have been considered as potential approaches to improving the single cell trapping efficiency [84, 85]. However, all of the prior designs only worked in microfluidic devices with enclosed chambers. After considering these prior designs, we decided to take an advantage of a statistical approach to facilitate the cell seeding process.

Another issue we encountered in our microwell cell array was dirty wells containing particles, as shown in Figure 3.5a. The fiber-like particles deposited on the culture surface during cell culture have a direct effect on the quality of the images used for cell counting. From our testing, we found that the majority of these particles came from the serum in the culture medium. This growth factor had a tendency to aggregate and form visible particles over time. Therefore, the culture medium has to be filtered (0.2 μm filter) prior to being used for cell seeding or cell culture. Once the medium was filtered, the culture surface of the microwells was clean without large particles (Fig. 3.5b).

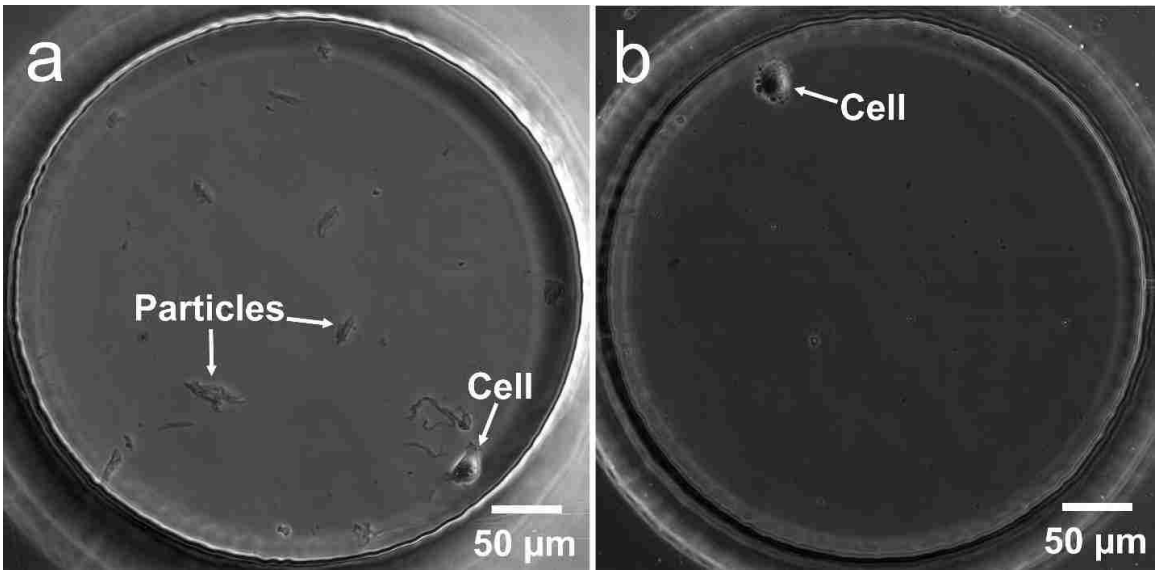

Figure 3.5: Serum accumulations on the culture substrate surface.
(a) Large particles deposited into a microwell containing a single cell. (b) Once the culture medium was filtered before use, similar microwells appear to be very clean without many visible particles.

Since the suspended cells were randomly seeded in our microwell array, the cells would also adhere to the top surface of the microwell array without landing in a well. We did

not typically attempt to wash off these cells that did not land in a well. We took care to minimize shaking when replacing medium once every 2 days during the 7 day growth period, and when transferring microwell array dishes from the cell culture incubators to the imaging stages. We quantified the fraction of wells that were seeded with no cells but acquired 1 or more cells over an experiment to demonstrate that the potential for well cross-contamination from other wells, from the microwell array surface, or from culture media, was low across all experiments (≤3%). In order to further eliminate well cross-contamination, a cell repellent coating on the top surface of the microwell array could also alleviate this concern.

We have also explored the potential of culturing cells on a microscope using an on-stage incubator for long-term cell tracking (Fig. 3.6a). An on-stage incubator designed for microscope normally has a heating system (Indium tin oxide, or ITO, glass is the most common heating element) with a temperature probe. The heating system may either regulate temperature using automated feedback or may require manual control of the temperature based on the temperature probe. Both automated and manual heating systems can provide the steady temperatures required for proper cell culture conditions. To allow for cell culture, the key differences that the on-stage incubator does not provide the same condition as a conventional cell culture incubator are the gas supply (5% CO_2) and the humidity which affect pH and osmolarity in the culture medium. In the conventional cell culture incubator, the chamber is completely sealed with a CO_2 sensor to control the concentration of 5% CO_2 and a water bath to create a high humidity environment (normally the humidity reaches ~85%). In contrast, on-stage incubators do not provide a perfect seal (Fig. 3.6b). Therefore, similar techniques to control the CO_2 concentration and maintain high humidity in the chamber are difficult.

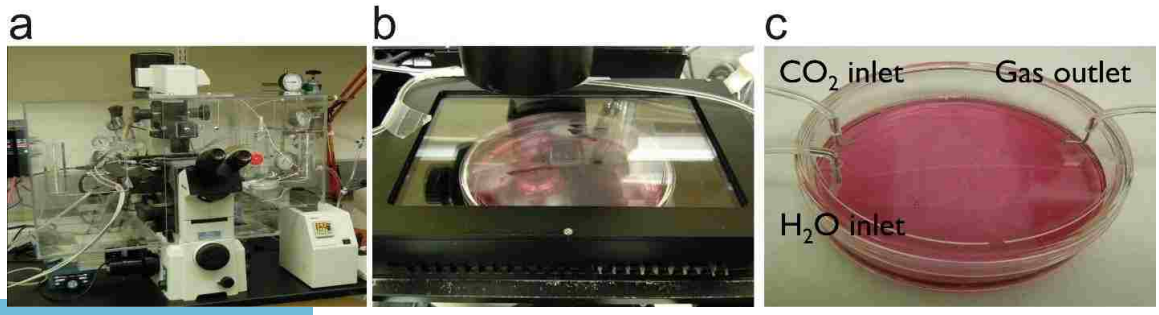

Figure 3.6: Long-term cell culture on microscopy.
(a) Inverted epifluorescence microscopy (b) On-stage incubator with a petri dish in the chamber. (c) Customized cell culture petri dish. The lid has three drilled holes to allow for the insertion of the CO_2 gas, sterile water and gas outlet tubing.

In order to overcome pH and osmolarity in cell culture medium, we set up a customized cell culture dish as shown in Fig. 3.6c. A petri dish with gas inlet and outlet to allow for 5% CO_2 gas perfusion within the culture dish, directly above the culture medium. (Note that the gas line has to be filtered through water to eliminate fine particles from the gas cylinder.) The dry gas injection into the dish results in high evaporation of water from the medium and causes the changes of pH and osmolarity in the culture medium. To resolve this evaporation issue, we calculated the rate of evaporation with time and perfuse the sterile water with the same evaporative rate back into the culture medium. As a result, we were able to maintain single neurons on the microscope stage for at least 4 days (Fig. 3.7).

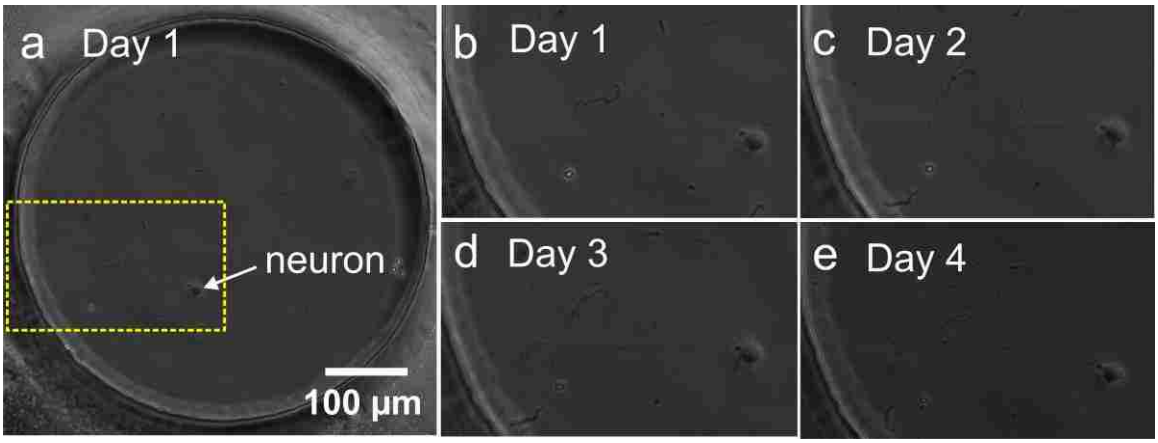

Figure 3.7: On-stage single neuron culture.
(a) Single neuron was cultured in a microwell. (b-e) The neuron was cultured in an on-stage incubator and tracked using an inverted microscope for 4 days. An axon of the neuron grew and extended over the 4 day period.

3.5 Results and Discussion

3.5.1 Large Array of PDMS-Based Microwell Device for Studying Single-Cell Clonal Expansion

Exclusion molding [79] provides a simple and reliable way to generate PDMS microwell arrays from a microfabricated master. The features of the master are photolithographically defined in SU-8 (Microchem, Newton, MA), a photosensitive epoxy; we have investigated various patterns such as 512-round well, 900-square well, and 3000-square well arrays. Once generated, the SU8 master can be used repeatedly to generate PDMS multi-well microarrays by exclusion molding. Figure 3.8a demonstrates an exclusion-molded PDMS membrane with square-round hollow structures on the membrane. The oxygen plasma treatment and APTES bonding protocol [80] work together to irreveriblely bond the PDMS microwell array to cell culture-grade polystyrene dishes (Fig. 3.8b).

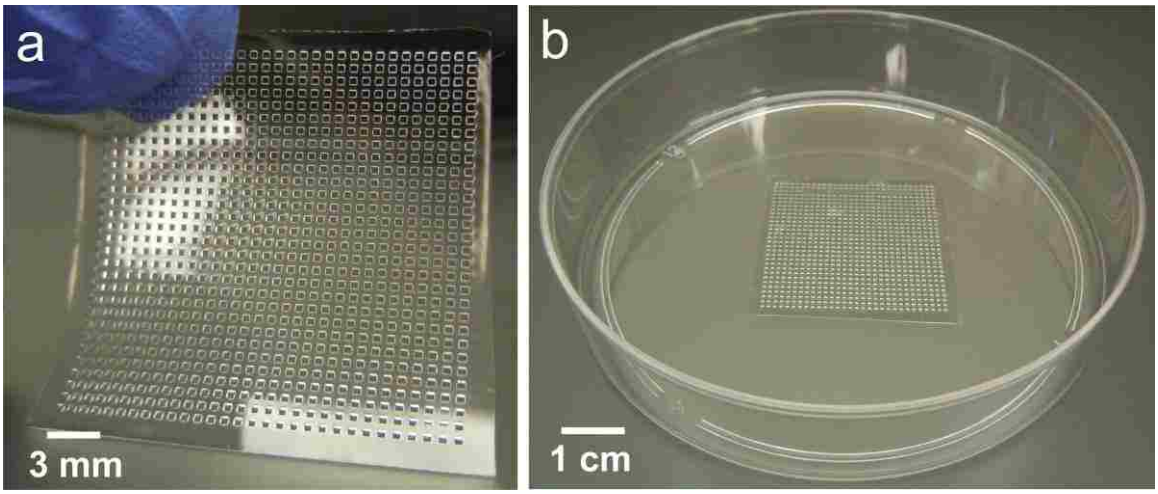

Figure 3.8: 900 well PDMS microwell arrays.
(a-b) Example of PDMS microwell membrane prior to (a) and after (b) bonding to a conventional 10 cm polystyrene cell culture dish to form the completed microwell array.

The microwell culture system described here is compatible with current cell culture and automated imaging methods and protocols. Microwell arrays can be fabricated in a wide range of formats, and up to 3000 microwells can be easily handled in a single 10 cm culture dish. Microwells thus avoid the common 'edge' effects which often plague 96-well plate-based experiments in which center and edge wells experience substantially

different growth environments. These microwell arrays are simple and inexpensive to fabricate, can be modified easily to generate different well geometries, and can be bonded or conformed on pre-coated or nano-patterned substrates to allow the growth and analysis of many different cell populations of high biological or medical interest, e.g., ES or iPS cells, and their lineage-specific, differentiated progeny.

3.5.2 Cell Seeding by Poisson Distribution

The design of microwell arrays is useful because the wells can be easily and reliably seeded with a desired average number of starting cells. The actual number of cells that are seeded in each individual microwell cannot be controlled, but the distribution (known as Poisson distribution) is very well understood and allows us to predict the proportion of wells seeded with different numbers of starting cells. We then empirically determined the optimal cell concentration and culture medium volume needed to obtain the highest percentage of microwells containing single cells. For 900-well arrays (Fig. 3.8), we found that flooding microwell arrays in 10 cm dishes with 20 mL of culture medium containing 1000 cells/mL resulted in the reliable seeding of ~1/3 of the microwells (32%) with single cells.

Our use of a cell seeding strategy that takes advantage of Poisson statistics provides a very simple and highly reproducible way to seed a predefined fraction of wells with single (or other defined numbers of) cells, while minimizing cell manipulation and the potential for damage.

3.5.3 Large Numbers of Single Cell Proliferation during Clonal Growth in Microwell Cultures

We performed pilot experiments to determine the best protocol to follow cell proliferation in microwell cultures. These experiments used GM639 SV40-transformed human fibroblasts [73, 76, 81] and a 512-well round microwell array in which we followed the number of cells per well over a 7-day growth period (Fig. 3.9). Daily imaging of microwells seeded with single cells was used to systemically track cell number/well as a function of time. This approach revealed remarkable heterogeneity in

the proliferative behavior of single cells. Four different clonal proliferation patterns could be identified: exponential proliferation (38% of wells); slow or variable proliferation (30%); non-dividing viable cells (7%); and cells which were lost from the wells and were presumed to have died (25%). The combined percentage of wells showing proliferation (68%) closely approximates the colony forming efficiency of GM639 cells as determined by conventional dilute plating CFE assay [73, 75, 77].

We next compared the proliferative behavior of isogenic cultures of the same GM639 SV40- transformed human fibroblasts which had been depleted or mock-depleted of the WRN RECQ helicase protein. In previous work that cells depleted of WRN displayed the same defects in cell proliferation, senescence and DNA damage sensitivity as had been previously observed in primary and SV40-transformed fibroblast cultures derived from Werner syndrome patients [73, 75, 77]. WRN-depleted and control (mock-depleted) GM639 SV40 fibroblast cells were made by transducing GM639 cells with a lentiviral vector expressing either a shRNA that targeted the *WRN* gene and depleted the corresponding WRN protein [73, 75, 77], or a scrambled shRNA with no known target sequence in the human genome. In previous experiments, changes in cellular phenotype observed in WRN-depleted cells reflected WRN depletion, as opposed to shRNA-specific off-target effects, lentiviral infection or engagement of the RNAi machinery [77, 86].

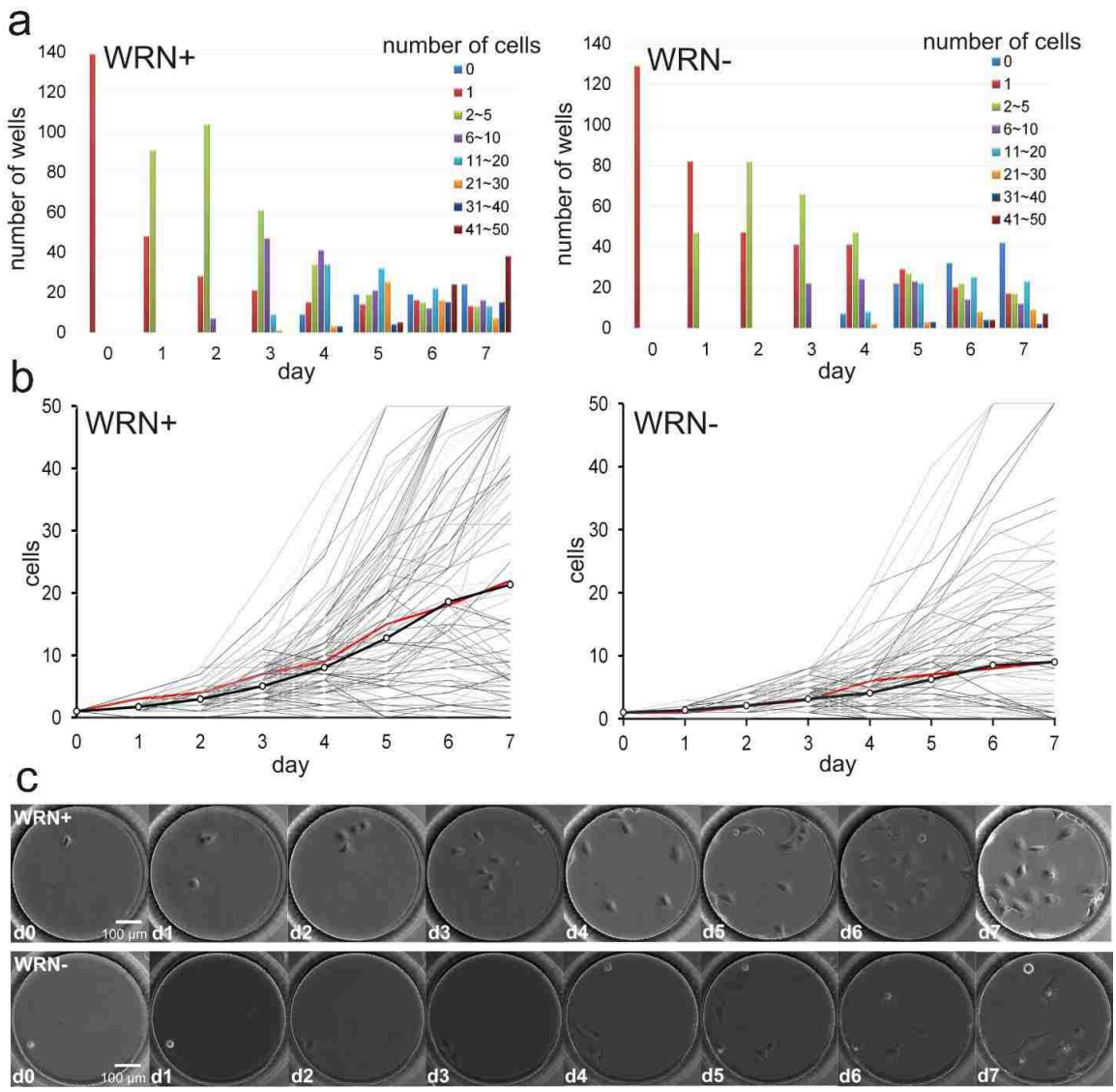

Figure 3.9: Proliferation of single human cells in microwell arrays.

(a,b) Number of cells/well in wells seeded with single WRN+ or WRN-depleted cells after a 7 day growth period shown as a bar graph (a) or growth curve (b). Wells were traced every 24 hrs by acquiring focused images, and the cell number in each well counted. Black curves in (b) represent the mean increase in cell number over time across all single cell wells. The red curves depict the proliferative behavior of the wells shown in (c). (c) Phase contrast images of the proliferation of a single cell in a round 500 μm diameter, 400 μm high microwell over 7 days. These wells were chosen because their proliferative behavior (red curves in (c)) follows most closely the average behavior (black curves in (b)).

We used a daily (24 hr) imaging interval in our experiments, as this represents a common division time for many human cells in culture. More frequent imaging can also be readily

achieved, and can be performed on even very short time intervals (minutes to ≥1 hr) by using an on-stage incubator to ensure consistent culture conditions. Imaging on longer timelines is also possible and may be important for very slowly dividing cells, or where cell differentiation in conjunction with proliferation is to be analyzed (e.g., in the proliferation and differentiation of neural precursor cells derived from ES or iPS cells). These different uses and extensions of our current microwell culture system will make it easier to generate detailed information on the behavior of single cells, and thus to better understand and eventually control cellular heterogeneity.

3.5.4 Probability of Cell Proliferation as a Function of Starting Number of Cells

The fraction of wells containing 0 cells served to confirm our predicted distribution, and was also useful for monitoring potential cross contamination between wells or from the PDMS surface. Neither type of well contamination was common: ≤3% of wells initially observed to contain 0 cells was found to contain 1 or more cells at the end of growth experiments of up to 7 days. Using the Poisson distribution to predict cell seeding in the microwells also allowed an easy way to determine whether proliferative behavior is strongly influenced by the starting number of cells in a microwell. As shown below, the procedure was done by identifying wells seeded with 0, 1, 2 or 3 cells at immediately after seeding, and then following all wells over 7 days to determine the proliferative potential of wells as a function of initial cell number.

In order to determine whether proliferative potential was strongly influenced by the number of starting cells in a microwell, we also compared cell proliferation in wells seeded with 1, 2 or 3 cells. We did this by plotting the fraction of wells that proliferated (i.e., increased in cell number from the starting cell number) over 7 days. Figure 3.10 shows that the probability of proliferation increased as more cells were seeded into microwells, but that this increase was not proportional.

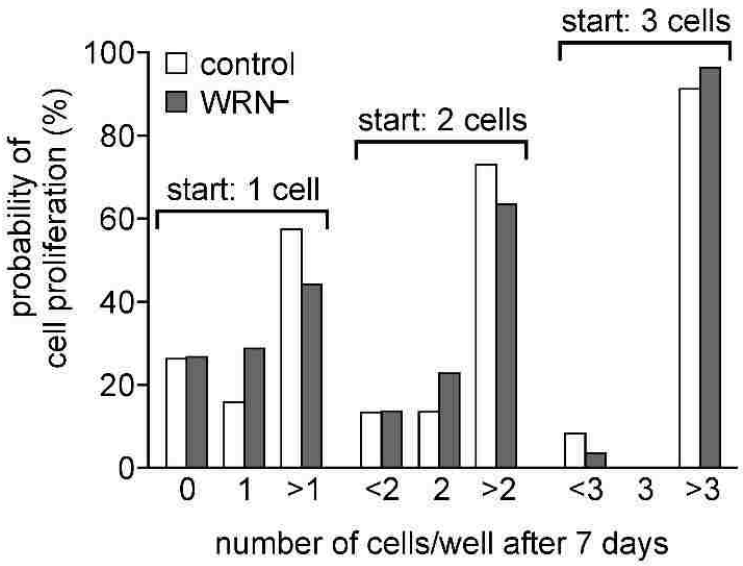

Figure 3.10: Probability of cell proliferation as a function of starting number of cells/well and WRN protein expression.

The proliferative potential in wells seeded with 1, 2 or 3 cells increases, as does the probability of the cell proliferation as a function of starting cell number.

3.5.5 Depletion of WRN Protein Alters Cell Proliferation and Senescence during Clonal Growth

Loss of function of the Werner syndrome protein is known to alter the probabilities of cell proliferation and senescence [73, 76, 77, 87]. Consequently we wanted to examine the contribution of these two determinants of cell population growth in microwell cultures using isogenic WRN+ and WRN-depleted GM639 fibroblasts. In order to measure cell proliferation in 512 well microwell arrays and compare the result with prior data from conventional cell culture protocols, we determined the fraction of wells which reached ≥ 50 cells over a 7 day growth period. This is about the largest number of cells that can be reliably counted in microwells. These experiments showed that the average proliferative rate of WRN-depleted cells was 40% lower than the rate of isogenic WRN+ control cells. When we looked at final cell numbers in wells which proliferated to any extent, we found that 17.5% of single control cells but only 4% of WRN-depleted cells were able to proliferate over 7 days to generate ≥ 50 cells (Fig. 3.11). Moreover, the average cell number per well was significantly higher in control than in WRN-depleted

cells. These microwell array experiments were thus able to reveal the previously described proliferation defect in WRN-depleted GM639 fibroblasts [73, 77, 87].

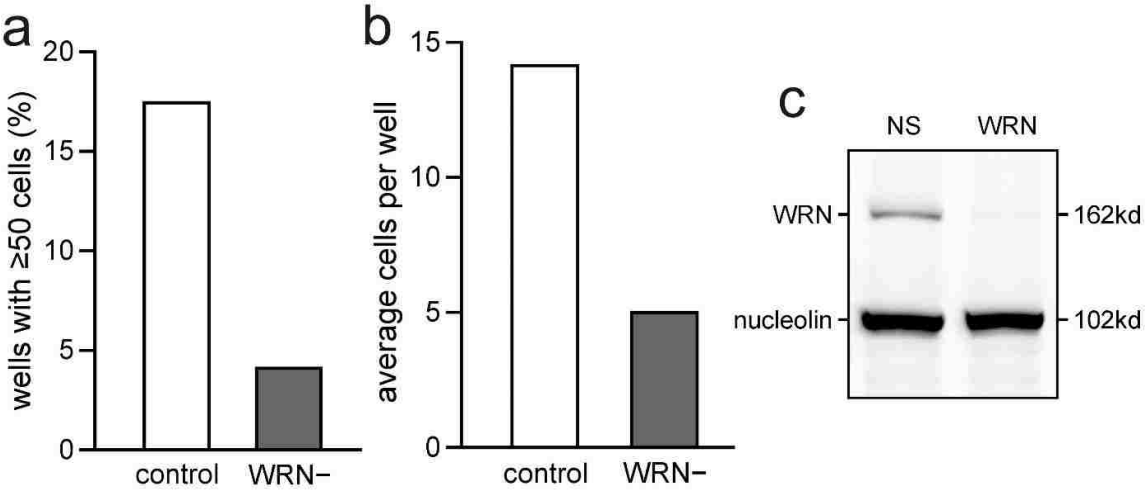

Figure 3.11: Proliferative behavior of WRN+ and WRN-depleted cells as assessed by maximum and mean cell counts.

(a) Percentage of microwells seeded with single cells that reached a final cell number of ≥ 50 cells after 7 days as a function of genotype. (b) Average cell number of wells seeded with single cells after 7 days growth as a function of genotype. (c) Western blot verification of the extent of depletion of WRN protein in cells used for this experiment. Densitometry analysis revealed that lentiviral shRNA expression had depleted 94% of the 162 kDa WRN protein in this experiment. Panels were generated from data derived from 189 wells in control (WRN+) data and 195 wells in WRN-depleted data in 512 microwell assays.

WRN depletion also influenced the fraction of GM639 cells which died or became senescent during clonal growth in microwell cultures. We were able to quantify both the number of wells containing senescent cells and the number of senescent cells per well, as described above, by a combination of cell counting and staining. These experiments were performed in 900-well arrays using isogenic pairs of GM639 fibroblasts in which the WRN shRNA-depleted cells were 90% depleted of WRN (Fig. 3.12). Wells containing WRN-depleted cells had a 2.7-fold higher likelihood of containing 1 or more senescent cell (17.4%), when compared with control/mock-depleted cells (6.5%) (Fig. 3.12a). The total number of senescent cells in WRN-depleted cell wells was nearly 7-fold higher than control cell wells (Fig. 3.12b).

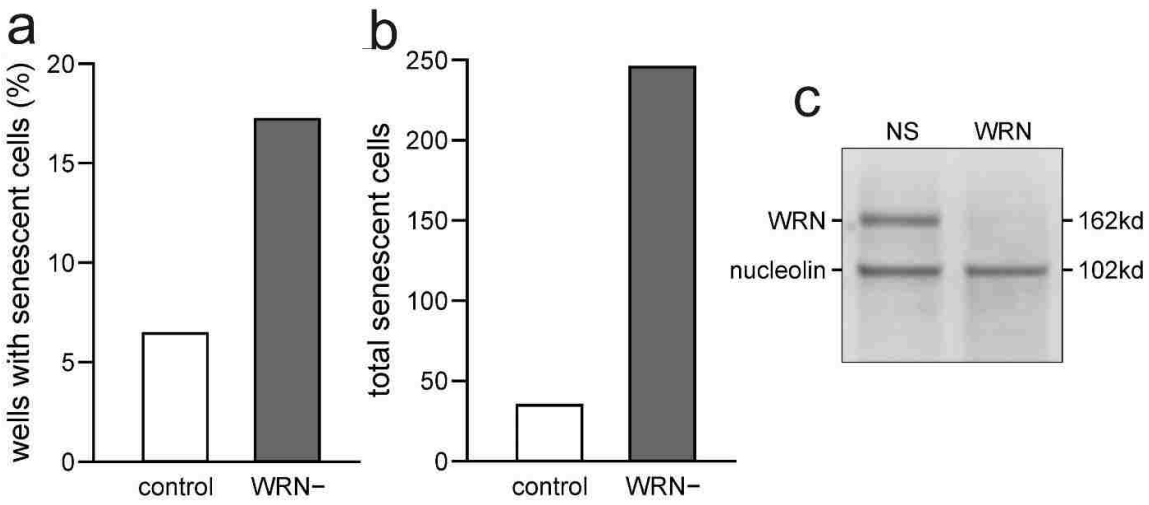

Figure 3.12: WRN depletion increases both the fraction of wells and total number of senescent cells in isogenic cell populations.

(a) Percentage of wells containing 1 or more senescent cell in WRN+/control and isogenic WRN-depleted microwell cultures. (b) Total number of senescent cells in WRN+ and WRN-depleted cell wells after 7 days in microwell culture. (c) Western blot verification of the extent of depletion of WRN protein in cells used for this experiment. Densitometry analysis revealed that lentiviral shRNA expression had depleted 90% of the 162 kDa WRN protein from cells used in this experiment. Control (WRN+) data were derived from 319 wells, and WRN-depleted data from 340 wells, each seeded with a single cell per well in 900-microwell arrays.

3.5.6 Modeling Reveals Growth Determinants in Microwell Cultures

Data on cell proliferation and senescence in microwell cultures begun from single cells allowed us to estimate the contributions of cell birth, senescence and death to overall microwell growth. From cell proliferation data, we were able to estimate the overall growth rate *r* for each well, using data from all wells (Fig. 3.13a) or only those wells with 1 cells on Day 0 (Fig. 3.13b). The results show a markedly bimodal distribution for both cell types (WRN+ and WRN-depleted), with a strong peak at $r = 0$ indicating no proliferation. The fraction of cells displaying no growth are typically never identified in population-based cell proliferation assays, but as these results demonstrate can be readily identified and quantified in microwell cultures as two starting populations with or without growth potential. The peak at $r = 0$ is higher when only wells with a single cell are included, since wells with multiple cells on Day 0 have a greater chance that at least one cell will proliferate. This analysis also clearly shows that a greater proportion of WRN-depleted cells never divide (26.3%) compared to control cells (17.2%), and that the

median *r* among WRN-depleted cells that do divide is smaller than that for control cells (~0.32 vs. 0.41). These results thus identify two different sources of lowered proliferation among WRN-depleted cells: a lower birth/division rate for cells which do divide, and an initially higher fraction of dead cells or senescent cells which never contribute to cell population growth.

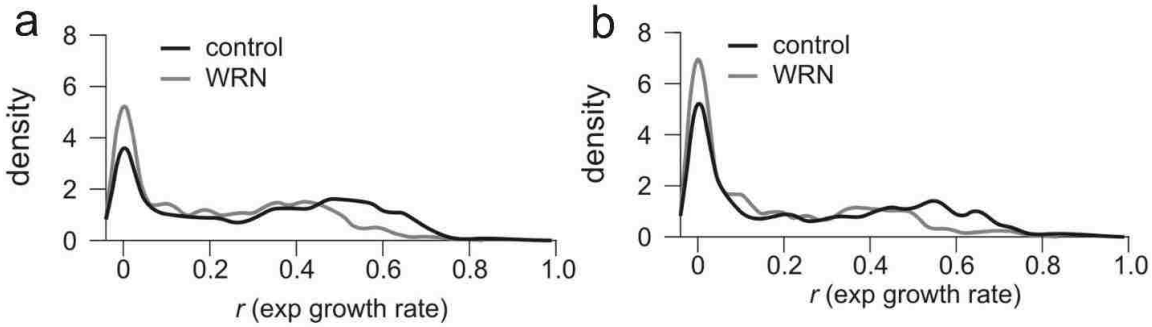

Figure 3.13: Distribution of estimated overall exponential growth rate '*r*' for microwell cultures.

Estimation was performed using data from all wells (a), or from only those wells that contained 1 cells on Day 0 (b). WRN-depleted cells show a higher proportion of cells which never divide, as well as a lower median growth rate among those which are able to divide.

We were able to deconvolute the growth rate *r* into its components using data from experiments in which we identified and counted senescent cells. The ratio of the number of senescent cells (r_2) to the number of living cells (r) is r_2/r. By assuming that r_2 from the second experiment (Fig. 3.11 & 3.12, in a 900 well microarray) also applies to the first experiment where cell proliferation data were generated in a 512 well array as shown in Figure 3.9, we can estimate the exponential growth rates which would have been observed in the absence of senescence. This allows us to compare the contribution of senescence for each cell type to the difference in observed growth rates for each cell type. More specifically, $(r_2/r + 1) \times r = r + r_2 = r_1 - r_3$ (r_1: birth rate, r_2: senescence rate, r_3: death rate) by removing the senescence rate from the overall exponential growth rate parameter. For WRN-depleted cells the ratio of senescent to viable cells r_2/r was estimated to be 0.015, while for WRN+ cells r_2/r was 0.114, which is more than 7-fold greater than for WRN-depleted cells. Similarly, we can estimate $(r_2+r_3)/r$ by the ratio of the number of wells with one cell that never divides to the number of wells with one cell

on Day 0 that do divide. Then r_1, the birth (division) rate is then given by $((r_2+r_3)/r +1)$ x r. Figure 3.14 shows the results to deconvolute *r*, the growth rate, to reveal the individual contributions of reduced proliferation and increased senescence to the overall lower birth rate of WRN-depleted cells versus isogenic controls (0.390 vs 0.300 for WRN+ and WRN-depleted cells, respectively). Cell death rates, in contrast, are comparable in the two cell populations. This analysis reveals how microwell data together with modeling can be used to reveal and quantify the differential contributions of cell proliferation, senescence and death to cell population gorwth over time, and thus identify changes in key determinants of population growth that may not be apparent from simple cell counts such as those shown in Fig. 3.14.

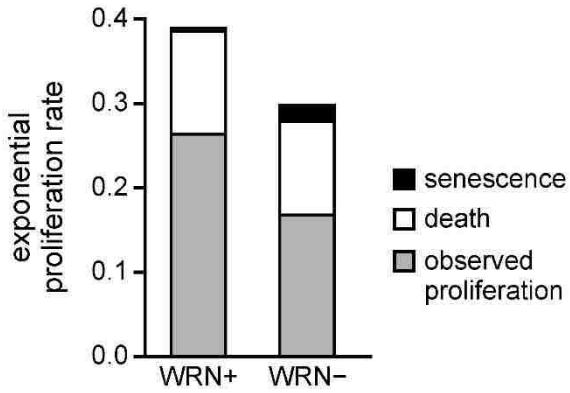

Figure 3.14: Deconvolution of microwell data to reveal determinants of the exponential proliferation rate.
The exponential proliferation rate *r* is = $r_1 - r_2 - r_3$ (birth rate – senescence rate – death rate). The exponential rate parameters for birth, r_1, are given by the overall height of the three segments. The estimated values of r_1, r_2 and r_3 for WRN+ cultures are 0.390, 0.004 and 0.122, and for WRN-depleted cultures 0.300, 0.034 and 0.110. Note that the overall height of the bars is the overall birth rate $r_1 = r + r_2 + r_3$.

Our goal in this chapter was to develop a microwell array that could be used easily with existing cell culture, imaging equipment, and protocols to quantify cell behavior across hundreds of individual cells during clonal expansion in culture. Our fabricated PDMS microwell arrays allowed the facile seeding and growth of hundreds of single cells in microwells under consistent conditions. Once seeded, microwell arrays are grown submerged in culture medium to insure uniform nutrient transfer and gas exchange across

all microwell cultures. The use of phase-contrast imaging in our system eliminates the need for additional cellular engineering to label cells with, *e.g.*, GFP-tagged proteins or the use of fluorescent or vital dye staining. The rapid analysis and counting of phase-contrast imaging data should progressively improve as better cell identification and counting algorithms are developed. The ability to rapidly generate quantitative multi-dimensional data on cells during clonal growth should provide a better understanding of key determinants of cell structure and function, and how these can be understood and controlled by genetic or chemical perturbations in culture. Thus our microwell approach should be useful for detecting and characterizing cellular heterogeneity during clonal growth in many cell types and for identifying drug effect to different types of cancer cells based on key cell behaviors.

Chapter 4. *Ex-vivo* Model Using Intact Tissue Slices or Biopsies

4.1 Summary

In this chapter, we focused on the methods for producing intact tissue slices and core tissue biopsies. We explain the techniques for tissue extraction, preparation and organotypic culture in detail. Then we demonstrated the culture viability of mouse brain slices and liver biopsies using liver/dead cell stain. We further investigated post tissue processing using a tissue clearing agent to overcome optical limitations and fixable staining agents to ensure the preservation of staining signal after tissue processing.

4.2 Introduction

In chapter 3, we developed a microwell cell array for a single cell clonal expansion study with a potential to study tumor heterogeneity. This approach allows for tracking cell behaviors from large numbers of single cells to provide quantitative information. However, the comparison of single cell behaviors may not be adequate for drug testing as the lack of stromal cells, ECM, cell-cell and cell-ECM communications raise concerns and the results from the drug screening techniques based on monolayers of cells might be physiologically irrelevant [19].

Increasing the complexity of the tissue culture systems will potentially increase the predictive power of the model for drug screening [88]. In the past two decades of research, studies have shown that growing cells in 3D reduces the gap between *in vitro* cell culture and *in vivo* tissues [19]. However, these still rely on cell lines or dissociated cells from primary tissues to build 3D models, often in matrices which are potentially unrepresentative of tissue origin. Tissue slice and biopsy cultures offer an attractive alternative as they preserve tissue in their native state and allow for the test drug to be added directly to the culture media. The intact tissue slices and biopsies have a high degree of physiological relevance and morphological structure compared to the original tumor environment, and furthermore, the drug testing results from this model can be produced fast enough to provide useful information for doctors before the treatment is given. In addition, a variety of techniques used for intact tissue culture have been

explored with consistent results. In this chapter, we focused on the common techniques to extract and culture intact tissue slices and biopsies. Mouse brains and livers were used to demonstrate the culture of slices and biopsies, respectively. Further, we investigated live tissue staining reagents that can provide reliable readouts of tissue viability.

4.2.1 Methods for Obtaining Intact Tissue Slices and Biopsies

4.2.1.1 Tissue Chopper

A tissue chopper is inexpensive and can rapidly produce tissue slices from a chunk of tissue. Therefore, it is an affordable and popular tool for research laboratories. However, the tissue slices produced using a chopper are typically thick (400 µm ~ 1 mm) and inconsistent. Hence, the chopped tissue slices are rarely for culture. Furthermore, a chopper with a carbon-steel razor blade is not suitable for sectioning soft tissues, as the chopping mechanism is not adjustable and usually jams the tissue while chopping.

4.2.1.2 Vibratome Tissue Slicer

The vibratome tissue slicer has a wide range in price with a major difference between manual and automated controls. While the system with more automated features requires less technical training, this difference should not affect the quality of the tissue slices obtained from a vibratome slicer. In the vibratome slicing technique, four major parameters (cutting angle, cutting speed, the oscillation frequency of the cutting blade, and the z-movement for thickness control) related to the slicing result can be finely adjusted. Normally, soft tissue types and/or thinner slices require slower cutting speed and higher oscillation frequency of the cutting blade. In contrast, harder tissue types and/or thicker slices have less requirements on these settings. The tissue mounting stage is usually located in the center of a chamber containing crushed ice in order to maintain the temperature while slicing, as the vibratome requires a longer time to produce tissue slices compared to a tissue chopper. The z-movement of the blade holder offers a higher degree of control in tissue slice thickness. Generally, a vibratome tissue slicer allows multiple degrees of manual controls and gives flexibilities for slicing tissues.

4.2.1.3 Precision-Cut Automated Tissue Slicer

The precision-cut tissue slicer provides high reproducibility and consistency to obtain tissue slices. The fully automated control of perfusion and slicing improves the slice consistency and decreases human error. The two most common and commercially available slicers for precision cut are Krumdieck and Brendel-Vitron tissue slicers. However, the main drawbacks are that these systems are expensive and have less flexibility in the control of operation.

4.2.1.4 Core Tissue Biopsies

A core tissue biopsy tool is a hollow needle with a cutting tip to draw a column of tissue out of a tissue chunk. The advantages of this technique are that it is quick and clinically relevant. The tissue core biopsy obtained from a biopsy tool can be directly cultured without any additional tissue processing, such as slicing. Therefore, it does not require additional labors which reduces the cost for the *ex-vivo* assay. However, the thickness of the tissue is restricted by the size (diameter) of the biopsy tool which is normally larger than 400 µm. Furthermore, small core biopsy tools only work for tissues with solid structures as the extraction mechanism is similar to a tissue chopper (acute slicing).

4.2.2 Methods for Culturing Tissue Slices and Biopsies

For intact tissue slice culture, several culture techniques have been established. Earlier culture methods using roller-tubes or Maximov-type chambers were described by Gahwiler [89] and Linder [90], respectively. In roller-tube cultures, the tissue is embedded in either a plasma clot or in a collagen matrix on glass coverslips and then undergoes continuous slow rotation in a tissue culture incubator. The slow rotation allows the tissue slice to be periodically submerged in the culture medium and exposed to the humidified air, allowing for sufficient nutrients and oxygen supply during culture. In tissue slices cultured in chambers and submerged in culture medium, continuous perfusion of oxygenated medium is required [57, 91]. The only oxygen source for tissue slice culture in this method is the oxygen dissolved in the medium solution, increasing the content of the oxygen in the medium allows for higher oxygenation to the tissue. More recently, a porous membrane used as an interface to maintain intact tissue slices has

become the most popular method. In porous membrane culture, the tissue slices are placed on a semi-porous membrane and the culture medium is only filled below the membrane. Both the porous membrane and the thin tissue slice are hydrophilic with very low water surface tension. Thus, the tissue is consistently moist and covered by a thin film of culture medium which is termed the air-fluid interface and allows for sufficient nutrient and oxygen supply to the tissue. The culture is stationary during the entire tissue culture process. Therefore, the culture technique can be easily adapted by research scientists.

All the techniques have shown the ability to retain the tissue architectures and various degrees of cell-to-cell interactions which do not exist in dissociated cell culture. The major difference between the various techniques is the final thickness of the tissue as each technique has its own limitations in terms of the diffusion of the nutrients and oxygen to maintain the viability of the tissue. For example, hippocampal slices cultured in the roller-tube technique thin down from an initial 400 μm to about 50 μm. In contrast, the same hippocampal slices cultured using the porous membrane interface method can retain the final thickness of 150 μm. On the other hand, the tissue types, anatomical origin of the tissue and the age of the animals affect the final thickness of the tissue slice [92] and are unrelated to the culture techniques.

Different culture techniques also serve different research purposes. Roller-tube culture is designed for experiments that require optimal optical conditions and access to individual cells, as the tissue slice becomes thinner and is culture on a thin glass coverslip. Porous membrane culture provides thicker tissue structures and is simple to use. If the experiment requires larger amounts of tissues and a higher level of cell-to-cell interactions with high accessibility of tissue manipulation, membrane culture should be the best choice. Cultures grown in medium-perfused chambers are well suited for short-term studies, such as recording from implanted electrodes or monitoring the electrical activity.

4.2.3 Assessment of Cell/Tissue Viability Using Vital Dye

Staining and imaging cells with vital fluorescent dyes is a highly versatile approach widely used among biologists. The diversity of commercially available vital dyes allows for microscopic analysis of multiple cellular parameters individually or combined. Many previous publications [93-95] have demonstrated the feasibility of using vital dyes to stain and image live tissue slices for qualitative and quantitative data collection. Therefore, we adapted this approach to characterize and verify the viability of our intact tissue slice and biopsy cultures.

4.3 Materials and Methods

4.3.1 Mouse Brain Handling and Slicing

Coronal mouse brain slices were prepared from E18~P7 embryonic or neonatal mice supplied by Charles Rivers Laboratories. Pregnant or neonatal mice were sacrificed in accordance with a protocol approved by the University of Washington Animal Care and Use Committee. Brain slices were prepared in ice-cold, Gey's balanced salt solution (GBSS; #G9779, Sigma, St. Louis, MO) supplemented with glucose (D-Glucose; G-6152, Sigma, St. Louis, MO) to a concentration of 7.5 mg/mL and bubbled with carbogen (5% CO2 and 95% O2) under sterile conditions. Mice were sacrificed by decapitation, and the brain removed and quickly immersed in ice-cold, carbogen bubbled ACSF prior to vibratome slicing (Vibratome Series 1000, Technical Products International, St Louis, MO). The cerebellum and inferior colliculus were removed with dissection scissors to create a flat tissue surface to allow vibratome stage mounting prior to slicing. A 6% rectangular agarose block was mounted on the vibratome stage using superglue as a wall for the whole mouse brain. Once the whole mouse brain was on the stage, ice-cold carbogen bubbled artificial cerebrospinal fluid (ACSF) was quickly transferred into the vibratome stage to immerse the whole brain. Crushed ice was used to surround the vibratome stage to maintain temperature during slicing with an uncoated razor (American Safety Razor Company, Verona, VA) to produce 300 µm thick brain slices. Figure 4.1 shows the process of vibratome slicer slicing a whole mouse brain to produce coronal mouse brain slices.

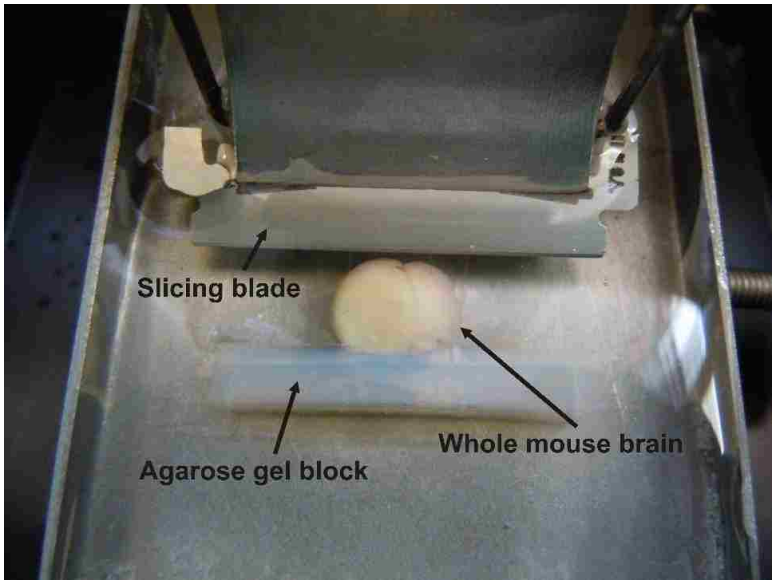

Figure 4.1. The process of a vibratome slicer slicing a mouse brain.
A glioblastoma multiforme (GBM) xenograft mouse brain (the tumor is on the left hemisphere of the brain, such that the size and the shape of the left and the right hemispheres are the same) was mounted on the stage and the blade mounted on the vibratome slicer was approaching the whole brain.

4.3.2 Mouse Liver Handling and Biopsy Extraction

Mouse liver biopsies with a diameter of 600 μm were prepared from adult mice. Adult mice were sacrificed in accordance with a protocol approved by the University of Washington Animal Care and Use Committee. Mice were euthanized by CO_2 at high concentration, and the liver was removed and quickly immersed in ice-cold carbogen-bubbled Williams E Culture Medium (WECM) prior to the biopsy extraction. The mouse liver has four distinct lobes interconnected with each other. Dissection scissors were used to separate the four lobes to allow for the biopsy extraction from individual lobes (while one lobe was being used, the other three were kept in ice-cold, carbogen bubbled WECM for maintaining their low metabolic activities). A 600-μm diameter core needle biopsy tool (#701120090, Angiotech, FL) was used to obtain cylindrical biopsy tissues (Fig. 4.2a). The liver tissue was placed on a flat and fibrous substrate, such as filter membranes or Kimwipes tissues, soaked in ice-cold WECM. The biopsy needle was then inserted horizontally through the tissue. Once the sliced area on the biopsy tool (Fig. 4.2b) was covered by the tissue, the back of the biopsy tool was pushed to initiate the slicing process (Fig. 4.2c). Once the slicing process was finished, the tissue was quickly slid off

biopsy tool. The biopsy tool was then reset by pulling the fire button and the biopsy tissue was appeared on the sliced area. The sliced area of the needle was quickly submerged in ice-cold WECM to allow the biopsy tissue slowly detach from the needle. The core needle biopsy tool can be reused as long as the quality core tissue biopsies can still be produced.

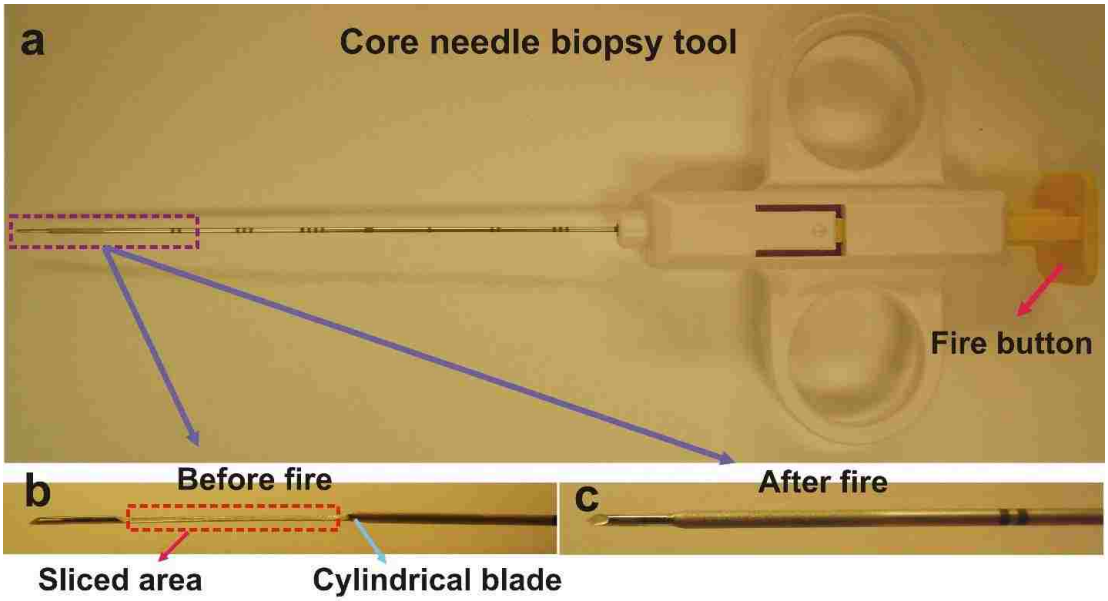

Figure 4.2. Core needle biopsy tool.
(a) A core biopsy tool with up to 18 mm penetration depth and 600-μm diameter. (b,c) Mechanism of extracting a core biopsy tissue. The biopsy tool is set to be (b), then inserted into a solid tissue. Once the sliced area is covered by the tissue, the fire button is pushed to trigger the cylindrical blade moving forward (from (b) to (c)) to slice a core biopsy tissue.

4.3.3 Organotypic Mouse Brain Slice and Mouse Liver Biopsy Cultures

Organotypic mouse brain slice cultures are well-established in neuroscience research and a variety of brain regions have been cultured with great success and consistency [96-100]. The common technique for tissue slice culture is the porous membrane interface culture that the tissue is placed on top of a hydrophilic porous membrane, the cell culture medium is placed below the porous membrane, and the tissue is in contact with humidified air to create an air-fluid interface and to allow oxygen and nutrient transport through the tissue. Compared to other tissue slice culture techniques which require

additional oxygen supply and medium perfusion, organotypic culture is under normoxia condition and is similar to the conventional cell culture routine.

Immediately after mouse brain slices and mouse liver biopsies were produced, the tissues were transferred onto porous membrane culture inserts using a 3-mm plastic transfer pipet (#357575, BD Bioscience, San Jose, CA) with the tip removed. Culture inserts were prepared and placed in a 6-well plate containing pre-warmed culture medium (1.2 ml medium/well/insert). For mouse brain slice cultures, the culture medium contained 75% neurobasal-A (#10888, Invitrogen, Carlsbad, CA), 25% horse serum (#H1138, Sigma-Aldrich, St. Louis, MO), Penicillin-Streptomycin (#P0781, Sigma-Aldrich, St. Louis, MO) and L-Glutamine (#G7513, Sigma-Aldrich, St. Louis, MO). For mouse liver slice cultures, the culture medium was made by adding 5 ml of 2 mM L-Glutamine, 5 ml of 10 mM Hepes, 5 ml of 5 µg/ml ITS, 5 ml of Penicillin-Streptomycin, 1.2 µL of 10 mM dex and 2ml of 250 µg/ml Fungizone into 500 ml WECM. Once the tissue is positioned on the porous membrane, the surrounding solution was removed by gent aspiration using a 20 µL or 100 µL pipet to create an air-fluid interface. The slices and biopsies were then cultured in a tissue culture incubator. Full volume of culture medium was replaced every two days for the mouse brain slices and half volume of culture medium was replaced every three days for the mouse liver biopsy tissues.

4.3.4 Porous Membrane Properties

Two most commonly used porous membranes, polyester (PET) with pore size of 0.4 µm (BD, MD) and hydrophilic polytetrafluoroethylene (PTFE; PICM0RG50, Millipore, Billerica, MA) membranes, were used to test organotypic mouse brain slice and liver biopsy cultures.

PET porous membranes are track-etched from a thin film of hydrophilic PET material with control over pore size and pore density to determine their physical properties (Fig. 4.3a). In contrast, hydrophilic PTFE membranes have a mesh-like topography and fibrous structure with high permeability and porosity, which helps transport nutrients across the whole surface of the tissue slice (Fig. 4.3b). Both porous membranes are biocompatible,

optically transparent (wet hydrophilic PTFE membrane) and have been used for organotypic slice cultures. Both track-etched (PET) and fibrous (PTFE) membranes have average pore sizes of 0.4 µm, however their permeability, microtopography and surface chemical groups are completely different, which make them very different tissue culture substrates.

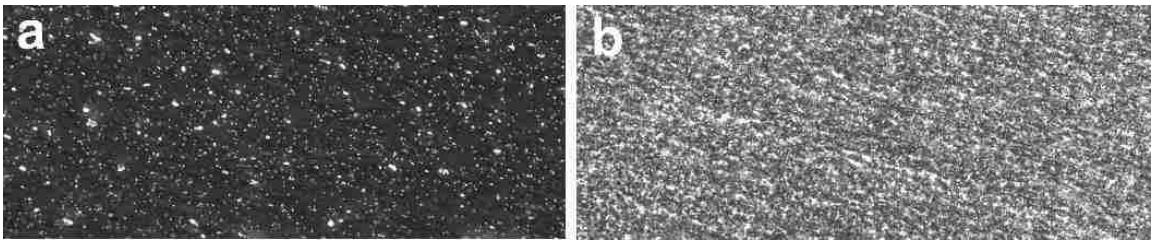

Figure 4.3. Porous membranes.
(a) track-etched PET porous membrane (pore size: 0.4 µm). (b) Fibrous PTFE porous membrane (pore size: 0.4 µm)

4.3.5 Cell Viability Assay

For live cell staining, we use calcein-AM which is a cell-permeable molecule that is converted by intracellular esterases into a calcium-binding, highly fluorescent molecule as a live cell indicator. The live cells labelled with calcein-AM normally express high intensity of green fluorescence throughout the full cell bodies/membranes.

For dead-cell staining, cell-impermeable nuclear binding dyes (the dyes can only enter into the cells with compromised cell membrane) such as EthD-1, propidium iodide (PI), and Sytox Green are commonly used to label dead cells. These dyes are high-affinity nucleic acid stains that are weakly fluorescent until bound to DNA after which they emit fluorescence more than 30-fold brighter. Fixable dead cell stain is the other type of dead cell staining and is slightly different than the nuclear binding dye. This dye is also cell-impermeable, but instead of binding to DNA, the dye reacts with the proteins of the cell. For viable cells, because the dyes cannot enter the cell membrane, only the proteins on the exterior surface of the cell are available to react with the dyes which results in dim staining. For dead cells with compromised cell membrane, the dyes can penetrate through the membranes and stain both intra- and extra- cellular proteins resulting in higher

intensity from the staining. The fluorescence intensity from fixable dead cell stain is about 50-fold greater in live cells than in dead cells.

To access cell apoptosis, Cell Event Caspase-3/7 Green Detection Reagent (CellEvent™) was used to detect apoptotic cells. The reagent is a four amino acid peptide (DEVD) conjugated to a DNA-binding dye; the DEVD peptide sequence is a cleavage site for caspase-3/7 and the conjugated dye is non-fluorescent until cleaved from the peptide. Fixable dead cell stain and Cell Event Caspase-3/7 are compatible with both live cell fluorescence-imaging and paraformaldehyde (PFA)-based fixation methods. Therefore, after staining and prior to imaging, the tissue can be fixed using 4% PFA.

To stain the tissue slices or biopsies, we rinse the tissue three times with PBS prior to applying the staining solution. The staining solution is prepared by mixing the calcein-AM and EthD-1 solutions in PBS at a final concentration of 2 µM and 4 µM, respectively. Once the tissue is rinsed, the staining solution is applied to label the tissue at room temperature for 45 minutes. The tissue is then rinsed again three times with PBS before imaging. For other staining dyes (Sytox Green, PI, Fixable dead cell stain, and CellEvent™), 1 µM in PBS would be an adequate concentration for tissues following the same staining procedure.

4.3.6 Image acquisition

Tissue slices and biopsies were imaged in a glass-coverslip bottom chamber (#12565336, Fisher Scientific, Pittsburgh, PA) using a Nikon Eclipse Ti inverted microscope (Nikon Instruments, Melville, NY) with epifluorescence illumination. An automated x-y stage and both 4X and 10X objectives were used to acquire fluorescent images. Individual images were focused manually and all the images were acquired with a 12-bit cooled CCD camera (ORCA-ER, Hamamatsu, Japan). Nikon NIS-Elements AR software was used to control image acquisition.

Confocal images were obtained using a Zeiss LSM 510 confocal microscope (Carl Zeiss, Thornwood, NY) with a 20X objective. The thickness of optical sections was 2.2 µm,

based on the longest excitation wavelength of the fluorescent channel. Two fluorescent channels were set to the same optical thickness. The z-scan function was used to define the surface (0 μm) of the tissue slice, then confocal image was acquired at the focal plane of 10 μm above the bottom tissue surface.

4.4 Troubleshooting

Tissue handling and slicing are critical processes in organotypic slice culture. Keeping the tissue "ice cold" and "sterile" are two essential keys throughout the preparation, dissection, and tissue slicing process. A thermometer can be used to monitor temperature of the dissection solution throughout the process (the temperature should always be below 4ºC). If the thermometer is not used or unavailable, small ice cubes made of dissection solution should be prepared and placed in the dissection solution during the slicing process. If the dissected tissue requires travel (less than 1 hr), the tissue should be stored in a 50-ml tube with ice-cold medium slightly covered and with the lid loose to maximize the oxygen supply.

As the mouse brain is directly mounted on the stage, it is difficult to slice the lower part of the brain tissue as the vibratome blade holder will be in contact to the bottom of the stage. In this case, a thin piece of agarose gel can be mounted on the stage to elevate the brain tissue.

All models of vibratome tissue slicer provide certain controls of the cutting angle, speed, and oscillation frequency of the blade. From our experience, a slower cutting speed and higher oscillation frequency produce the best results. However, a slower cutting speed will prolong the slicing process and a high oscillation frequency will increase risks of damaging the tissue either from the physical contact through the blade or the heat generated from the oscillation. Generally, vibratome tissue slicer takes longer time for producing quality tissue slices. Therefore, it is important to maintain oxygenation and ice-cold condition during slicing.

Once tissue slices and biopsies are produced, tissue transferring can be tricky and requires some practice. As the tissue slices and biopsies are thin (300~600 μm) and fragile, moving tissues by physical contact is almost impossible and normally damages the tissues. Therefore, it is important to transfer the tissue using a transfer pipet with the tip cut to increase the aspiration area. The aspiration generated from a transfer pipet allows the tissue with the solution to be aspirated into the pipet. The tissue is protected by the solution while being transferred without physically contacting the pipet. When placing the tissue on the membrane, angle the tip of the transfer pipet down to allow the tissue to settle at the bottom of the tip by gravity. Then a droplet is created by gently pushing the transfer pipet. As the tissue slice is settle at the bottom, the tissue slice should be within the droplet. Simply allow the droplet to be in contact with the culture membrane (culture substrate), the tissue slice with the droplet should be instantly transferred and attached on the top surface of the membrane. Once the tissue is settled on the membrane, the residual solution surround the tissue is gently aspirated. If the tissue slice or biopsy is not at the desired position on the membrane, gently place few drops of dissection solution on top of the tissue and manipulate the solution to control the movement of the tissue.

Despite the organotypic culture technique is simple, there are few steps which require extra attentions. First, organotypic slice culture requires that the tissue be cut into a thin slice (200~400 μm) such that mass transport of nutrients and oxygen is not diffusion-limited (i.e., it must be sufficiently small in at least one dimension). Second, it is important to have an adequate amount of medium filled below the culture membrane. For example, in a 6-well plate, each well should contain 1~1.2 mL of culture medium below the membrane well insert. Third, any excessive amount of solution on top of or around the tissue should be aspirated off as much as possible to create a proper air-fluid interface. If the tissue is covered by too much solution, the tissue will encounter insufficient oxygen supply during culture. To aspirate the solution around the tissue, it needs to be extra gentle and careful to avoid any possible damages to the tissue. The damage may come from the strong aspiration or physical contact from the tip of the transfer pipet. Fourth, organotypic slice culture is sensitive to humidity of the

surrounding culture environment. Tissue slices dry out very quickly when expose to outside of a cell culture incubator as the humidity is significantly lower than the environment inside an incubator (20% outside an incubator; 85% inside an incubator). When the culture is needed for medium change or other required steps outside of an incubator, it is important to reduce the process time and place the culture back into an incubator as soon as the process is finished. Fifth, the tissue morphology should be monitored daily using an inverted microscope to ensure the quality of culture and to avoid any possible contaminations.

About the tissue staining, calcein AM staining for live cells is relatively unstable and the fluorescence intensity decreases rapidly during imaging. Therefore, the tissue should be imaged right after staining with short duration. Sytox Green is extremely bright and highly sensitive to cells with compromised cell membranes. Even live cells with minor damages on their cell membranes, the cells will be stained with Sytox Green, causing false negative results. Therefore, we do not recommend the use of Sytox Green as a dead cell indicator.

In organotypic mouse brain slice culture, the slice shows partial transparency under an inverted light microscopy because of the thin thickness. This partial transparency allows us to quickly estimate the slice culture condition. For example, if there are black dots forming in the tissue slices over time during culture, most likely that the tissue slices have been contaminated. Therefore, the tissue slices should be taken off immediately to avoid further contamination to the culture incubator.

4.5 Results and Discussion

4.5.1 Thin Tissue Slices and Small Core Biopsies for Organotypic Cultures

We were able to obtain coronal mouse brain slices in a reproducible manner without the need of tissue embedding. From each embryonic or neo-natal mouse brain, we were able to obtain at least six 300-μm thick slices for organotypic culture. In addition to the thickness of the slice, the size of the slice is defined by the outline of the mouse brain. The first couple of slices are generally small as the cutting location of the brain is towards

the olfactory bulb with smaller outline and the following slices are bigger as the outline gets bigger towards the central cortex regions. For the mouse liver biopsy, we were able to extract multiple core biopsy tissues, particularly from the largest lobe of the mouse liver. The mouse liver biopsy is roughly 500 μm in diameter and 1~1.5 cm in length. Figure 4.4 shows the mouse brain slices (Fig. 3a) and a mouse liver biopsy (Fig. 3b) cultured on PTFE membrane well inserts.

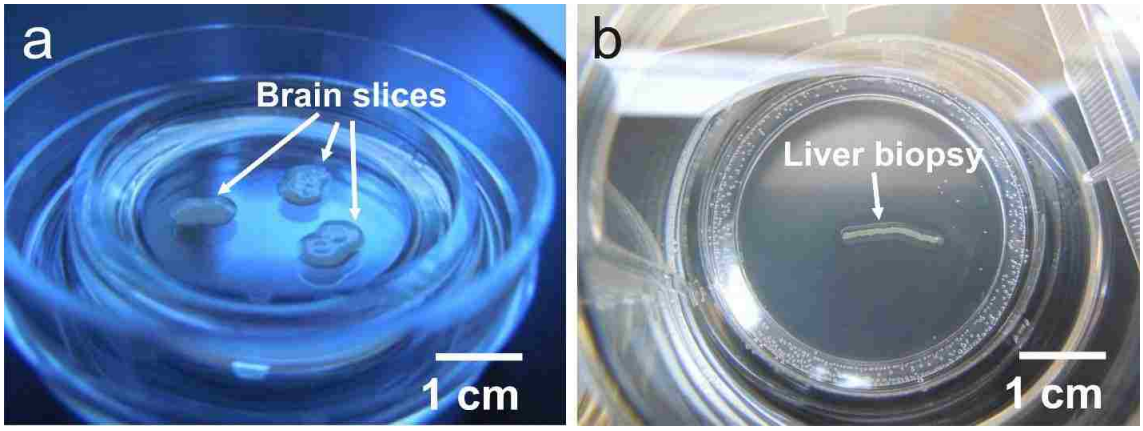

Figure 4.4. Organotypic intact tissue cultures.
(a) Three coronal mouse brain slices were cultured on a PTFE membrane well insert. (b) A mouse liver biopsy was cultured on a PTFE membrane well insert. Both intact tissue slices and biopsies were covered by a thin film of culture medium as an air-fluid interface.

A whole mouse brain has a proper size and geometry. Therefore, a mouse brain can be directly mounted on the stage for slicing without any additional process, such as tissue embedding. For other types of tissues with flat or undefined structures (like mouse livers or tumors), agarose embedding technique is necessary for the tissue preparation before slicing. Low-melting temperature agarose gel should be used for tissue embedding, as the melting temperature is typically below 30 ^{o}C, to minimize the damage to the tissue caused by the high temperature. Once the tissue is embedded and the agarose gel is solidified, the structure can be easily shaped and mounted on the stage. Agarose gel surrounds the tissue chunk gives a support during slicing. Therefore, quality slices can be produced even for the tissues with undesired shapes or structures.

Here we demonstrate the process of handling and obtaining tissue slices and biopsies from mouse brains and livers, respectively. The same methods should also work for other types of tissues with minor adjustments.

4.5.2 Porous Membrane Properties Have Direct Effects on Viability of Tissue Slice Cultures

Interfacing with a semi-porous membrane is a common approach for organotypic slice culture. However, little is known about the importance of the material on the viability of the tissue cultured on it. The difference in porous membrane properties to an intact tissue slice culture has barely been discussed in the previous publications. Here we investigated the effect based on the properties of the membranes to the slice culture condition by comparing the viability of mouse brain slice cultures.

Two most commonly used porous membranes for organotypic slice culture are track-etched PET and hydrophilic PTFE membranes. We tested both membranes for organotypic mouse brain slice culture with identical culture conditions. As a result, we discovered that a mouse brain slice cultured on a hydrophilic PTFE membrane provides significantly better viability than cultured on a PET membrane as shown in Fig. 4.5.

The result of the difference in viability between the two types of membranes has been consistent with multiple repeats. We believe that this may be because the medium transport is significantly more efficient through PTFE than PET. This culture condition with an air-fluid interface above the tissue only allows for the culture medium to be supplied from the bottom. Hence, the ability to transport the medium to the tissue through the porous membrane is critical. For track-etched PET membranes, the medium supplied from the bottom is only able to reach the tissue through the track-etched pores, the density and the size of which are usually minimized to remain optical clarity through the membrane, but may result in insufficient medium transport. In contrast, PTFE is a fibrous material and thus the pore size and the porosity of PTFE membranes are defined by their material properties. This PTFE material wicks in medium and holds it within its fibrous structure to allow for the supply of medium to the tissue in a uniform manner. This

uniform supply is likely to provide sufficient medium transport. Moreover, the topography of the material from PTFE is likely to improve cell attachment, resulting in an enhanced viability. Thus, these dissimilar properties and permeability (mesh-like vs track-etched) of the two membrane materials may affect the medium transport and determine tissue viability in organotypic culture.

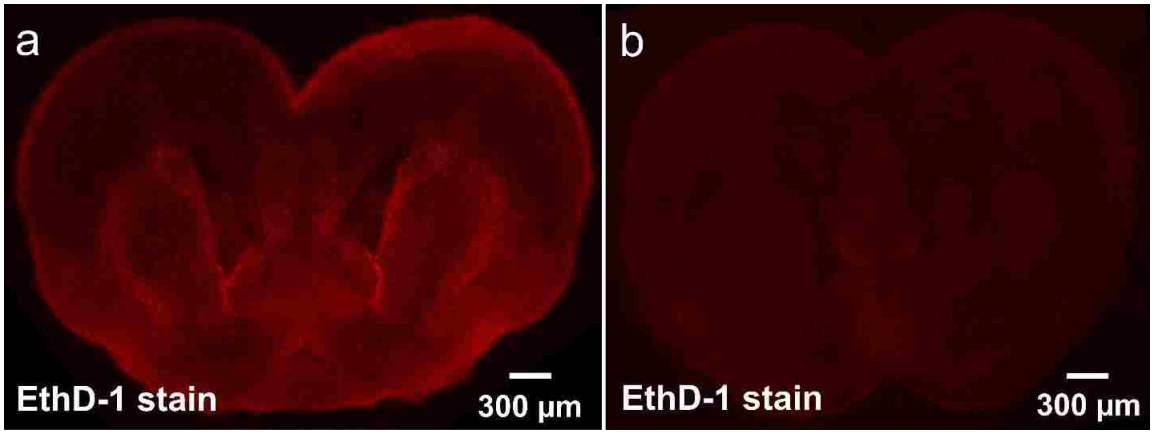

Figure 4.5. Epifluorescence images of coronal-cut live mouse brain slices stained with EthD-1.

Images of mouse brain slices cultured on a PET (a) and a PTFE (b) membranes for 48 hours and stained with EthD-1. Damaged cells can be easily distinguished from healthy cells with the staining of EthD-1, resulting in high fluorescence intensity in cell nuclei. (a) The mouse brain slice cultured on a PET membrane had excessive amount of EthD-1 nuclear stains, indicating that the slice was not in a healthy condition. (b) The mouse brain slice cultured on a PTFE membrane only had few EthD-1 nuclear stains, indicating that the slice was in a healthy condition.

Furthermore, we conducted the confocal microscopy to visualize the tissue slice viability. The use of celcein-AM and EthD-1 together provides both positive and negative indicators of cell viability, allowing for the collection of data related to quality control method for tissue viability. This simple method allows for determining whether cell membranes have been compromised. From our confocal readouts, the mouse brain slice cultured on a PTFE membrane shows higher viability with more calcein-AM and less EthD-1 stains than the one cultured on a PET membrane as shown in Fig. 4.6.

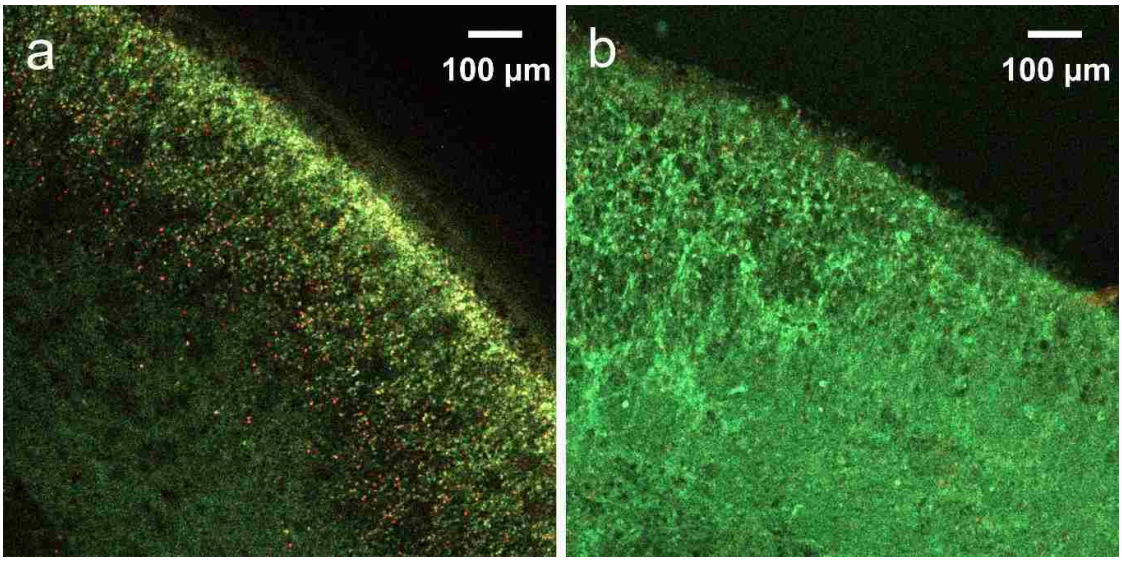

Figure 4.6. Viability comparison of brain slice culture using PET and PTFE membrane well inserts.

E18 mouse brain slices were cultured on PET porous membrane (a) and PTFE porous membrane (b) under the same culture condition. After 3 days in culture, calcein AM (green) and EthD-1 (red) were used to determine the viability of the brain slices. Confocal microscopy was used to acquire staining outcomes. The calcein-AM/EhtD-1 overlay above clearly show that the viability of brain slices is vastly superior in slices cultured on PTFE membranes (b) than in those cultured on PET membranes (a).

In addition to the comparison of the bare PET and PTFE porous membranes, we have also tested different types of ECM coating (Poly-D-lysine & Matrigel) on the PET porous membrane surface to enhance the culture. Poly-D-lysine surface coating enhances the cell/tissue attachment by providing monolayers of positively charged molecules on the culture surface. Matrigel surface coating forms a thick gel layer on the porous membrane surface and allows for the fluid transport to be evenly distributed within the gel layer before reaching to the tissue slice. As a result, we found that Matrigel coated PET porous membrane improves the viability of the brain slice culture. However, PTFE membrane is still significantly better in providing the optimized slice culture condition.

4.5.3 Long-Term Mouse Brain Slice and Liver Biopsy Cultures

For drug testing experiments, the length of drug exposure requires anytime from few hours to few days. In addition to drug exposure, the freshly dissected slices usually require 24~48 hour culture for recovery prior to being used for experiments. Therefore, it

is important to evaluate the culture condition for extended period of time. To address this long-term culture condition, we examined the viability of the mouse brain slices after a week of organotypic culture. As a result, the slice remained highly viable as the calcein-AM stained (Fig. 4.7a) throughout the full slice and less regions of cells were stained by EthD-1 (Fig. 4.7b).

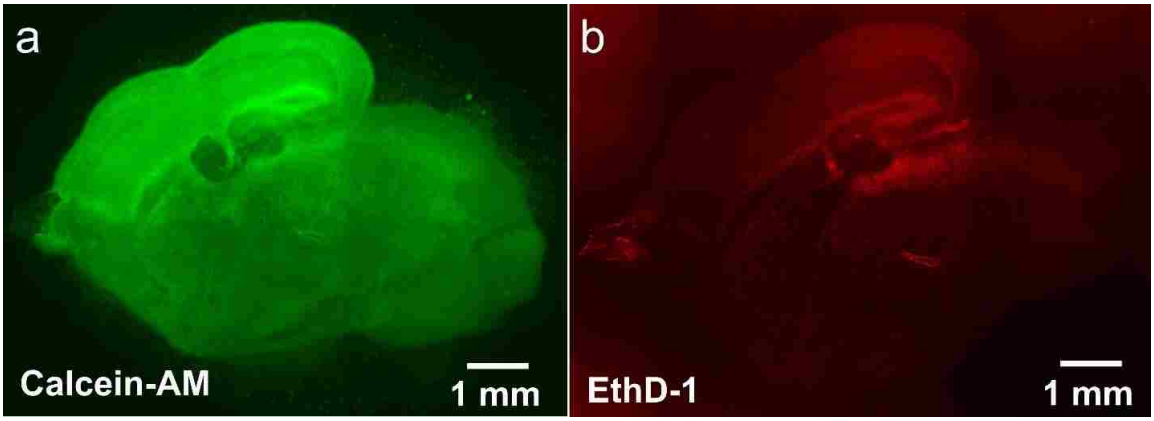

Figure 4.7. Long-term organotypic mouse brain slice culture.
A sagittal-cut mouse brain slice was stained with calcein-AM (a) and EthD-1 (b) after 7 days of culture. Noticeably, there is a small region of the brain slice excessively stained by EthD-1, indicated the large amount of cell death. However, the cause of the cell death at the specific region might not be from the culture technique as the rest of the areas in the brain slice remains healthy (unstained). We think that the potential causes might be because of the severe damage from the initial dissection or the certain anatomical region of the cells which is difficult to survive under the *ex-vivo* culture.

For mouse liver slice and biopsy cultures, the freshly extracted core mouse liver biopsies and mouse liver slices were directly placed on PTFE membrane well inserts under organotypic culture. Interestingly, the culture condition requires different medium change interval and takes longer period of time for the tissue to recover. From our experience, the culture medium should not be replaced until the third day of culture and should not be replaced in full volume. The reason might be because the liver tissue secrets growth factors which are essential to support its own viability and is sensitive to any change of the culture environment. Based on both assumptions, the culture medium should only be replaced partially at each medium change interval. Furthermore, we also found that the viability of the tissue does not reach to an optimal condition until a week of culture, indicating that the difference in tissue/cell type requires its own unique culture strategies.

Figure 4.8a-d shows the PI staining of core mouse liver biopsies (500 μm in diameter) after 24 hr (Fig. 4.8a) and 96 hr (Fig. 4.8b) culture. A significant improvement of tissue viability with less PI stained cells throughout the core biopsy tissues was found after 96 hours of culture. Figure 4.8e-h shows the PI staining of mouse liver slices (400 μm thick) after 1 (Fig. 4.8e), 3 (Fig. 4.8f), 4 (Fig. 4.8g), 7 (Fig. 4.8h) days of culture with half volume of culture medium changed once every 3 days. A gradual improvement of the slice viability demonstrates the requirement of long recovery time for liver tissue cultures.

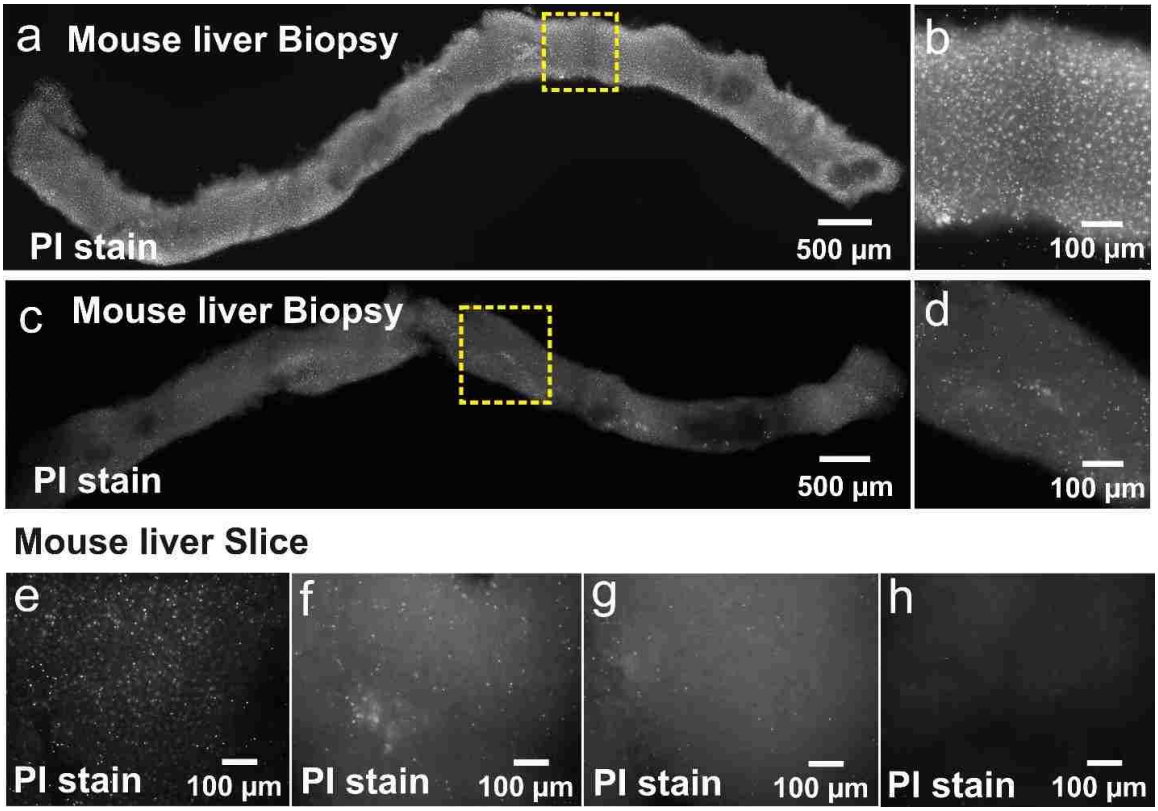

Figure 4.8. Intact mouse liver tissue cultures.
(a) Mouse liver biopsy after 1 (a-b) and 4 (c-d) days in culture and stained with PI. (e-h) Evaluation of mouse liver slice viability after 1 (e), 3 (f), 4 (g), 7 (h) days of culture.

4.5.4 Increasing Optical Penetration Using Tissue Clearing Agents

For intact tissue slices or biopsies, the thickness of which is normally between 300 and 600 μm right after slicing or biopsy extraction. Even though the slice normally becomes

thinner after few days of culture, the final thickness of the slice is likely to be no less than 150 µm. In order to observe the inner layer of the tissue, confocal microscopy is required for acquiring spatially defined images from the tissue sample without disrupting the integrity of the tissue slice (the use of confocal microscopy allows defining a focal plane and enabling the reconstruction of three-dimensional structures rather than the epifluorescence microscope which can only acquire and identify the images from x and y-axis). However, confocal does have limitations in the depth of optical penetration (~50 µm from our test). Even though optical penetration depths of up to 150 µm have been reported, repeated experiments show that we are only able to obtain 50 µm penetration depths with clear images through our tissue slice samples.

In recent studies, intact tissue clearing to enhance the optical penetration with minimum signal degradation has been an attractive technique. This technique enables optical reconstruction of an intact tissue and gives precise spatial information without requiring tissue sectioning. Many tissue clearing reagents have shown impressive signal stability and optical penetration. ScaleView™ from Olympus, pioneered by Miyawaki and colleagues at Riken, is one such well-established tissue clearing agents composed of 4 M urea, 10% glycerol, and 0.1% Triton X-100, which has shown excellent preservation of fluorescent signal and the optical penetration [101] (Fig. 15a-d). Furthermore, improved techniques with enhanced preservation of fluorescent signal and tissue structure have been introduced recently, using the reagents ClearT [102] and Clarity [103]. This tissue clearing technique allows us to detect stained cells throughout an entire tissue slice using confocal microscopy.

Figure 15 shows the optical penetration using confocal microscopy from a 300-µm thick fixed mouse brain slice before (Fig. 15a) and after tissue clearing (Fig. 15b). The slice becomes partially transparent and can be seen through by naked eyes. To further investigate the use of tissue clearing agent for confocal imaging, 300-µm brain slices from a transgenic Tau-green fluorescent protein (GFP) mouse were used for the measurement of optical penetration. As a result, the tissue clearing agent greatly improved the optical penetration by at least 6 folds (Fig. 15c,d).

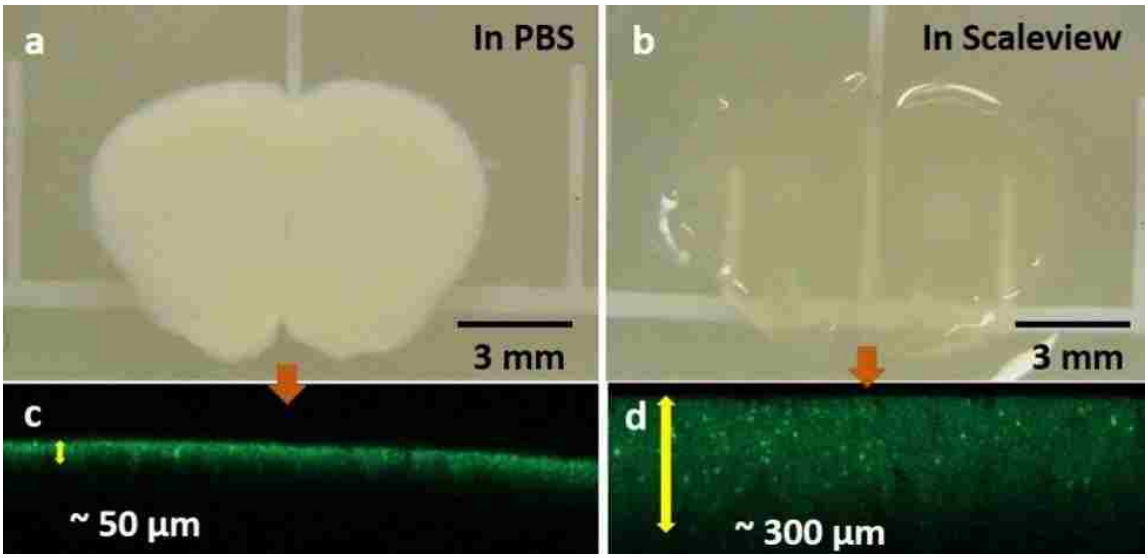

Figure 4.9. Tissue clearing increases optical penetration.
(a) PFA fixed GFP mouse brain slice preserved in PBS showed optical penetration of ~50 µm using confocal microscopy. In comparison, (b) the same GFP slice preserved in ScaleView showed a >6 fold optical penetration.

4.5.5 Vital Dye Staining Remains Stable after Tissue Fixation and Clearing

The current dead cell staining reagents (EthD-1, PI, Sytox Green), impermeable to the cell membrane in live cells and bind to DNA after passing through the compromised membrane of dead cells, are incompatible with the tissue fixation. Even though the tissue slices are normally rinsed with PBS 3 times before tissue fixation, these staining reagents can still leach out over time. Furthermore, small amount of residual staining solution can still stain the fixed cells causing strong imaging background. To resolve this issue, we demonstrate a fixable dead cell staining reagent which reacts with cellular amines on mouse brain slices. The requirement of chemical reaction with live cellular amines avoids additional staining after tissue fixation. In addition to the dead cell staining, we demonstrate the stability of the cell apoptosis staining reagent (CellEvent™) on mouse brain slices after tissue fixation. Figure 4.10 shows that both Fixable dead cell stain and CellEvent™ not only the staining results remain almost identical, but have great signal preservation after tissue fixation. Overall, we demonstrated the use of these two fixable reagents to detect cell death and cell apoptosis, respectively, allowing for the tissue slices

to be imaged after the tissue fixation and clearing without concerns of false positive staining.

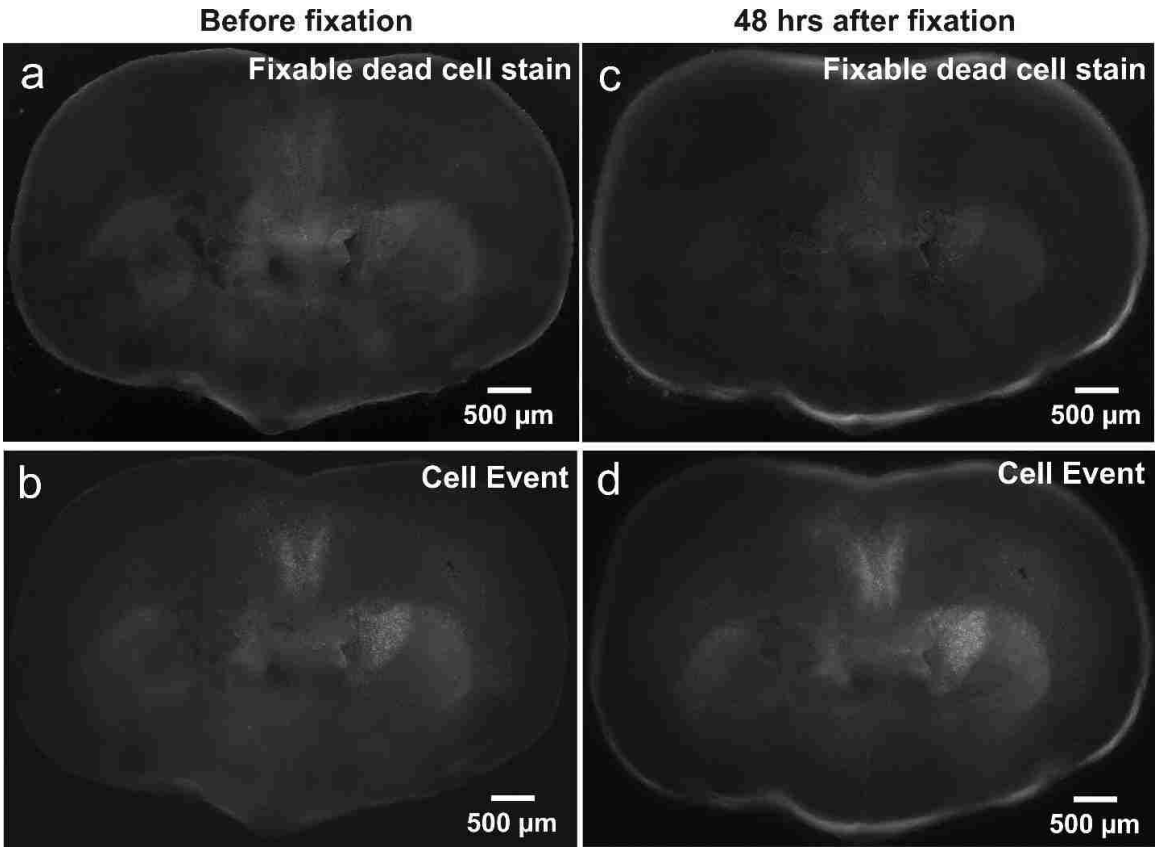

Figure 4.10. Stability of vital dyes after tissue fixation.

(a-b) A 300-µm thick coronal mouse brain slice stained with Fixable dead cell stain (a) and CellEvent™ (b) showing the original dead cells and apoptotic cells detected by the staining. (c-d) After tissue fixation overnight and tissue clearing for 48 hours, the stained results from both reagents were well preserved. All the images above were acquired using epifluorescence microscopy.

Chapter 5: A User-Friendly Microfluidic Device for Delivering Large Numbers of Drugs on Organotypic Tissue Slice Cultures

5.1 Summary

In this chapter, we demonstrated a microfluidic device that permits regioselective delivery of biomolecules with spatiotemporal control in slice culture. We explain the key designs of using a 96-well plate as an inlet interface and integrating with a porous membrane for organotypic slice culture in the device. We described the fabrication process in detail and demonstrated the operation of the device. We further explain the fluid transport in our microfluidic platform by both simulations and experiments. Additionally, we demonstrated two extended applications to show the potential of utilizing this microfluidic device for different biological studies.

5.2 Introduction

5.2.1 Motivation

In the past two decades, microfluidic devices have been utilized as powerful tools for high-throughput drug screening [104]. However, the majority of these device designs focused only on dissociated cell cultures [105, 106]. In the past few years, several devices have been developed to incorporate intact tissues into microfluidic devices. The lack of good culture platforms [59], requirements of complicated external equipment and setups [62], and the inability to spatiotemporally control fluid delivery [107, 108] are major hurdles to the application of microfluidics to intact tissue culture. Therefore, our goal is to overcome these challenges in utilizing intact tissues to develop a user-friendly microfluidic device for drug screening on live tissue slices or biopsies.

5.2.2 Fabrication of Microfluidic Device

In the current fabrication for microfluidic devices, PDMS has been the most widely used material due to its unique properties, including biocompatibility, optical transparency, and low cost. The use of SU8 photoresist to allow for fabricating high aspect ratio microstructures [109] and the invention of soft lithography [110] accelerated the use of PDMS and enabled rapid prototyping of microfluidic devices. Furthermore, the

discoveries of PDMS-PDMS bonding by oxygen plasma treatment and PDMS-plastic bonding by silane coupling [80] allowed for the fabrication of complex devices. Therefore, using PDMS for micro-device fabrication with the existing techniques still possess enormous potential.

5.2.3 Microchannel Resistance

Microfluidics is known for having low Reynolds numbers, resulting in laminar flow where viscous forces are dominant [111]. Because of the low Reynolds number, the Navier-Strokes equations describing fluid mechanics can be simplified and the calculation of the flow rate and microchannel resistance can be described as electrical analogy (Ohm's Law). In Ohm's Law, R = V/I (R: resistance, V: voltage, I: current). In microfluidic channels, the flow-driven pressure P can be seen as V and the volumetric flow rate Q can be seen as I. Therefore, the equation can be written as R = ΔP/Q.

In our microfluidic channels fabricated using SU8 and photolithography, the cross-section of the microchannels is rectangular. Therefore, the fluid resistance can approximately follow the equation below, where R is hydrodynamic resistance, L (m) is the length of the channel, w (m) is the width of the channel, h (m) is the height of the channel, and μ is the viscosity of the fluid [112].

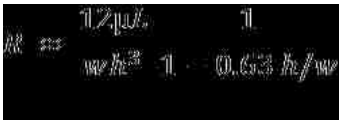

To calculate a network of channels interconnected with one another in our device, the equivalent resistance can be computed as the sum of individual channel resistances as shown below (the device has 80 sets of channels and the sum of the resistance (R) in each set (R_1+R_2+R_3…) can be calculated and adjusted individually as shown below; by balancing all channel resistances, the flow rates are balanced as well.

$$R = R_1 + R_2 + R_3 + R_4 + \cdots$$

5.2.4 Microfluidic Inlet Interface

One of the advantages of microfluidic device is the ability to deliver large numbers of reagents within a miniaturized fluidic chip which contains microchannels designed for functional applications. This fluid delivery in microchannels only requires small volumes of reagents, allowing for the reduction of costs for each experiment. However, large numbers of inputs normally lead to excessive amounts of tubing and reservoirs used for inlet connections and typically require complex external pressure sources [113] for operation (Fig. 5.1a). This complex interface results in one-time use devices with low reproducibility and time-consuming experimental setup. An innovative method using a vacuum-sealed manifold allowing for the operational interface to separate from the microfluidic device has been reported [114] (Fig. 5.1b). Nevertheless, fine alignment requirements, complicated manifold setup, and the potential effects of vacuum on cell cultures limit this approach. In this chapter, we demonstrate a simplified chip-to-world interface by integrating a 96-well plate into our device for the ease of operation, requiring only the pipetting for reagent loading (Fig. 5.1c). This well-plate platform is also compatible with the majority of microscopy systems without the need for customized stage holders.

Figure 5.1. Microfluidic inlet interfaces.
(a) Traditional operation of a microfluidic device. (b) Customized manifold as a plug-and-play interface. (c) All-in-one microfluidic device.

5.2.5 Finite Element Analysis: Comsol Modeling

Physical systems can be analyzed by deriving differential equations relating the variables of through basic physical principles. However, once the physical principles are formulated, the mathematical equations are normally impossible to solve analytically. Finite Element Modeling (FEM) allows one to interpret a complex mathematical model

as a series of components of simple geometry (mesh). Each component is expressed in terms of a finite number of degrees of freedom. All the individual components are resolved prior to being combined. Therefore, a complex system can be seen as a combination of multiple simple components and the physical phenomenon can be simulated based on the definitions of physical conditions in the system.

5.3 Materials and Methods

5.3.1 Device Fabrication (Fig. 5.2)

A 96-well plate-based microfluidic device was fabricated using soft lithography, PDMS replicas, oxygen plasma for PDMS-PDMS and PDMS-glass bonding, and silane coupling for PDMS-plastic bonding. The device was assembled from 4 parts including a modified bottomless 96-well plate, a PDMS interface layer, a PDMS channel network layer, and a thin microfluidic chip.

5.3.1.1 Bottomless 96-Well Plate

A square reservoir was created in the center of a Greiner bio-one clear bottomless 96-well plate (#82050, VWR, Radnor, PA) by cutting and removing the center 16 wells, leaving the surrounding 80 wells to serve as input reservoirs, followed by edge scraping to give a smooth surface across the bottom of the plate.

5.3.1.2 PDMS Interface

A PDMS block containing 3-mm holes was exclusion molded from a master fabricated using 0.25” thick acrylic sheets (Small Parts, Logansport, IN) cut using a CO2 laser (Universal Laser Systems, Scottsdale, AZ). Two laser-cut acrylic sheets were assembled using a thin double adhesion mylar sheet: a 5.6” long, 3.75” wide, 0.25” thick block, and a rectangular frame with outer dimensions of 5.6”x3.75”x0.25” and inner dimensions of 4.5”x2.9”x0.25”. Uncured PDMS (mixed at 1:10 crosslinker:prepolymer ratio) was poured in the rectangular master and a thin release liner sheet (3M, St. Paul, MN) was sandwiched between the master and the acrylic block. Two rectangular metal blocks were used to sandwich the full structure and a no-twist C-clamp (#5046A18, McMaster-Carr,

Santa Fe Springs, CA) was used to compress the sandwich structure for exclusion molding by baking at 70 °C for at least 4 hours. After the PDMS was cured, the sandwich structure was disassembled and the rectangular PDMS block was created by detaching the cured PDMS from the master. Next, the rectangular PDMS replica was aligned and attached to the bottom surface of a bottomless 96-well plate. A colored marker was used to mark the center of individual well reservoirs on the PDMS replica. Further, a 3-mm Harris Uni-Core biopsy punch (Ted Pella, Inc., Redding, CA) was then used to create an array of holes following the marks. Finally, a square block was cut off from the center of the PDMS replica to match the modified bottomless 96-well plate.

5.3.1.3 PDMS Channel Network

For fabrication of the PDMS channel network master molds, two silicon wafers were spin-coated with SU-8 2075 photoresist (Microchem Co., Newton, MA) at 3000 rpm to pattern microchannels using single layer photolithography. After two SU-8 masters were made, laser-cut acrylic sheets (outer dimension: 4" diameter, 0.125" thick, inner dimension: outline of the microchannel design and 0.125" thick) were adhered to the silicon wafers to define the PDMS replica shape. Exclusion molding was then used to create a uniform thickness of the PDMS replica (the thickness of the PDMS replica is defined by the thickness of the acrylic sheets). Once the PDMS channel network replicas were made, a 0.5-mm biopsy punch was used to punch through the PDMS replica to connect well reservoirs and through the PDMS channel interface and network to the microfluidic chip.

5.3.1.4 PDMS Microfluidic Chip

Multilayer photolithography and PDMS exclusion molding [79] were used to fabricate the PDMS microfluidic chip. Delivery channels were patterned with a 60 µm thick layer of SU-8 2075 (spin-coated at 2000 rpm) on a silicon wafer. Next, an additional 220 µm thick layer of SU-8 was spin-coated to pattern inlets, outlet, and open channels on the silicon wafer. After photolithography, the SU-8 masters were hard baked at 200℃ on a hotplate. Masters were then coated with fluorinated-trichlorosilane (#448931, Sigma, St.

Louis, MO) using several drops of the silane solution in a desiccator under vacuum. Exclusion-molding was then used to produce a 280 µm PDMS microfluidic membrane with open inlets, outlet, and channels. The SU-8 master mold was placed on a 4" diameter, 0.5" thick steel disk. Uncured PDMS (9:1) was mixed, degassed, and then poured onto the master. A sheet of polyester film was treated with oxygen plasma and placed onto the uncured PDMS. Air bubbles trapped within the SU-8 features and uncured PDMS were scraped off using a razor blade. Four additional sheets of polyester film and two 75 mm x 50 mm x 1 mm glass slides were stacked on top of the mold to add compliance to the stack. Finally, a steel disk was placed on top and the assembly was compressed using a no-twist C-clamp prior to baking at 70℃ for at least 2 hours in a convection oven. After disassembly, the PDMS replica was peeled off along with the sheet of polyester film, then bonded on a 65 mm x 48 mm x 0.15 mm glass coverslip using oxygen plasma followed by removal of the polyester film. Open features (inlets, outlet and channels) were checked with a dissection tweezer under a Nikon SMZ 1500 microscopy (Nikon Instruments, Melville, NY). Scotch packaging tape (3M, St. Paul, MN) was then used to cover the glass surface area outside of the PDMS replica.

5.3.1.5 Device Assembly

Bonding of PDMS to PDMS and to glass is done by oxygen plasma treating surfaces using 60 W at 670 mTorr for 60 s, and at 40 kHz RF from a Zepto plasma system (Diener Electronic GmBH, Ebhausen, Germany). Bonding of PDMS to PS plastic (bottomless 96-well plate) is done by silane coupling using (3-aminopropyl)triethoxysilane (#A3648, APTES, Sigma, St. Louis, MO) to modify plastic surfaces prior to bonding with oxygen plasma treated PDMS at room temperature [80]. The order of assembly was bottomless 96-well plate and PDMS interface, followed by two PDMS channel network parts that were carefully aligned and bonded onto a PDMS microfluidic chip. These two assembled components were then bonded together to complete the four layer device. A simple outlet was created by cutting a cube of PDMS with a 0.5-mm punch followed by bonding onto the outlet port of the PDMS microfluidic chip by oxygen plasma. Finally, uncured PDMS (1:9) was carefully dripped into gaps between channel network parts to fill gaps prior to curing on a hotplate at 80℃ for at least 1 hour.

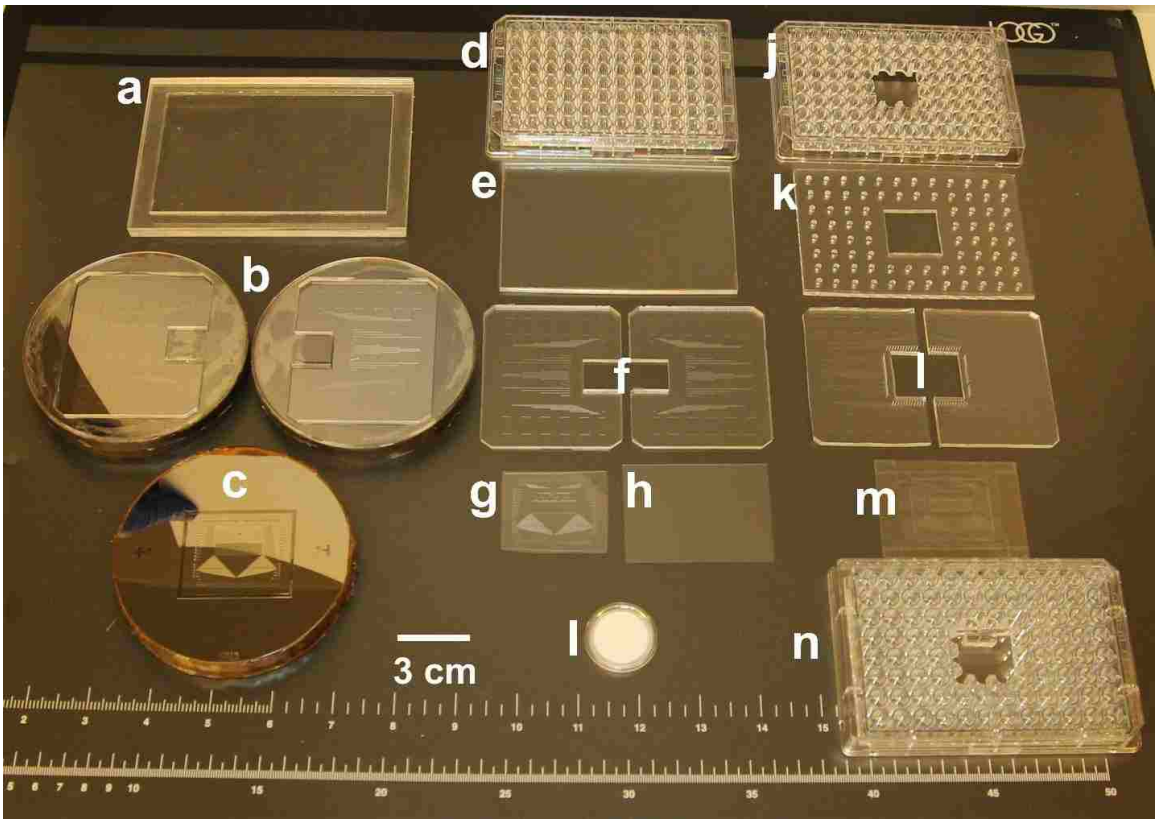

Figure 5.2. Individual parts of masters and PDMS molds.
(a) Acrylic master for molding PDMS interface layer. (b) Masters for channel network layers. (c) Master for microfluidic chip. (d) A bottomless 96-well plate. (e) A mold of a PDMS interface layer. (f) Molds of PDMS channel network layers. (g) Exclusion-molded PDMS microfluidic chip layer. (h) A glass coverslip. (i) PTFE porous membrane well insert. (j) Modified bottomless 96-well plate. (k) Modified PDMS interface layer. (l) Modified PDMS channel network layer. (m) PDMS microfluidic chip. (n) Completed 96-well plate-based microfluidic device.

A 96-well plate lid with a 4-mm hole above the outlet port was used as a cover for culture experiments. A 19 gauge, 0.5" long metal pin and 1 inch segment of Tygon tubing (Cole Parmer, Vernon Hills, IL) was then connected in the outlet port to complete the device.

5.3.2 Integration of Porous Membrane in Microfluidic Device for Organotypic Culture

In conventional microfluidic devices for cell/tissue culture applications, the cells and tissues are directly cultured in the device and attached to the substrate that is permanently bonded to the device. One critical step in microfluidic cell/tissue culture application is the

cell/tissue loading process which requires microfluidic expertise. This requirement causes the difficulty of microfluidic devices being adapted by general scientists. To address this issue, the designs of the microfluidic devices for cell/tissue loading, culture and operation should consider the user friendliness.

Here we demonstrate an easy method to transfer the PTFE membrane (with intact tissue slices attached) to the top of the open microchannels, which closes the roof of the microchannels. This transfer can be easily done by cutting the membrane from the PTFE membrane well insert with the tissue slice cultured on the top and then placing it in the device (the PTFE porous membrane must fully cover the open channels). This method relies on the paper-like (wicking) properties of the PTFE material which has a very low surface tension; the PTFE establishes an excellent seal with a PDMS substrate when the membrane is fully wet.

Using this membrane transfer technique, the tissue slices can be cultured on the commercial membrane well insert prior (Fig. 5.3a) to being transferred to our microfluidic device for drug screening (Fig. 5.3b). Once the drug exposure process is finished, the tissue slice can then be moved to a glass coverslip-bottom chamber for further tissue staining and imaging (Fig. 5.3c). Since the transfer process allows to move the culture substrate rather than the tissue alone, the contamination from the culture substrate is minimized. Because of this membrane transfer technique, the device can be rinsed and reused as long as the delivery channels are not clogged.

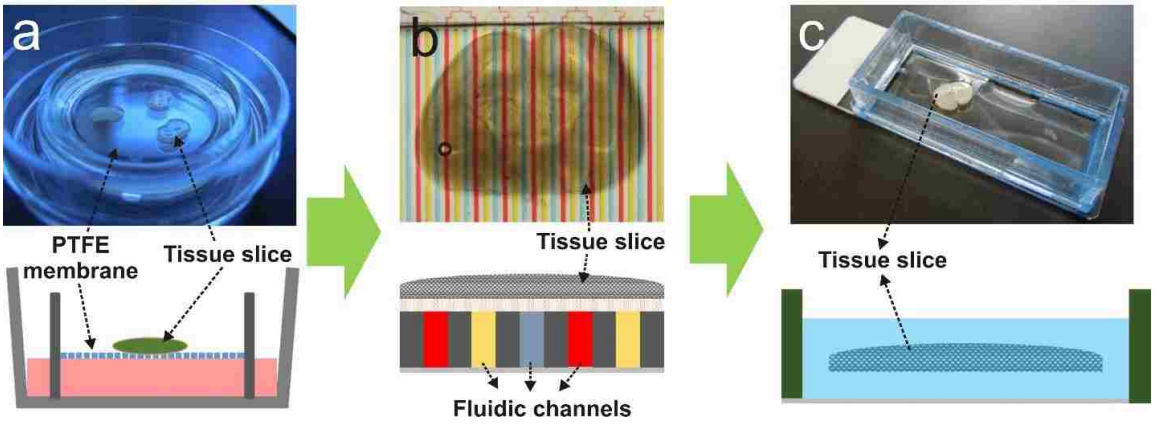

Figure 5.3. The PTFE membrane transfer technique. The bottom schematics represent the cross-sections of the top images.

(a) Tissue slices organotypically cultured above a hydrophilic PTFE porous membrane in a well insert. (b) The membrane with the tissue slice can be cut and transferred to our microfluidic device for multiplexed drug exposure. (c) The tissue slice can be removed from our device and transferred to a glass coverslip bottom chamber, where the slice can be processed for all of the standard pathology protocols of tissue staining and imaging.

5.3.3 Device Operation

The assembled microfluidic device was treated with oxygen plasma using the same conditions for bonding for sterilization and hydrophilization prior to use. Immediately after the plasma treatment, the device was transferred to a cell culture hood and microchannels were filled by pipetting culture medium into well reservoirs, covering the open channels with a PTFE membrane and then applying suction to the outlet. Once microchannels were filled, the device was left in a cell culture incubator for 1 hr to allow culture medium to temperature and pH equilibrate prior to use. Tissue slices were transferred from the culture membrane well insert by first cutting PTFE membrane and placing it onto the open microchannels of the device. The full culture area of the device (80 parallel open channels) was imaged to register the position of tissue slices relative to delivery channels. The solutions in the well reservoirs in respect to the delivery channels beneath the tissue slices were then replaced with the delivery agents with the desired spacing. Flow was initiated by connecting the device outlet to a 20 ml syringe (#302830, BD Bioscience, San Jose, CA) and syringe pump (Fusion 200, Chemyx Inc., Stafford, TX) to ensure a flow rate of 300~1200 µL per hour.

5.3.4 Colored and Fluorescent Molecules for the Observation of Fluid Transport

In order to test the fluid transport in the microchannels and in the porous membrane, we used three different colors of food coloring dye (FD&C Red #3, FD&C Blue #1 and FD&C Yellow #5, Spectrum, NJ) to observe the fluid transport. To further quantify the fluid transport result, fluorescein (#71980, Riedel-de Haen, Germany) with the concentration of 100 mM in distilled water was used in the device.

To observe the transport of biomolecules in an intact tissue slice, Hoechst 33342 (blue), Sytox Green (green), and EthD-1 (red) were used as nuclear staining reagents. Hoechst 33342 is cell-permeable and can stain both live and dead cells. In contrast, Sytox Green and EthD-1 are cell-impermeable and can only penetrate and stain the cells with compromised cell membranes. In our fluid transport observation study, we used fixed tissue slices, therefore, cell permeability of the dye is not a concern.

5.3.5 Diffusion Modules in Comsol Modeling

The Comsol Free and Porous Media Flow module approximates porous matrix properties of brain tissue slices with a constant porosity of 0.4, a permeability of 1×10^{-11} m^2, and a tortuosity of 1.5 [115]. The Transport of Diluted Species module was used to define the concentration sources and sinks at the selected microchannels with fluorescein (M.W. = 332 Da) as the diffusing species (diffusion coefficient (D) = 5.7×10^{-10} m^2s^{-1}) to simulate concentration profiles in tissue slices.

5.4 Troubleshooting

SU8 negative photoresist is the most commonly used material to create micro-scale features on silicon wafers for PDMS molding. Even though detailed fabrication method has been written on the manufacture's data sheet (MicroChem), we still encountered many problems during the SU8 master fabrication. Here we provide few solutions from the common and poor outcomes of the SU8 masters based on our experiences. (1) If the SU8 features came off from the silicon wafer during the last developing step, it is normally because of the wafer baking process or the lack of UV exposure for crosslinking the SU8 material. Baking is essential in the SU8 fabrication process, it helps to solidify the SU8 material. However, it is also the major issue causing the detachment of SU8 features from the silicon wafers, because of the difference in thermal expansion between the SU8 and the silicon wafer. In this case, we recommend to slowly ramp the temperature up and down during the baking process to reduce the thermal expansion. Regarding the lack of UV exposure, carefully check and calculate the exposure energy from the photolithography machine to ensure the regular efficiency from the UV lamp. In

general, the temperature ramp should be slow (1 ^{o}C/min) at each baking process and the UV exposure should reach the exact exposure energy as recommended from the manufacturing data sheet. In addition to the thermal expansion and UV exposure, two minor reasons in causing the SU8 detachment are from the initial surface condition of the silicon wafer and the original product of the SU8. For the concern of the wafer surface condition, treat the surface with oxygen plasma to ensure an absolute cleanness of the surface before coating. If the feature detachment remains unresolved, then the problem likely comes from the original product of the SU8 and requires a complete replacement. (2) The other common failure is an incomplete developing of SU8 features. The issue usually happens when there are two features too close to each other with relatively high aspect ratio. The features supposed to be etched away by the SU8 developer were either partially cross-linked during the UV exposure process or the developer was not able to sufficiently etch the uncross-linked SU8 because the narrow path between the cross-linked features. In both cases, sonicating the developer bath while developing the SU8 wafers for a short duration (1~3 minutes) should be tested. However, sonicating the wafers can potentially cause the detachment of the SU8 features.

Modifying plastics by machine drilling, laser cutting, and melting at a high temperature results in rough surfaces and edges. This unevenness of the surfaces causes issues of bonding the plastic surface to the PDMS. We resolved these issues by scrapping off the uneven edges from a 45 degree angle to smooth the edges and to create an even surface.

PDMS exclusion molding technique to create "open" features is a tricky process. It requires the design and fabrication of the SU8 master, fine tune of the sandwich structure, adequate attachment between the polyester film and the PDMS, and the high pressure to compress the structure for molding. It is particularly important to use adequate amount of polyester films as compliances for the exclusion molding. More polyester films need to be used if the features are not excluded. If the feature was partially excluded with only a thin film of PDMS, tweezers with fine tips can be used to clean the PDMS film under a stereo microscopy.

For the assembly of the device, it is important to check the evenness, smoothness and cleanness of each layers before bonding. If the surface of the PDMS layer is not clean, 3M shipping tapes can be used for cleaning before plasma treatment. All the layers should be bonded right after oxygen plasma treatment and placed on a 70 ^{o}C hot plate for at least 5 minutes to enhance the bonding strength. Check the bonding strength at each bonding process to ensure the best outcome of the device.

From our previous experiments, we have not encountered any contamination issues caused by the device. However, the contamination can always be a concern as our microfluidic device is not fabricated under a sterile environment. To increase the sterile culture condition, exposing the device with UV light to minimize the concern of the contamination. This step can be done by using the UV lamp in the cell culture hood to expose the device overnight.

The membrane transfer technique requires to cut the PTFE membrane off from the well insert. This cutting process requires a sterile and sharp knife in order to cleanly separate the membrane without stretching during cutting. As stretching the membrane can easily damage the tissue slice cultured on the membrane, it is highly recommended to use a new cutting blade every time for this cutting process. Furthermore, practicing in cutting the wet membrane off the well insert will help the cutting process in the real experiment.

5.5 Results and Discussion

5.5.1 Leak-Proof 96-Well Plate-Based Microfluidic Device

Here we demonstrate a microfluidic platform that allows for selective delivery of fluids to an organotypic slice at a large number of pre-defined locations. Delivery of drugs occurs through a removable porous membrane that rests on top of a set of microchannels. Each microchannel is fed by a 400 µL reservoir that, given the low flow rates of microchannels can provide up to two days of uninterrupted reagent delivery. After reagent delivery, the membrane (with slice attached) can be removed for imaging and analysis.

The platform features a "tubeless" input interface based on 96-well format (inspired by work from Brian Cunningham's group [116]). The central 16 wells from the 96-well plate have been removed to create a culture area, while the remaining 80 wells serve as reservoirs (inputs) in our device (Fig. 5.4). As opposed to other interfaces based on tubing and connectors, this familiar, user-friendly interface allows users to pipet panels of up to 80 solutions into the device for screens. With this microfluidic organotypic culture, solutions move through channels on the bottom surface and then travel or diffuse upwards through the tissue.

Our microfluidic device for slice cultures was fabricated by using a combination of multilayer soft lithography, exclusion molding [79] and PDMS-to-plastic silane bonding [80]. Upstream of the delivery/culture area, each microchannel is individually connected to a different reservoir well of the modified 96-well plate, containing a drug of choice (Fig. 5.4a-b). Downstream of the delivery area, all the microchannels are connected to a common outlet via a binary arbor which the flow rate is typically controlled with a syringe pump. The delivery microchannels, initially "roofless", are separated by PDMS walls. The PDMS walls are designed to sit underneath a PTFE porous membrane. When a wet PTFE porous membrane is placed onto the open microchannels, capillary forces cause the membrane to adhere to the PDMS surface; the membrane then becomes the "roof" for the open microchannels. Negative pressure applied to the outlet increases the PTFE membrane adhesion to the PDMS surface and causes a slow flow under the membrane, allowing for the diffusive supply of nutrients to the tissue. All the microchannel resistances (and thus flow rates) are designed to be equivalent across all microchannels, which were achieved by varying microchannel widths according to their lengths.

All the PDMS and plastic components in the 96-well plate-based device (except the porous membrane) are irreversibly bonded to produce a leak-proof platform (Fig. 5.4c-d). This 96-well plate platform results in a device that is easy to transport, and is compatible with standard imaging systems.

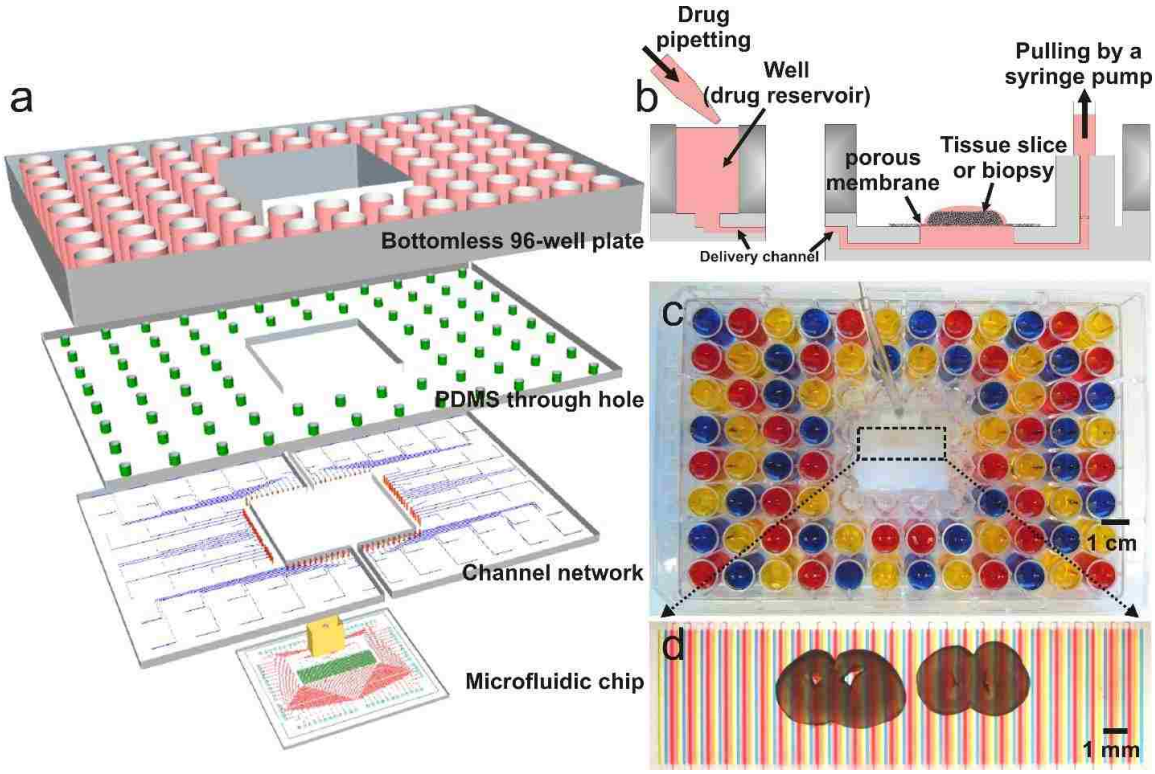

Figure 5.4. Microfluidic device design.

(a) Layer-by-layer schematic view of the device. The device includes (from top to bottom) a modified bottomless 96-well plate featuring 80 inlet wells after the central 16 wells have been removed; a PDMS through hole layer; a PDMS microchannel network layer; and the microfluidic chip (where the porous membrane with the tissue is placed). (b) Cross-sectional schematic of the device. The device is operated by gravity flow and the total flow rate is driven by a syringe pump through a common outlet: one syringe pump is able to control flow across all 80 fluidic streams. Tissue slices are cultured on a PTFE porous membrane. The wet membrane seals the open microchannels by capillarity, which allows for fluidic stream transport of culture medium to tissue. (c) Micrograph of the microfluidic platform loaded with three dyes (yellow, blue and red) in sequence to generate an alternating pattern of yellow, blue and red microchannels across the perfusion membrane (d). Micrograph of the tissue culture area after loading the platform shown in (c) with a porous membrane that has two mouse brain slices attached.

To initially demonstrate the concept of fluid transport, we chose food-coloring dyes to deliver into the channels and monitor the dye transfer through the porous membrane to the tissues after the channels were rinsed with clear PBS solution. In both mouse brain slices (Fig. 5.5) and liver biopsies (Fig. 5.6), we observed highly selective dye transfer patterns on the tissues.

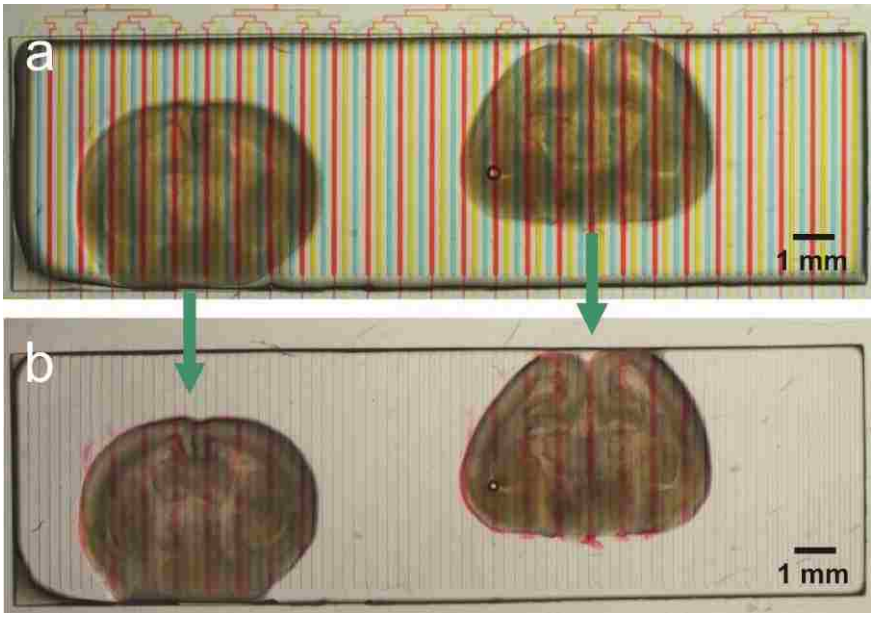

Figure 5.5. Micropatterning using coloring dyes on tissue slices.

Micro-streams can be patterned in tissue slices through the porous membrane. The streams can be formed and quickly flow through the porous membrane, leaving the food coloring dye on the mouse brain slices. The total delivery time of dye exposure is 20 minutes. After the delivery channels were rinsed with clear phosphate buffered saline (PBS), the colored stains were still visible on the slices. The dye transfer from the blue and yellow streams is not obvious on the image because the initial concentrations of the dye streams were low. Moreover, the tissue slices have a strong background which makes it even harder to see the transferred colors.

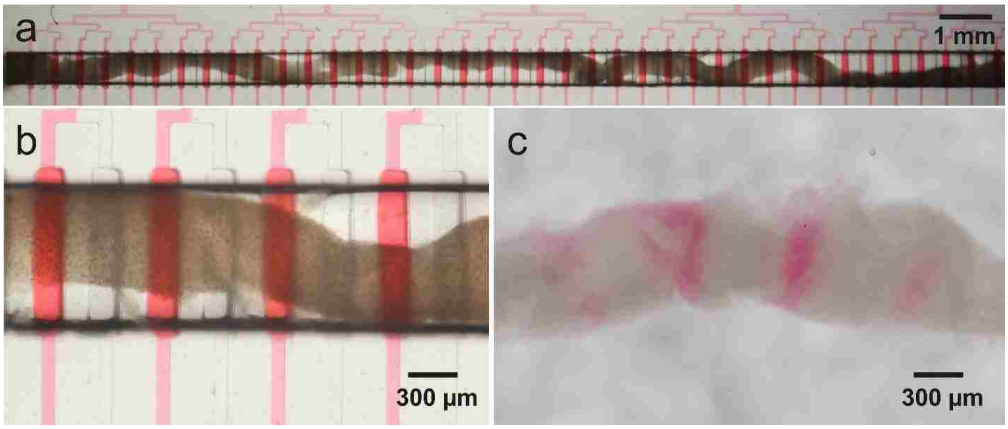

Figure 5.6. Perfusion of core tissue biopsies from mouse liver using our microfluidic device.

(a) Two mouse liver biopsies were extracted and placed in our microfluidic device while the red colored streams were delivered underneath the biopsy tissues. (b) After red colored dye was flowed and flushed with HBSS, (c) the dye selectively transferred from the bottom streams into the liver biopsy.

Our 96-well plate-based device only has one outlet at the downstream of the delivery area where all the microchannels are connected through a binary form. Therefore, the flow control of the device can be as simple as using a pump to generate negative flow rate or pressure. Furthermore, it is also possible to run flow by gravity to a lower common reservoir (syphon) as shown in Fig. 5.7. Relying on this physics of syphoning, our device can be operated and the flow streams can be formed without any additional flow-driven equipment.

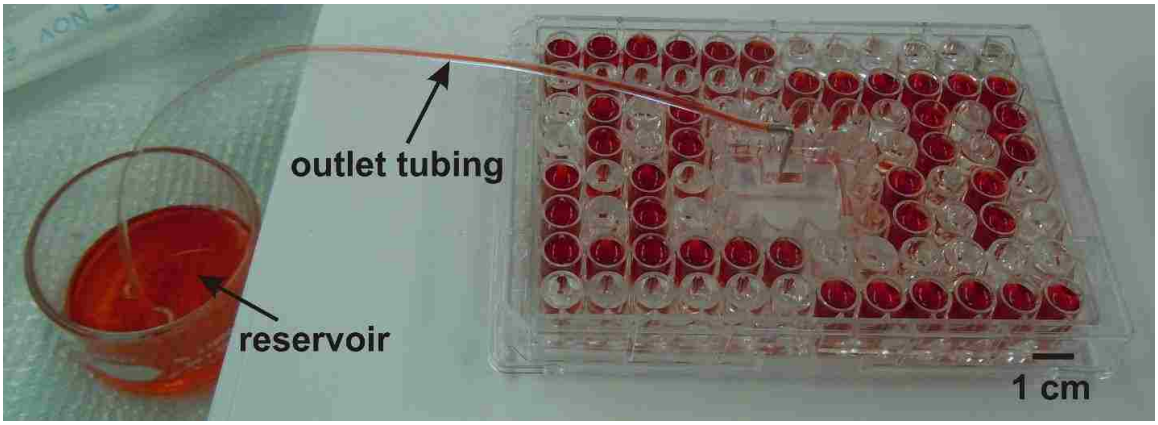

Figure 5.7. Operation of the device by syphon.
A tubing connected to the device outlet conveyed liquid down to a lower level of a reservoir.

5.5.2 Long-Term Organotypic Tissue Slice Culture in a Microfluidic Device

Our microfluidic device is designed to closely mimic the organotypic culture method with the following differences. First, the full surface area on the bottom side of the membrane is evenly in contact with the culture medium bath in the conventional organotypic culture. In our microfluidic device, only 2/5 of the surface area (open channels) on the bottom side of the membrane is in contact with the culture medium. The rest of the surface area is in contact with the solid PDMS materials (gaps in between the channels). Second, the culture medium is static beneath the porous membrane in the conventional organotypic culture. In comparison, our microfluidic device has continuous flow within the delivery channels underneath of the porous membrane. In both cases, the contact between the porous membrane and the medium maintains the wetness of the

membrane and allows the biomolecules to diffuse between the tissue and the culture medium.

In order to verify these design differences in our microfluidic device should not change the condition of the organotypic slice culture, we conducted a viability study in our microfluidic device using embryonic mouse brain slices. We were able to confirm high viability of the slices in our device with the total flow rate of 600 µL/hr (the flow rate was chosen based on the total reservoir volume of the device) after 48 hours in culture using vital staining dyes prior to starting toxicity studies (Fig. 5.8a-b). Furthermore, we tested the long-term viability of the brain slice in our device up to 7 days. Due to the limitation of the total volume in a 96-well plate (~ 30 mL), we decreased the flow rate to 150 µL/hr for this long-term slice culture testing to allow for the continuous flow in the device without the need of refilling the culture medium. As a result, the slice appeared to be very healthy with the stain of calcein-AM throughout the full slice (Fig. 5.8c) and only few EthD-1 stained cells found in the slice (Fig. 5.8d).

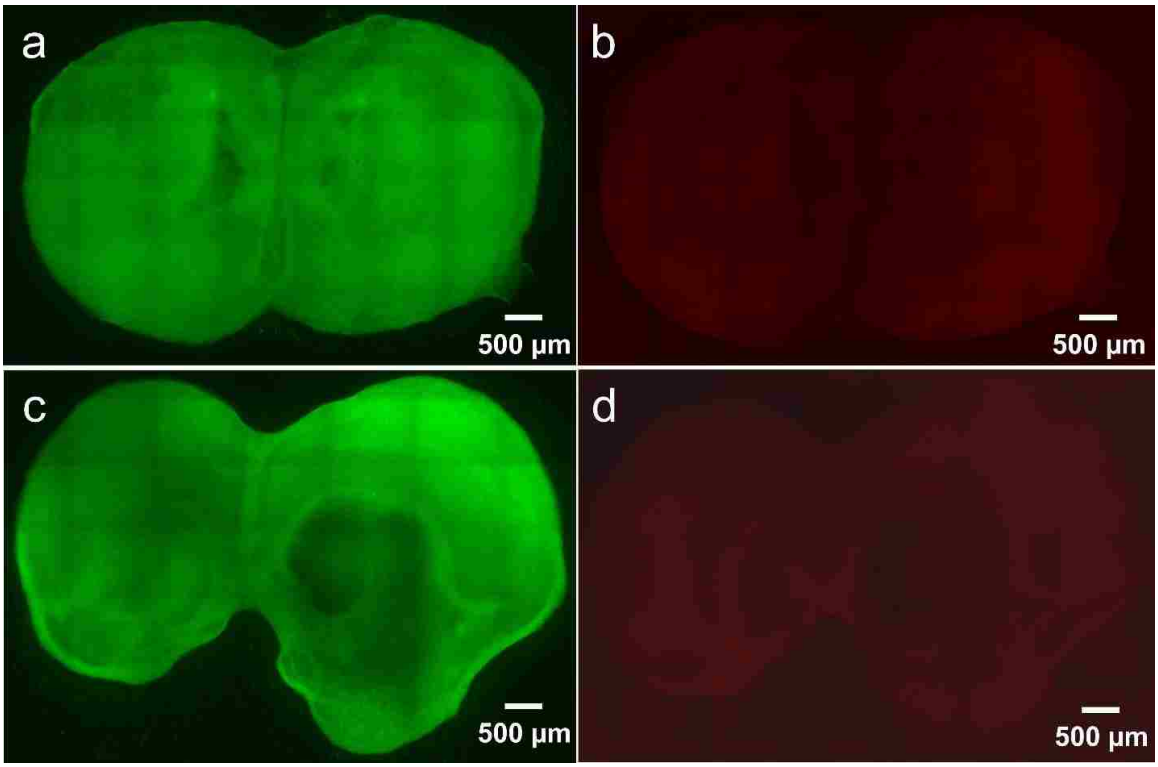

Figure 5.8. Organotypic mouse brain slice cultures in microfluidic devices.

E18 coronal mouse brain slices were cultured in our microfluidic device for 2 days (a-b) and 7 days (c-d), followed by staining with calcein AM (a,c) and EthD-1 (b,d), and imaging using epifluorescence microscopy. The grid patterns on both images are image stitching artifacts due to uneven illumination.

5.5.3 Fluid Transport in a PTFE Porous Membrane

To explain fluid transport in our microfluidic device, we consider the PTFE porous membrane separate from the tissue slice. In theory, the membrane's mesh structure creates high hydrodynamic resistance: therefore, the porosity of the membrane allows molecules to diffuse in the membrane without convection. We initially tested the fluid transport in a PTFE porous membrane placed in our microfluidic device using fluorescein (M.W. 332). As a result, we observed that lateral diffusion of reagents within the membrane can be adjusted by varying the flow velocity of the fluids in the microchannels underneath the membrane (Fig. 5.9). From this observation, we suspected that the membrane might support flow which is driven by the fluid streams in the microchannels.

In order to investigate this fluid transport phenomenon, we used fluorescently labeled dextran with different molecular weights (M.W. 3000 and 70,000) to determine if the fluid transport is dominated by convection or by diffusion. If the length of lateral diffusion in a PTFE membrane does not change between these two different molecular weights of dextran, then the fluid transport is dominated by convection. On the contrary, the dominant fluid transport is diffusion. We found that the spreading length of fluorescence signal is altered by different molecular weights (Fig. 5.10a-b). This difference in the spreading length of fluorescence signal between these two molecular weights is particularly obvious at the downstream regions. Furthermore, we performed an additional experiment using quantum dots (5~20 nm in diameter) to confirm the dominant fluid transport in our device (Fig. 5.10c). In consequence, no single quantum dot was observed outside of the channel region, indicating that diffusion plays a dominant role in PTFE porous membranes.

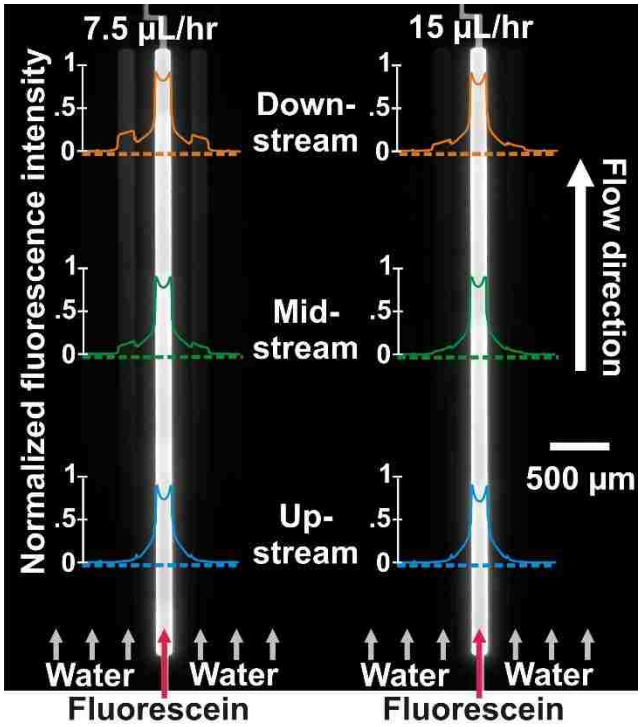

Figure 5.9. Transfer from the underlying fluid streams into the PTFE porous membrane.

The extent of lateral diffusion of fluorescein within the membrane (direction orthogonal to flow) decreases when the flow velocity underneath the membrane is increased.

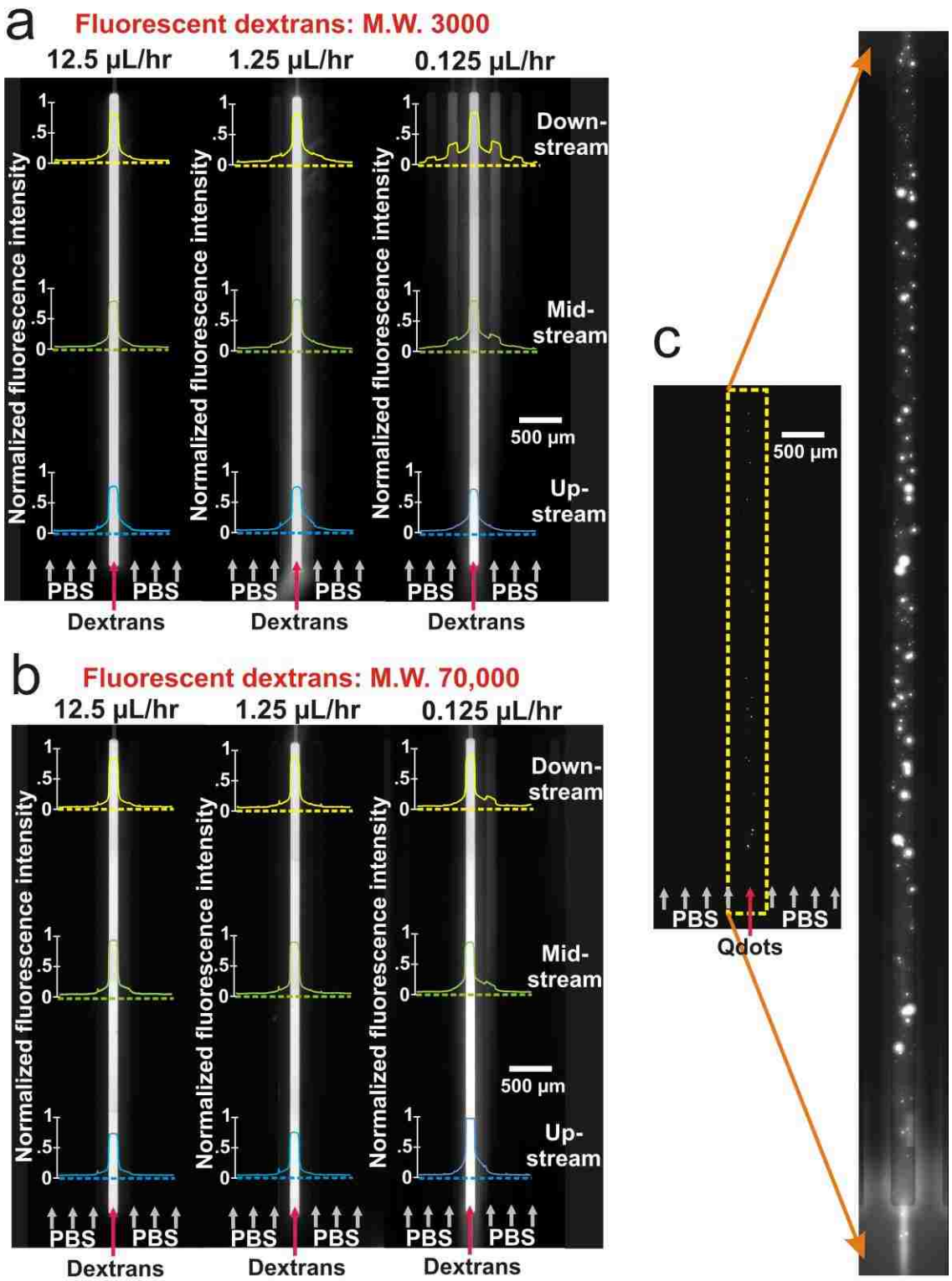

Figure 5.10. Molecular weight-dependent behavior reveals that fluid transport is dominated by diffusion in PTFE porous membranes.

(a,b) The extent of lateral diffusion (a: Dextran 3000, b: Dextran 70,000) within the membrane scales with the flow velocity underneath the membrane. (c) Quantum dots with 5~20 nm in diameter flow through a microchannel in our device.

5.5.4 Diffusion-Based Comsol Modeling Confirms the Concentration Profiles in Microfluidic Organotypic Tissue Slice Culture

To further understand how our microfluidic device can achieve selective drug delivery to a tissue slice, we built a simple diffusion-based model using Comsol. In our microfluidic device, the drug delivery channels (containing concentration C_1) are separated by buffer channels (concentration C_0). In the Comsol model, we assumed delivery and buffer channels in direct contact with a 200 μm thick 2D "tissue slice" (Fig. 5.11a) which is assumed to be a homogeneous porous medium [115]. Comsol simulations use configurations of delivery and buffer channels (vary in the numbers of intervals between each of two drug delivery channels) as shown in Figure 5.11a-c. The delivery channels act as concentration sources which isotropically diffuse into tissue slices. Buffer channels next to delivery channels act as concentration sinks that limit diffusion from delivery channels. Hence, the flows in both delivery and buffer channels create stable sources and sinks that result in the formation of steady-state chemical concentration patterns over time inside tissue slices. The concentration plots in Fig. 5.11 shows the predicted concentration profiles at 10 μm, 25 μm, 50 μm, and 100 μm above delivery channels with different numbers of buffer intervals in a tissue slice. This simple diffusional model assumes high flow resistance of the tissue slice and neglects the contribution of advection (mass transport due to fluid's bulk motion) potentially caused by injected flow at the bottom slice surface into the porous tissue. Thus our model provides a lower estimate of the observed spatial drug distribution profiles.

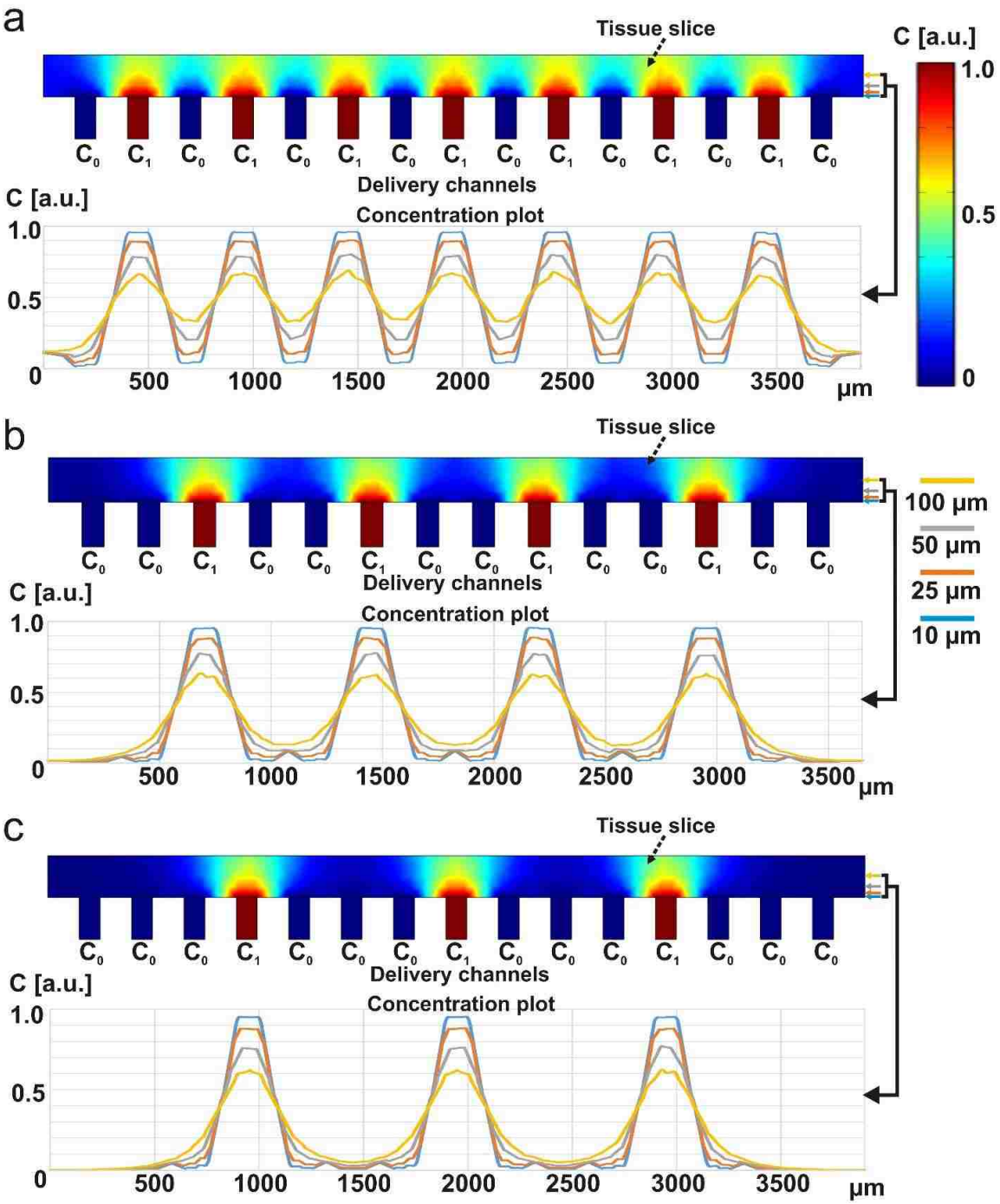

Figure 5.11. Purely diffusive model of the expected steady-state concentration profile corresponding to fluorescein.

(Fluorescein: MW = 332 and D = 5.7 x 10^{-10} m^2s^{-1}) Concentration plots below the 2D concentration profiles show the concentration 50 µm above the delivery channels (within the slice). Note how the buffer channels act as sinks that appear to counteract the effect of diffusion. (a) Sinks formed by a single microchannel. (b) Sinks formed by clusters of two microchannels. (c) Sinks formed by clusters of three microchannels. Any unevenness along each trace line is because of the coarse meshing in finite element modeling. The

blip in between channels in blue and orange traces is the concentration value in between each of two buffer channels.

According to Comsol modeling (Fig. 5.11), it appears that more than one buffer channel in between each of two delivery channels are needed to create a control region (the region with minimal concentration value diffused from the adjacent delivery channels).

5.5.6 Regioselective Intracellular Delivery of Biomolecules to a Mouse Brain Slice

As we demonstrated the steady-state concentration profiles above, in concept, it shows that our microfluidic device is able to deliver biomolecules selectively. In order to further verify the simulated concentration profiles, we delivered two different colors of cell nuclear staining reagents, Hoechst (blue) and Sytox Green (green) to a fixed mouse brain slice (Sytox Green can only enter into cells with compromised cell membranes) for 5 hrs through alternating streams using our microfluidic device with the total outlet flow rate of 1.2 mL/hr (15 µL/hr in each delivery channel). As a result, we observed that these staining reagents were selectively delivered to the regions of the tissue slice with minimum lateral diffusion between the delivery channels, as shown in Fig. 5.12.

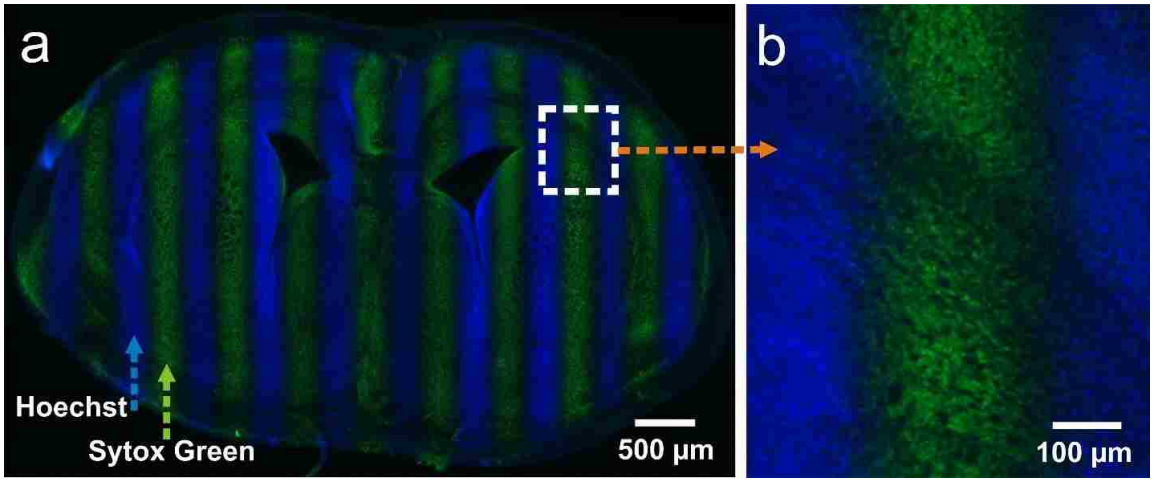

Figure 5.12. Selective delivery of biomolecules to a mouse brain slice.
Micrograph of a fixed mouse brain slice exposed to two different cell nuclear binding agents (Hoechst, blue, and Sytox Green, green) through the alternating streams in our microfluidic device for 5 hrs. The image is the result of stitching 42 fluorescence microscopy images.

Furthermore, we used calcein AM and fluorescently-labelled red dextran with the same flow rate setting to demonstrate the selective fluid transport in a live mouse brain slice. Calcein AM expresses green fluorescence after internalized within the cells. Therefore, the staining result should only show in the tissue slice. In contrast, red dextran is fluorescent by itself and leave the fluorescent stains on both the porous membrane and the tissue slice. We delivered both reagents in an alternating form beneath and across a sagittal-cut live mouse brain slice. As a result, tracks of the calcein AM stained cells in the tissue slice not only show the selective fluid transport, but the viability of the tissue slice (Fig. 5.13). On the other hand, red tracks from the porous membrane stained by dextran shows highly selective delivery and are corresponding to the dimension of the delivery channels (Fig. 5.13).

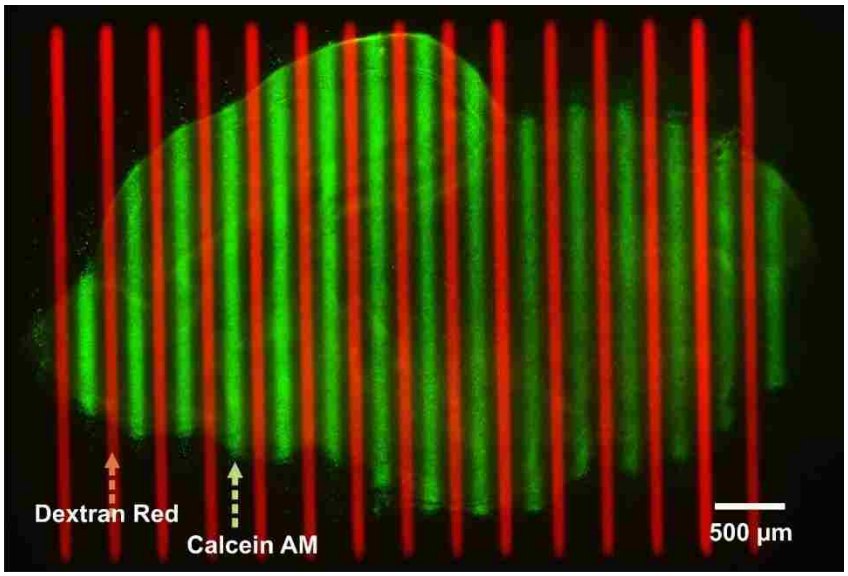

Figure 5.13. Selective delivery of biomolecules in a live mouse brain slice.
A live mouse brain slice was exposed to calcein AM and fluorescently-labelled dextran through the alternating streams in our microfluidic device for 1 hr.

5.5.5 Intracellular Staining Reveals the Transport Depth in the Tissue Slice

Diffusion-based Comsol modeling allows us to estimate the concentration profile across the thickness of the tissue slice. In order to observe the delivery of biomolecules into the tissue, we have conducted confocal studies of Hoechst dye penetration in a live mouse brain slice as shown in figure 5.14. Small molecule of Hoechst dye enters through the cell

membrane and binds to double-strain DNA, mimicking many cytotoxic drugs, such as kinase inhibitors which bind to interior sites of cells to induce cell death. In our penetration study, we selectively delivered 16 µM of Hoechst dye to a fixed mouse brain slice using our device for an hour. After 1 hour of delivery, 50 µm penetration depth of Hoechst staining was observed and measured using a confocal microscopy. Therefore, we conclude that at least 50 µm depth of cells were stained by Hoechst dye, indicating that our data acquisition should at least include 50 µm depth in the tissue slice.

Our intention in this experiment is to observe the penetration of biomolecules by using Hoechst dye. We should be aware that this observation is different than the concentration profile which we demonstrated above using Comsol modeling. One of the major reasons is that Hoechst dye staining requires DNA binding reaction in order to be seen. Therefore, the dye concentration is being consumed while is penetrating through the tissue slice.

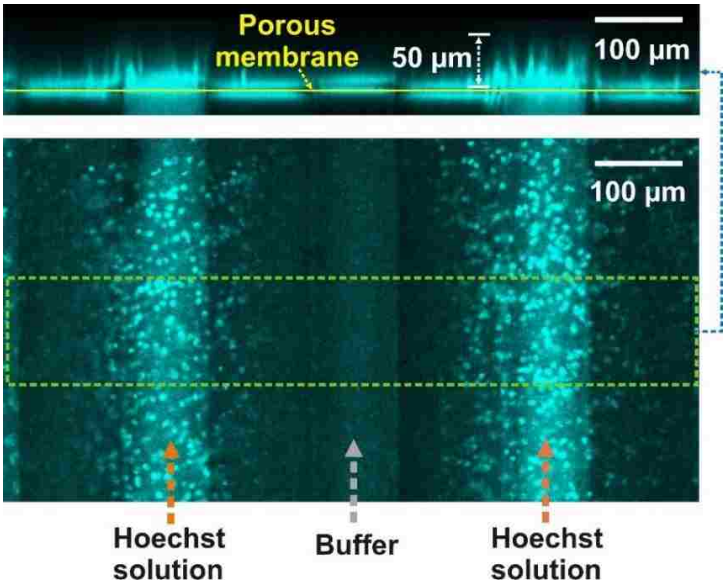

Figure 5.14. Estimated penetration of biomolecules in a live mouse brain slice.
A confocal image (top: penetration in the slice; bottom: one of the optical sections) demonstrates the penetration of Hoechst dye into a live mouse brain slice after 1 hr of delivery. The top image shows the presence of fluorescent cells up to ~50 µm into the slice, indicating that Hoechst dye penetrated at least 50 µm. Hoechst dye is not fluorescent unless it binds to cell nuclei. In this figure, there is clearly signals at the porous membrane interface. It is because Hoechst dye nonspecifically binds to the

surface of the porous membrane resulting in the fluorescent signals at the membrane interface.

5.5.7 Sequential/Combinatorial Delivery of Biomolecules in a Mouse Brain Slice

A recent report from Yaffe's group has discovered that delivering inhibitors that target oncogenic signaling pathways to a subset of triple-negative breast cancer cells prior to treating with chemotherapeutic agents such as doxorubicin increased the sensitivity of cancer cells to killing by genotoxic drugs [117]. This sequential treatment suggests a potential approach to activate oncogenic signaling pathways, rendering tumor cells more susceptible to chemotherapeutic drugs before chemotherapy. To accomplish the sequential drug delivery using our microfluidic device, we can first expose a tissue slice with a set of compounds (Fig. 5.15a-b), then the tissue can be rotated orthogonally before the second set of compounds was applied (Fig. 5.15c). As a result, intersects between the first and the second sets of compounds are the combinations (Fig. 5.15d) and this technique potentially allows for the delivery of n delivered drugs and n^2 combinations to the junctions.

In order to demonstrate the ability of our platform to perform sequential exposures in orthogonal format for a future sequential assay, we performed two consecutive deliveries of fluorescent tracers, EthD-1 (red) and Sytox Green (green), to a fixed mouse brain slice by rotating the culture membrane at 90 degrees in between the first and the second reagent delivery. Figure 5.16 shows the formation of the junctions after two reagents deliveries sequentially and orthogonally.

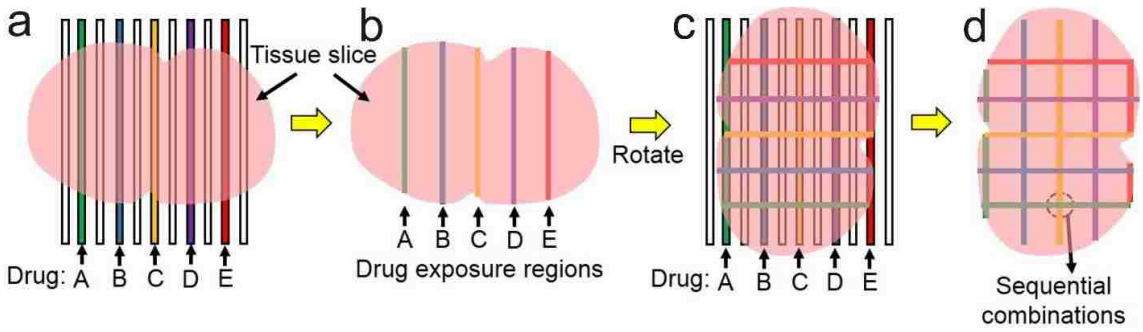

Figure 5.15. Schematic of sequential drug delivery for drug testing on an intact tissue.

After delivering the first set of drugs (a-b), the culture membrane can be rotated 90 degrees to deliver a second set of drugs (c-d). Hence, two sets of drugs can be delivered sequentially and orthogonally to a tissue slice.

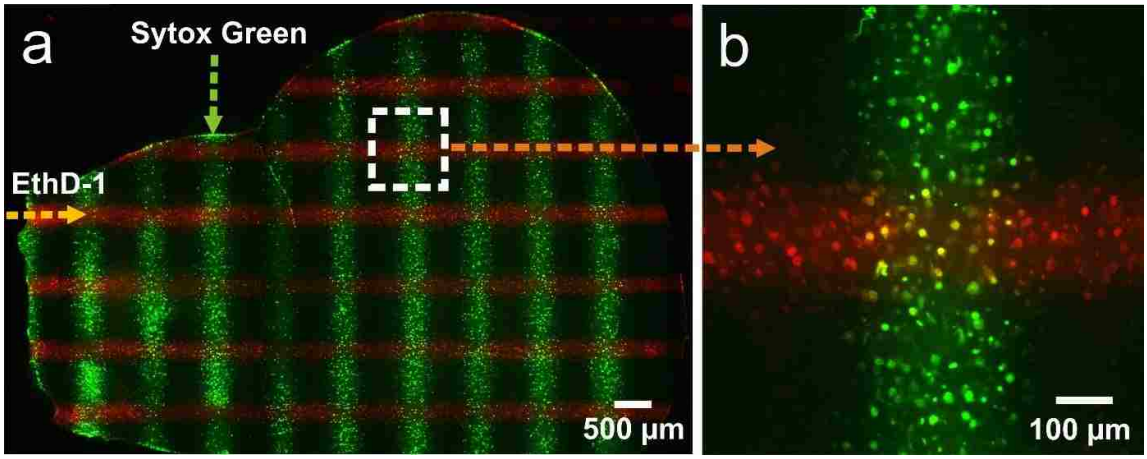

Figure 5.16. Demonstration of sequential drug exposure.

The culture membrane is rotated and repositioned (with tissue attached to the membrane) in the device between the first and the second reagent deliveries. As a result, *n* reagents delivered in parallel result in the formation of n^2 junctions where n^2 sequential pairs of reagents ("sequences") are delivered. For this sample, the image only contains half of a mouse brain slice because the width of a coronal-cut adult mouse brain slice is longer than the fluidic channels.

Our microfluidic platform has two key features that overcome current limitations of high-throughput cancer drug screening on intact tissues: 1) the coupling of organotypic slice culture with a microfluidic drug delivery device, which is used to perfuse the intact tissue slices through a removable PTFE membrane; and 2) the adaptation of this approach to a familiar multi-well plate format that enables multiplexed fluid routing and facilitates tissue handling and imaging for assessing tissue drug response patterns. These features make our device a desired platform for multiplexed drug screening on intact tissues.

5.5.8 Extended Applications Using the 96-Well Plate-Based Device

5.5.8.1 Membrane Interface Culture for Dissociated Cells

The original purpose to integrate a porous membrane in our device is to create an air-fluid interface for organotypic slice culture. This air-fluid interface allows the tissue

slices to be efficiently exposed to oxygen under normoxic condition. However, our device can also be used for dissociated cells for many biological studies, such as focal stimulation. To demonstrate this potential, we seeded monolayer of human fibroblasts on the porous membrane in our device and demonstrated the selective delivery of biomolecules using calcein-AM (Fig. 5.17). Calcein AM not only serves as a fluorescent tracer for visualizing the selective delivery of biomolecules to cells, but also verifies the viability of the cells cultured on the membrane. This demonstration shows the possibility of using our device for micro-scale cell stimulation and serving as a tool for understanding basic biology.

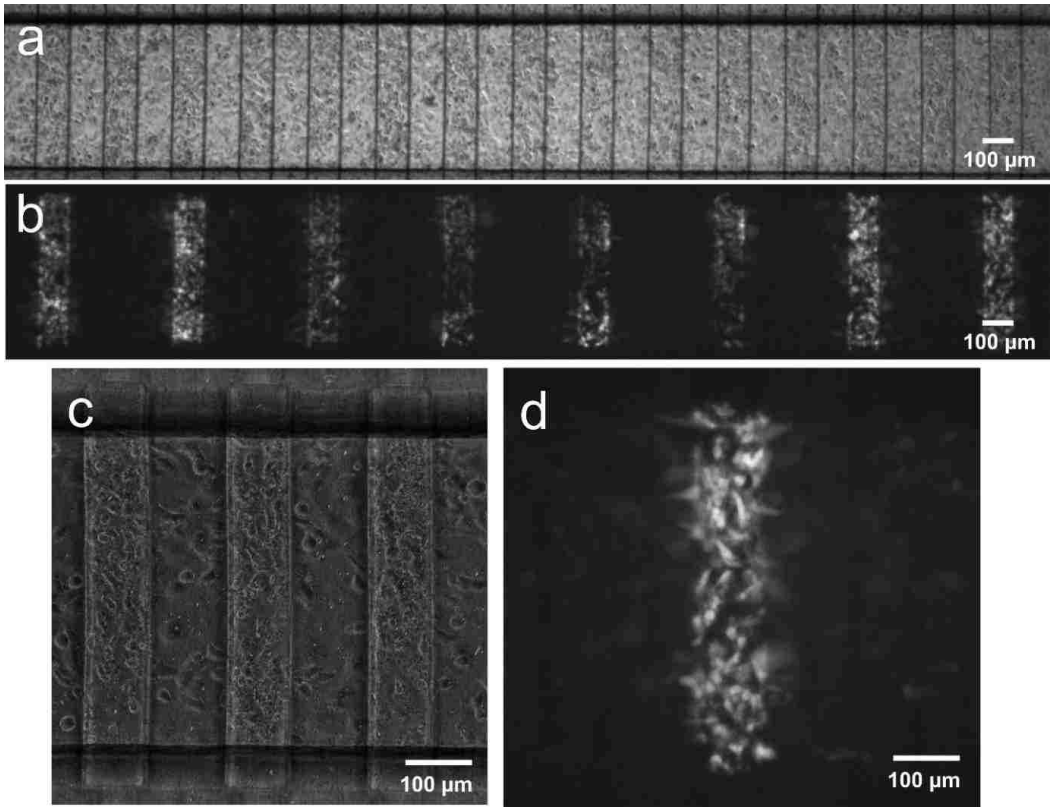

Figure 5.17. Dissociated cells culture in a 96-well plate-based microfluidic device.
(a) A phase-contrast image of human fibroblasts attached and spread on the PET porous membrane bonded on our device. (b) Selective calcein-AM delivery to the dissociated cells. (c-d) High magnification (20X objective) of phase-contrast (c) and fluorescence (d) images reveal highly selective staining results.

5.5.8.2 Generation of Chemical Gradients Using the 96-Well Plate-Based Device

One of the main cancer research fields is cancer metastasis, which involves chemotaxis of tumor cells and stromal cells in the surrounding microenvironment during cancer progression. For example, known ckemokine CXCL12 (stromal derived factor-1 (SDF-1)) binding primarily to CXC receptor 4 (CXCR4) to initiate signals related to chemotaxis has been found to associate with cancer metastasis [118]. Therefore, the ability to create biochemical gradients to induce chemotaxis in a physiologically relevant cancer model has a potential to not only discover more relationships between chemokines and its binding receptors, but also allow for testing the effect of the treatment on the metastatic cells.

Our microfluidic device can be easily converted into a biochemical gradient generator for inducing chemotaxis on an intact tissue slice. The device allows for organotypic slice culture which recapitulates the tumor physiological condition and the chemical gradient can be produced underneath of the porous membrane and delivered to the tissue slice. The exposure of biochemical gradients to an organotypic slice culture model can help to understand the invasive and migratory behaviors of cancer cells and has a potential to assist the inhibitory drug discovery in highly invasive types of cancer. Figure 5.18a shows the formation of the chemical gradient using red coloring dye in one of the two slice culture areas (one is the gradient chamber and the other is the control chamber). The gradient was generated by pipetting different concentrations of the coloring dye from high to low in the wells in respect to the channels delivering to the gradient chamber. Because the gradient is formed based on the concentrations in the individual delivery channels, the position of the gradient can be adjusted according to the position of the tissue slice at the region of interest (Fig. 5.18b-d).

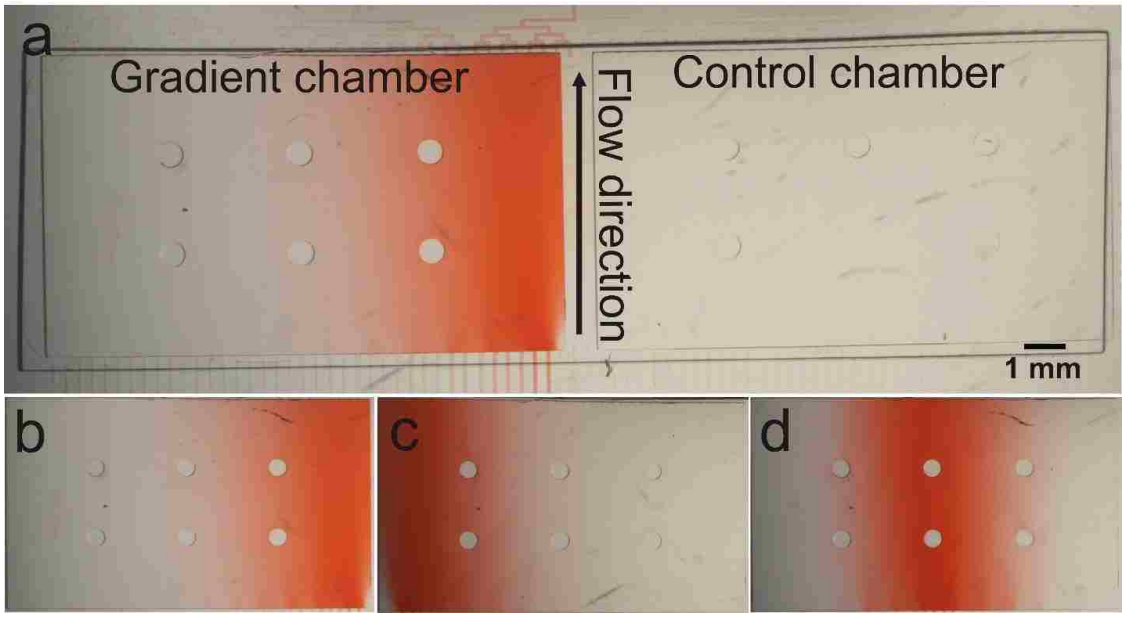

Figure 5.18. Chemical gradient generation from our 96-well plate-based device.

(a) The culture area of the device is divided into two chambers, a gradient chamber and a control chamber. Each chamber is linked to 40 individual channels for the formation of the chemical gradient. (b-d) The position of the gradient can be adjusted based on the initial concentrations of the individual wells/delivery channels.

Chapter 6: Multiplexed Chemosensitivity Testing on Organotypic Slice Cultures

6.1 Summary

In this chapter, we explain the complete methodology from device preparation, selective drug delivery, imaging acquisition, and readout analysis in detail. Here, we demonstrate the response of live mouse brain slices to a range of drug doses in parallel. Drug response is measured by imaging of markers for cell apoptosis and for cell death. Both epifluorescence and confocal microscopy were used for imaging acquisition.

6.2 Introduction

6.2.1 Motivation

The potential of using intact tissue slices for drug discovery and cancer diagnostics has been explored in the past decades [51, 119, 120]. Despite the organotypic culture technique allowing for simple tissue slice culture, the number of slices that can be produced is limited based on the size of the sample, resulting in slice culture being a low throughput system for drug testing. Unlike cell cultures, the models using intact tissues lack a standardized high-throughput drug delivery system. Therefore, we demonstrate a microfluidic device that permits regioselective drug delivery with spatiotemporal control in slice cultures to address this need. Our device allows to deliver large numbers of drugs to an intact tissue slice to increase the throughput of the organotypic slice culture model. Our device shows the potential to become a standard high-throughput platform for drug delivery on intact tissues.

6.2.2 Staurosporine Induces Cell Apoptosis

Staurosporine (STS) is a natural compound derived from bacterium [121]. One of the main biological activities from STS is to act as a nonselective protein kinase inhibitor by preventing ATP binding to the kinase, because STS has stronger affinity to the multiple ATP binding sites on the kinase [122]. This competitive kinase inhibitor has been found to induce neural apoptosis [123]. Many interests in the activities of STS have been focused on the potential for anti-cancer treatment [124]. In our brain slice culture model,

we used STS to mimic the application of chemotherapeutic drugs to intact tumor tissue slices by inducing apoptosis from the brain cells.

6.2.3 Vital Dye Staining Detects Cellular Caspase 3/7 Activity

Cell Event Caspase-3/7 Green Detection Reagent, which detects apoptotic cells. The reagent is a four amino acid peptide (DEVD) conjugated to a DNA-binding dye; the DEVD peptide sequence is a cleavage site for caspase-3/7 and the conjugated dye is non-fluorescent until cleaved from the peptide. Therefore, this dye is highly specific to the cells with apoptotic activities rather than based on the integrity of the cell membrane. As we previously introduced, Cell Event Caspase-3/7 is compatible with both live cell fluorescence-imaging and formaldehyde-based fixation methods. Therefore, after staining and prior to imaging, our tissue slice can be fixed using 4% PFA.

6.2.4 Dose-Dependent Response in Drug Screening Models

The dose-dependent response describes a relationship between different levels of chemical exposure and the biological effects from the cells [125]. This relationship is the fundamental concept in toxicology to understand the hazardous and the safe doses of the compounds [126]. This understanding allows us to make an assumption following the half maximal inhibitory concentration (IC50), the concentration of a drug required for 50% inhibition in vitro [127], to determine an adequate dosage for a specific compound. The ability to rapidly create a dose-dependent assay from a drug testing model not only demonstrates the sensitivity in response from the model, but also holds the potential to guide proper dosages to the patients.

6.2.5 Automated Cell Nuclei Counter

In our data collection, we plan to use cell nucleus staining so that the stained cells are easier to observe and quantify through confocal microscopy. However, because the tissue is composed of a high density of cells, the number of the cells can be extremely high and time-consuming to count. Currently, there are several systems available for automated nucleus counting for high-throughput data analysis. Many of these systems, however,

require expensive software and hardware attachments for image acquisition, analysis and storage. Based on this consideration, a cost-effective alternative for image analysis would be a welcome tool for our studies. Therefore, we propose to use ImageJ, a free Java-based public-domain image processing and analysis program developed by the National Institutes of Health (NIH) which is widely used in biological research [128]. With an automated nucleus counter plug-in [129], this becomes a powerful tool to assist our cell counting process. This software is capable of handling different types of nuclei images with the user-defined inputs of (1) an estimation of the diameter of a cell, (2) an estimation of the minimum distance between cells, and (3) either a region of interest (ROI) selected with ImageJ's selection tools or a black and white mask image that is white in regions that are to be counted. These user-defined area and intensity range parameters will minimized the error of computer cell counts. The captured images can then be opened in ImageJ for evaluating positive nuclei stains on fluorescence images [130, 131].

6.3 Materials and Methods

6.3.1 Device Preparation

The assembled microfluidic device was treated with oxygen plasma using the same conditions for bonding for sterilization and hydrophilization prior to use. Immediately after the plasma treatment, the device was transferred to a cell culture hood and microchannels were filled by pipetting culture medium into well reservoirs, covering the open channels with a PTFE membrane and then applying gentle suction to the outlet. Once microchannels were filled, the device was left in a cell culture incubator for 1 hr to allow culture medium to temperature and pH equilibrate prior to use.

6.3.2 Organotypic Mouse Brain Slice Culture

Embryonic or neo-natal mouse brain slices were prepared with the same protocol described in Chapter 4. The slices were cultured on PTFE membrane well insert with proper medium feeding below the membrane in a cell culture incubator for 2~3 days before the drug exposure experiment. The culture medium was replaced full volume once

every two days during culture and the cultured slices were monitored daily to estimate the condition of the slices before the drug exposure.

6.3.3 Device Operation

Tissue slices were transferred from the culture membrane well insert by first cutting PTFE membrane and placing it onto the open microchannels of the device. The full culture area of the device (80 parallel open channels) was imaged to register the position of tissue slices relative to delivery channels (Fig. 6.1). Well reservoirs were then filled with either drug or buffer with the desired spacing (~2-4 buffer channels in between each of two delivery channels). Drug channels contained culture medium mixed with staurosporine (STS; #S6942, Sigma-Aldrich, St. Louis, MO) to induce cell killing in mouse brain slices and buffer channels contained culture medium alone. Flow was initiated by connecting the device outlet to a 20 ml syringe (#302830, BD Bioscience, San Jose, CA) and syringe pump (Fusion 200, Chemyx Inc., Stafford, TX) to ensure a total negative flow rate of 600~1200 µL per hour (7.5~15 µL per hour in each delivery channels). The device was left in a cell culture incubator before and during the drug exposure process.

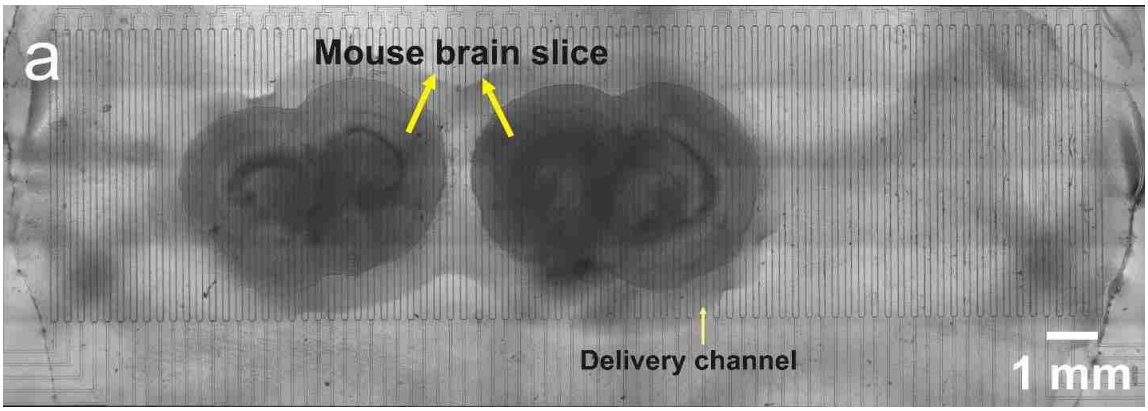

Figure 6.1: Pre-drug exposure image allows us to visualize the position of the tissue slices in correspondence to the delivery channels.
The brain slice on the right covers 22 delivery channels and the other on the left covers 20 delivery channels.

Once the drug exposure process was finished, the culture membrane with the tissue slices was transferred to another dish chamber. The device was rinsed by replacing the full

volume of well reservoirs with PBS 10 times for the drug wells and 3 times for the buffer wells. The microchannels were flushed with PBS by covering the open channels with a new PTFE membrane and operating the device at 200 µL/hr negative flow rate overnight to ensure sufficient rinsing. Once the rinse was finished, all the wells in the device were filled with PBS and left in the incubator before the next use.

6.3.4 Fixable Dyes to Access Cell Apoptosis and Cell Death

CellEvent™ (#C10423, Invitrogen, Carlsbad, CA) and Fixable Viability Dye eFluor 660 (eBioscience, San Diego, CA) were used to detect cell apoptosis and cell death respectively. DAPI (#D3571, Invitrogen, Carlsbad, CA) was used to label cell nuclei. After drug exposure, mouse brain slices were removed from the device and submerged in 1 µM CellEvent™ and 1 µM Fixable Viability Dye eFluor 660 mixing solution in PBS at room temperature for 1 hr, followed by fixation in 4% PFA at 4℃ overnight. Tissue slices were then permeabilized with 0.1 % Triton X-100 (#T8787, Sigma-Aldrich, St. Louis, MO) for 30 min following by 100nM DAPI staining overnight. Clearing agent was then applied by immersion in ScaleView A2[101] (Olympus, Center Valley, PA) for at least 2 d prior to imaging. Before the tissue clearing agent was applied, tissue slices were rinsed 3 times with PBS (5 min/cycle) in each of two staining, fixing and permeabilizing processes.

6.3.5 Imaging Acquisition

Tissue slices were imaged in a glass-coverslip bottom chamber (#12565336, Fisher Scientific, Pittsburgh, PA) using a Nikon Eclipse Ti inverted microscope (Nikon Instruments, Melville, NY) with epifluorescence illumination. An automated x-y stage and both 4X and 10X objectives were used to acquire fluorescent images. Images with 10% overlap were subsequently stitched together to generate fluorescence images. Individual images were focused manually during stitching. All the images were acquired with a 12-bit cooled CCD camera (ORCA-ER, Hamamatsu, Japan). Nikon NIS-Elements AR software was used to control image acquisition.

Confocal images were obtained using a Zeiss LSM 510 confocal microscope (Carl Zeiss, Thornwood, NY) with a 20X objective. Drug-treated and control regions were located visually using the binoculars of the microscope. The thickness of optical sections was 2.2 μm, based on the longest excitation wavelength of the fluorescent channel. All three fluorescent channels were set to the same optical thickness. The z-scan function was used to define the surface (0 μm) of the tissue slice, then confocal image acquisition started 10 μm above the bottom tissue surface (which was in contact with the PTFE membrane sealing microchannels). Five optical slices (~ 2.2 μm thick/optical section) separated by 10 μm and 50 μm deep in tissue slices were acquired from both STS-treated and buffer control regions. The maximum optical depth of 50 μm was selected to ensure high overall fluorescence intensity. Confocal images were then acquired sequentially in tissue slices at the regions of interest.

6.3.6 Background Correction for Large Image Stitching

Imaging a full tissue slice requires images to be stitched from a large array of individual images. Epifluorescence microscopy with an automated x-y stage with supported software can easily obtain a large stitched image. However, uneven illumination from individual images causes significant artifacts after image stitch. In order to fix the unevenness of the illumination, we have to adjust each images prior to stitching. In epifluorescence images, each individually captured image is the result of the sample's fluorescence (F) multiplied by the intensity of the illumination (I) plus the background signal registered by the camera (F_b).

To correct for the uneven intensity of illumination and find the true sample fluorescence across the image, we need to capture both illumination (I) and background (F_b) images as references to reveal the source images (F). A simple equation below explains the method to reconstruct the original image.

$$F = (\text{Resulting image} - F_b) / I$$

To demonstrate this image correction method, we acquired a 3 by 3 stitched image (9 individual images) from a region of a mouse brain slice sample. Illumination and

background images as references were acquired for correcting individual images prior to stitching (illumination image was acquired from a standard fluorescence reference slide). After image correction, the resulting image with a significant improvement is shown in figure 6.2.

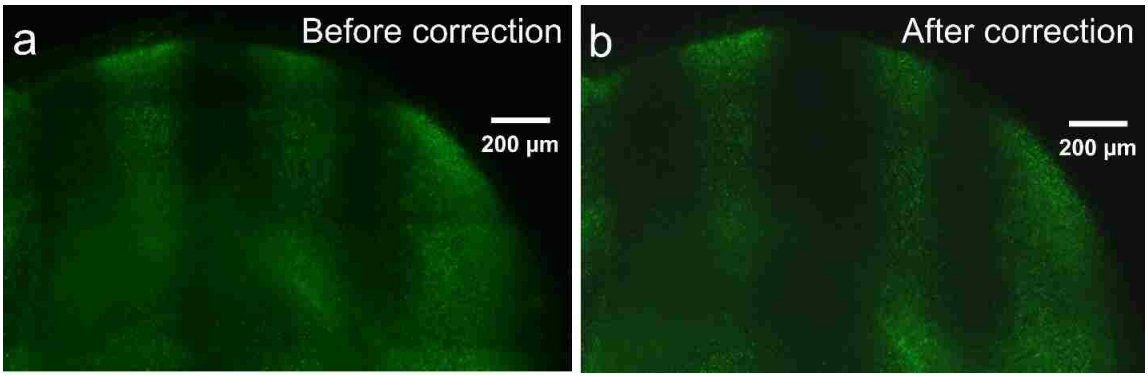

Figure 6.2: Image background correction.
Image stitch (3X3) before (a) and after (b) correction. The grid-like artifact is significantly decreased from (a) to (b).

6.3.7 ImageJ for Data Analysis

ImageJ was used to convert epifluorescence images into two-dimensional fluorescence intensity plots for brain regions of interest. In our experiment, the dorsal cortex area of mouse brain slices in epifluorescence images was manually selected. The fluorescence intensities (y-coordinate) at a particular distance along the slice (x-coordinate) is obtained by averaging the pixel intensities from the selected dorsal cortex region, and normalizing with respect to the maximum average intensity measured. The measurement of the normalized fluorescence intensities from plots could then be used directly to gauge drug and dose-dependent responses in tissue slices from the region(s) of interest.

ImageJ with an automatic nuclei counter plug-in was used to convert confocal images into cell counts. We used inputs of 14 pixels for the diameter of a cell and 7 pixels for the minimum distance between cells to analyze all the confocal images. An additional parameter, threshold, was set at 1 for DAPI and apoptotic cells, and at 2 for dead cells to improve counting accuracy. Captured images were opened in ImageJ to quantify and report positive cell staining in fluorescence images as cell counts that were exported to an

Excel spread sheet for further analysis. The combination of cell counts (DAPI, apoptotic cells, and dead cells) was quantified by calculating percentages of cell apoptosis and cell death from each image captured in spreadsheet data. Figure 6.3 demonstrates the automated cell counting from confocal images.

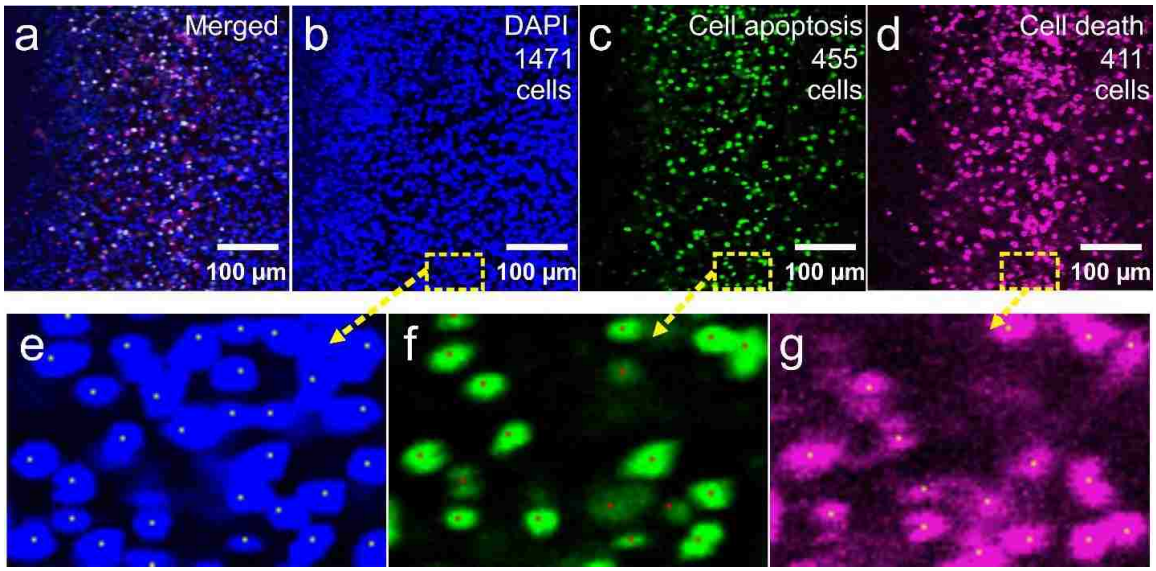

Figure 6.3: Automated cell count.
(a) 3 channel merged confocal image. (b) DAPI confocal image. (c) Cell apoptosis confocal image. (d) Cell death confocal image. (e-g) Selected regions with automated counting. Yellow dots (Fig. e,g) and red dots (Fig. f) in the middle of each cells show cell recognition.

6.3.8 Student t-test

Student t-test allows us to determine whether our result is significantly different between two populations. Based on our drug testing results between the drug-treated and –untreated regions, we assume that the distributions of these two populations are normal, and that the variances of these two distributions are the same. Therefore, we chose two-sample t-tests assuming equal variance as the method to compare two populations to determine if two sets of data are significantly different from each other, to compare the drug exposed and control regions for quantitative analysis.

6.4 Troubleshooting

Before device operation, it is important to visually inspect all the visible microchannels under a stereo microscope to avoid any significant clogging, especially for the reused device. Clogged microchannels in the device will cause an unbalanced flow rate and change the fluid transport patterns to the tissue slices. If the reused device needs to be left in an incubator for a long period of time (>3 days) before the next experiment, the PBS or culture medium solution in the device should be replaced with sterile water to avoid channel clogging from salt crystallization formed from PBS or chunks of serum particles accumulated from culture medium. However, sufficient rinsing with PBS and culture medium is required to ensure proper pH and osmolarity balance prior to the drug testing experiment.

The device hydrophilization step is critical and allows for the change in the PDMS surfaces from hydrophobic to hydrophilic. Thus, all the PDMS microchannels in the device can be easily filled with PBS and culture medium by gentle suction from the outlet. Once the channels are filled, the device should be left in a cell culture incubator with high humidity to avoid evaporation.

After the drug testing experiment, we transferred the culture membrane with the tissue slice to a glass coverslip bottom chamber and the tissue slice was separated from the membrane for imaging. However, the tissue slice may sometimes may strongly attach to the membrane resulting in difficulty in separation. This can be solved by fixing the tissue with 4% PFA prior to detaching the tissue slice from the membrane. Note that the process of separating the tissue slice from the porous membrane should be completed carefully, by gently pushing flow from an edge of the tissue slice using a transfer pipet. It is also important to remember the bottom side of the tissue slice, in contact with the membrane, for imaging.

DAPI and Hoechst staining allow us to visualize the full population of cell nuclei throughout an intact tissue slice. DAPI is cell-impermeable and requires tissue permeabilization to allow the DAPI molecules to penetrate through the cell membranes.

Hoechst is cell-permeable with low cytotoxicity and is often used as a vital dye staining reagent. Therefore, Hoechst can be combined with other vital dyes to stain the tissue at once. However, an uneven staining was observed in our selective drug testing experiment (Fig. 6.4a) when the Hoechst was applied before tissue fixation and permeabilization. We believe that this uneven staining result was because of a difference in the rate of molecule penetration through the cell membranes. At the regions of the tissue slice which have been exposed to STS, cell membranes were compromised either because the cells were undergoing cell death or the dimethyl sulfoxide (DMSO) used to dissolve STS damaged the cell membranes allowing for the Hoechst molecules to rapidly go through the cell membranes. From this unexpected Hoechst staining result, we recommend to fix and permeabilize the tissue slice before staining with DAPI and Hoechst. Figure 6.4b demonstrates a mouse brain slice uniformly stained with DAPI after the tissue slice has been fixed and permeabilized.

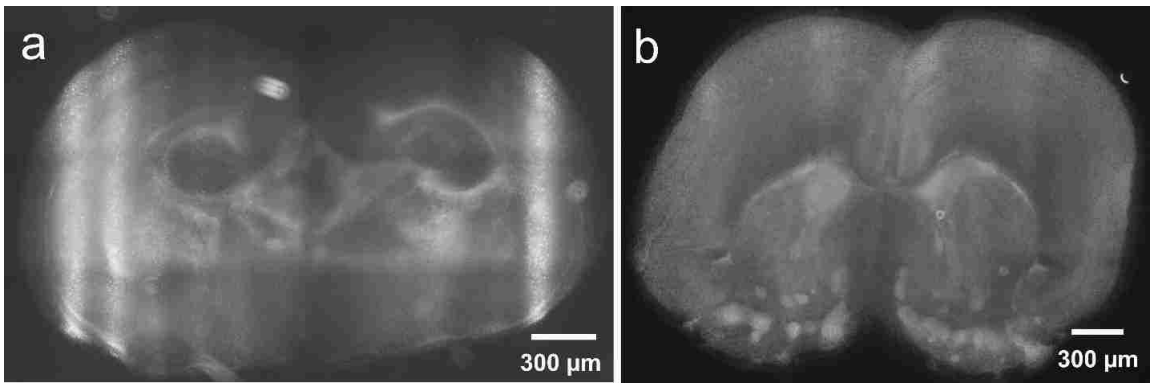

Figure 6.4: Hoechst staining of tissue slices.
(a) The live mouse brain slice was stained with Hoechst right after the selective drug testing. The uneven staining at the drug exposure regions and buffer regions are shown on the image. The difference in fluorescence intensity at the drug exposure regions is associated with the concentrations of the drug. (b) The Hoechst was applied after tissue fixation and permeabilization, allowing the tissue slice to be evenly stained with uniform fluorescence intensity throughout the whole slice.

When a large stitched image has an artifact due to an uneven illumination from each tile of image, calibration (aperture, flatness of the stage) of the microscope can sometimes improve the evenness of the illumination and decrease the artifact after image stitching. If the artifact still remains, imaging correction is necessary as we described above in the

materials and methods section. For imaging correction, testing the reference images (illumination and background images as described above) on a small stitched image from the sample is recommended to ensure the proper references for corrections before expanding to the full size.

The automatic nuclei counter plug-in in ImageJ is a great tool for automated cell counting from our confocal images, as the stained cell nuclei can be easily identified. For different types of tissues and cells, the size of cell nuclear and the separation between cells can vary. Therefore, it is necessary to adjust the parameters according to the readouts. Even for the same type of tissue, different parameter settings might be required because the variations in cytostructures among the anatomical regions of the tissue. To optimize the parameters, the automated cell counting results should be visually confirmed in order to improve the accuracy of the outcomes.

6.5 Results and Discussion

6.5.1 Induction of Cell Death on an Intact Mouse Brain Slice Using STS

In order to test the effectiveness of STS on mouse brain slices, we performed an initial study based on organotypic slice culture using PTFE membrane well inserts. 1 µM STS was used to induce cell death in a brain slice for 24 hours and EthD-1 was used as the readout to detect dead cells in the slices. Figure 6.5 shows the viability of two mouse brain slices where Fig. 6.5a is the control and Fig. 6.5b is the STS treated slice. As a result, the control slice (Fig. 6.5a) only shows the fluorescence background from the tissue slice with few cells stained with EthD-1 (EthD-1 stained cells show red and bright dots which can be differentiated from the tissue background on fluorescent images). In contrast, the STS-treated slice (Fig. 6.5b) contains a massive amount of cells stained with EthD-1 indicating the low viability of the slice. Ideally, confocal images can be acquired and used to quantify the viability of tissue slices.

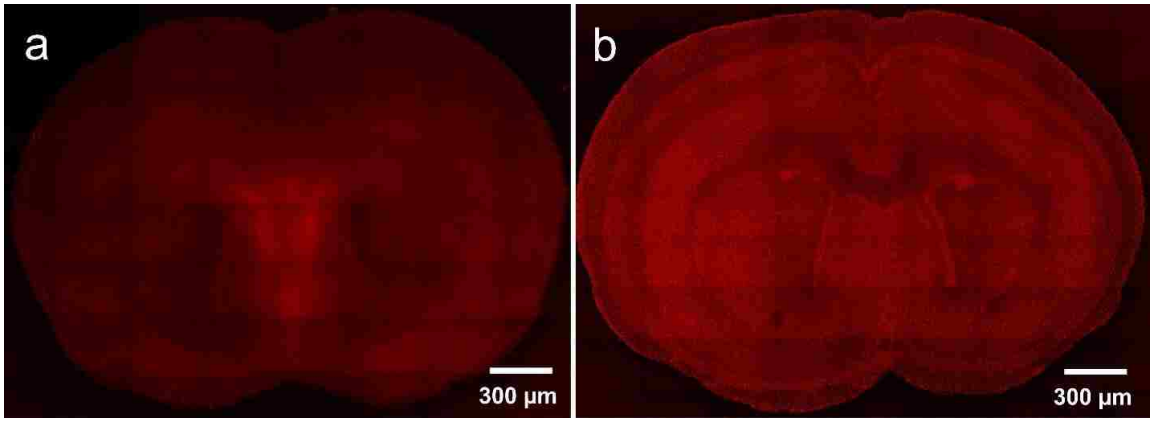

Figure 6.5: Prior testing of slice culture conditions with and without STS exposure
(a) The brain slice culture under normal medium condition retain highly viability with only minor spots stained by EthD-1. (b) The brain slice exposed with STS for 24 hours appeared to be unhealthy with massive amount of cells stained by EthD-1.

6.5.2 Regioselective Drug Testing on an Intact Mouse Brain Slice

In our drug testing experiment, we hypothesized that the regions of cells in an intact tissue at the selective drug delivery areas can be differentiated from the buffer areas using vital dye staining reagents. In order to test this hypothesis, we selectively delivered 1µM STS to intact mouse brain slices for 24 hours and visualized the slices under an epifluorescence microscopy after staining reagents were applied. As a result, the cells labelled with staining reagents appeared stained at the drug exposure regions (Fig. 6.6). In contrast, the buffer regions remained clean with an average fluorescence intensity 7-fold less than the drug exposure regions. As the staining reagents only label the cells with Caspase 3/7 activities or with compromised cell membranes, this result demonstrates the feasibility of our assay to differentiate the regions of cell apoptosis (Fig. 6.6a) and cell death (Fig. 6.6b) on an intact tissue slice.

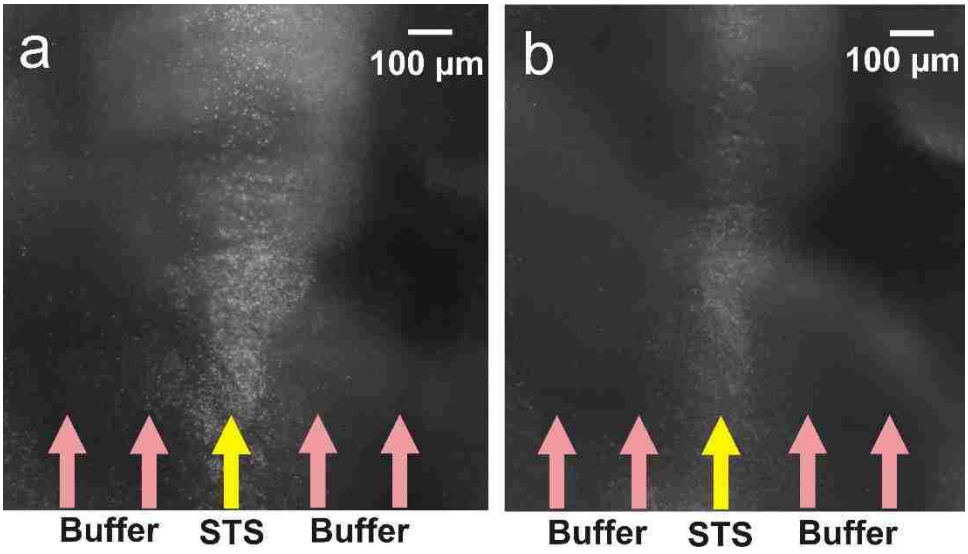

Figure 6.6: A cropped region from an intact tissue slice after selective drug delivery and tissue staining.

A track of apoptotic and dead cells formed at the STS-exposed region was detected by both (a) CellEvent™ and (b) Fixable dead cell stain reagents.

Furthermore, we tested the minimum exposure duration of 1µM STS which will still cause the induction of cell apoptosis from mouse brain slices. The staining reagent, CellEvent™, only labels the cells with Caspase 3/7 activity. Thus it is highly specific to detect cell apoptosis which is largely induced by STS in our experiment. After testing different durations (3, 5, 6, 8, 9, 10, 11, 13 hrs) of the STS exposure, we found out that the STS-induced caspase 3/7 activity requires at least 7~8 hours prior to being detected. Figure 6.7 shows the difference in cell apoptosis labelled by CellEvent™ after the selective STS exposure at the duration of 6 hours (Fig. 6.7a) and 8 hours (Fig. 6.7b). Figure 6.7a only shows minor cell apoptotic activity at the drug exposure area, in contrast, the figure 6.7b shows a visible track of apoptotic cells at the drug exposure area. This result indicates that the minimal duration of 7~8 hours for 1µM STS exposure to a mouse brain slice is required to be detected by CellEvent™ for our readouts.

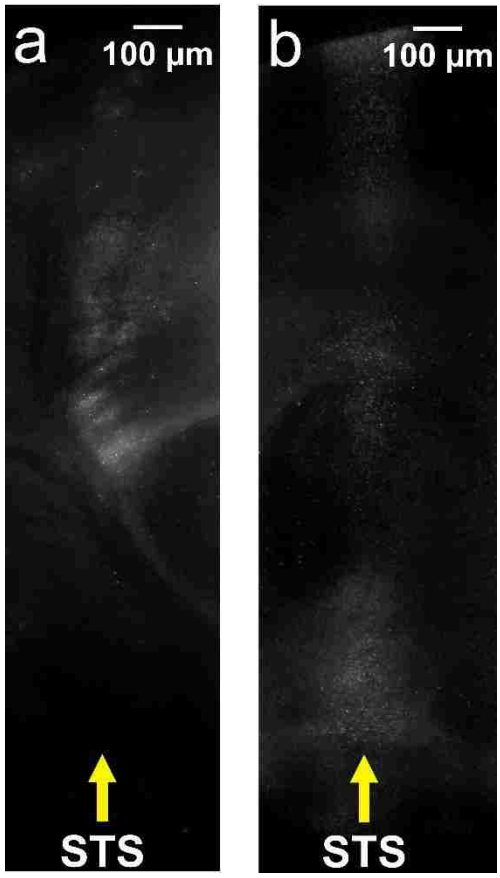

Figure 6.7: Formation of apoptotic cells stained with CellEvent™ at different durations of drug exposure.

(a) Six hours of selective STS exposure. Apoptotic cells started forming at the drug exposure region with partially bright spots along the drug exposure area. (b) Eight hours of selective STS exposure. Apoptotic cells formed a visible track along drug exposure area.

6.5.3 Chemosensitivity Testing on Intact Mouse Brain Slices

In order to test the ability of our microfluidic platform to produce dose-dependent chemosensitivity profiles of an intact tissue, mouse brain slices were used by exposing a slice to different doses of STS. After STS drug delivery, the tissue slices were stained with CellEvent™ to distinguish apoptotic cells. The brain slices were fixed using 4% PFA and an epifluorescence microscope with an automated stage was used to capture the image of whole brain slices.

We first delivered the same dose of STS in culture medium containing 1 µM of STS for 18 hrs, with an interval of four buffer channels in between each of two STS delivery

channels to an intact mouse brain slice. We observed significant apoptosis (cells labeled with CellEvent™) at the STS-treated regions (Fig. 6.8a) in 18 hrs of STS delivery. In order to quantify the fluorescence intensity from the epifluorescence image, we selected the dorsal cortex region from the image of the mouse brain slice (yellow-dashed region in Fig. 6.8a). The dorsal region has a relatively even cell density, which allowed us to establish a fluorescence intensity readout of cell apoptosis across STS-treated regions more easily than in other regions with more variable cell density or tissue porosity. Similar fluorescence intensity profiles across four STS-treated dorsal brain regions was observed as shown in Fig. 6.8b (the standard error of mean, averaged over the 100 µm wide drug delivery channels, was 7.1% and mostly attributable to the rightmost data peak). This result not only shows the feasibility of quantifying readouts based on epifluorescence images, but also demonstrates the reproducibility of outcomes from different drug-treated regions with the same dose of drug exposure.

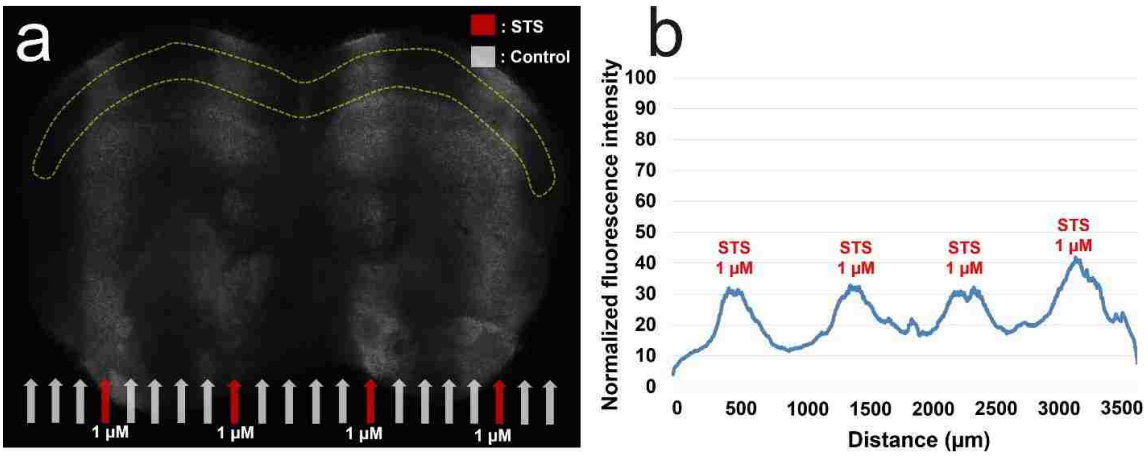

Figure 6.8: Same dose of STS on an intact mouse brain slice.
STS was used as a model cytotoxic agent. (a) Equivalent doses (1 µM for 18 hrs) of STS were delivered to coronal-cut mouse brain slices with the same interval distance (four buffer channels) in between each of two STS solutions. Fluorescent lanes indicate apoptotic cell staining by CellEvent™ in STS-exposed regions. (b) 2D fluorescence intensity profile across dorsal cortex of the mouse brain slice (yellow dashed region in panel a). The plot shows peaks of fluorescence intensity across STS-exposure areas.

Next, different doses of STS drug solution (culture medium containing 6 µM, 4 µM, 2 µM, 1 µM, 500 nM, 100 nM, 10 nM of STS) were delivered to an intact mouse brain

slice with a separation of two buffer channels in between every two STS delivery channels. The slice was exposed to the STS solution at the selected regions for approximately 8 hrs to allow induction of apoptosis. The resulting images show that apoptotic cells stained by CellEvent™ (bright cell nuclei) form lines over channels used to deliver STS, and that fluorescence intensity from labelled cells increased with the dose of STS (Fig. 6.9a). Our results demonstrate that the intensity profile measured from the dorsal cortex area increases in a STS dose-dependent manner (Fig. 6.9b).

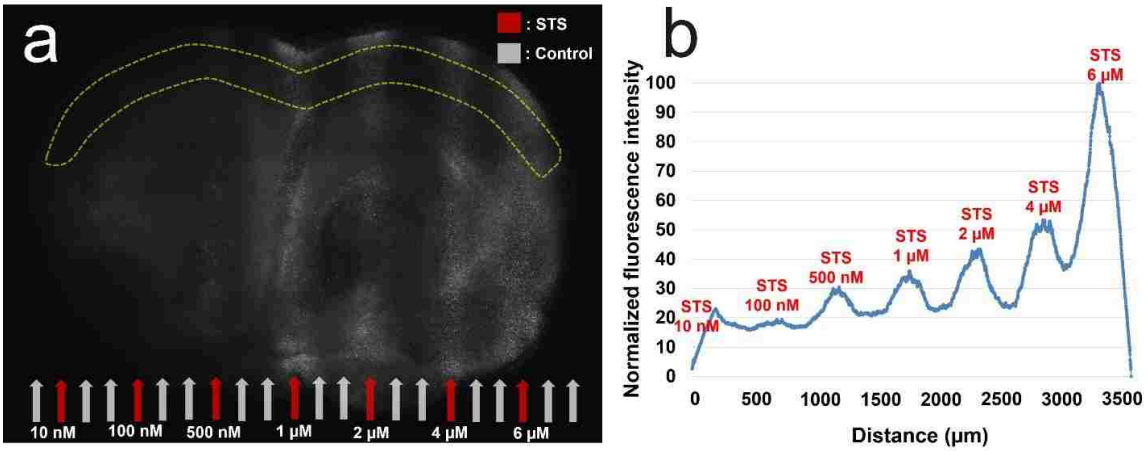

Figure 6.9: Dose-dependent cytotoxicity in an intact mouse brain slice.
(a) Different doses of STS solution were delivered to a coronal-cut mouse brain slice with the same interval distance (two buffer channels) in between each of two STS solutions. Fluorescent lanes of apoptotic cells stained by CellEvent™, formed at the STS-exposed regions in which the density of apoptotic cells is positively correlated with the STS dose. (b) 2D fluorescence intensity profile across dorsal cortex of the mouse brain slice (yellow dashed region in panel (a). The plot shows that the peaks of the fluorescence intensity located at the STS exposure areas correspond with the doses of STS in a dose-dependent manner. The fluorescence intensity plot can be directly used as a drug screening readout on intact tissues.

Figure 6.10 shows the concentration profiles using a diffusion-only Comsol model that simulates the delivery of STS as in Fig. 6.8 (1 µM for 18 hrs) and Fig. 6.9 (6 µM, 4 µM, 2 µM, 1 µM, 500 nM, 100 nM, 10 nM for 8 hrs). The fluorescence intensity plot (Fig. 6.9b) from our experimental study and the simulated concentration plot (Fig. 6.10b) obtained from Comsol modeling show a strong correlation (R^2 = 0.933), indicating that the fluorescence intensity readouts generated using the apoptotic marker (averaged over

the 100 µm wide drug delivery channels) are significantly correlated with STS concentration.

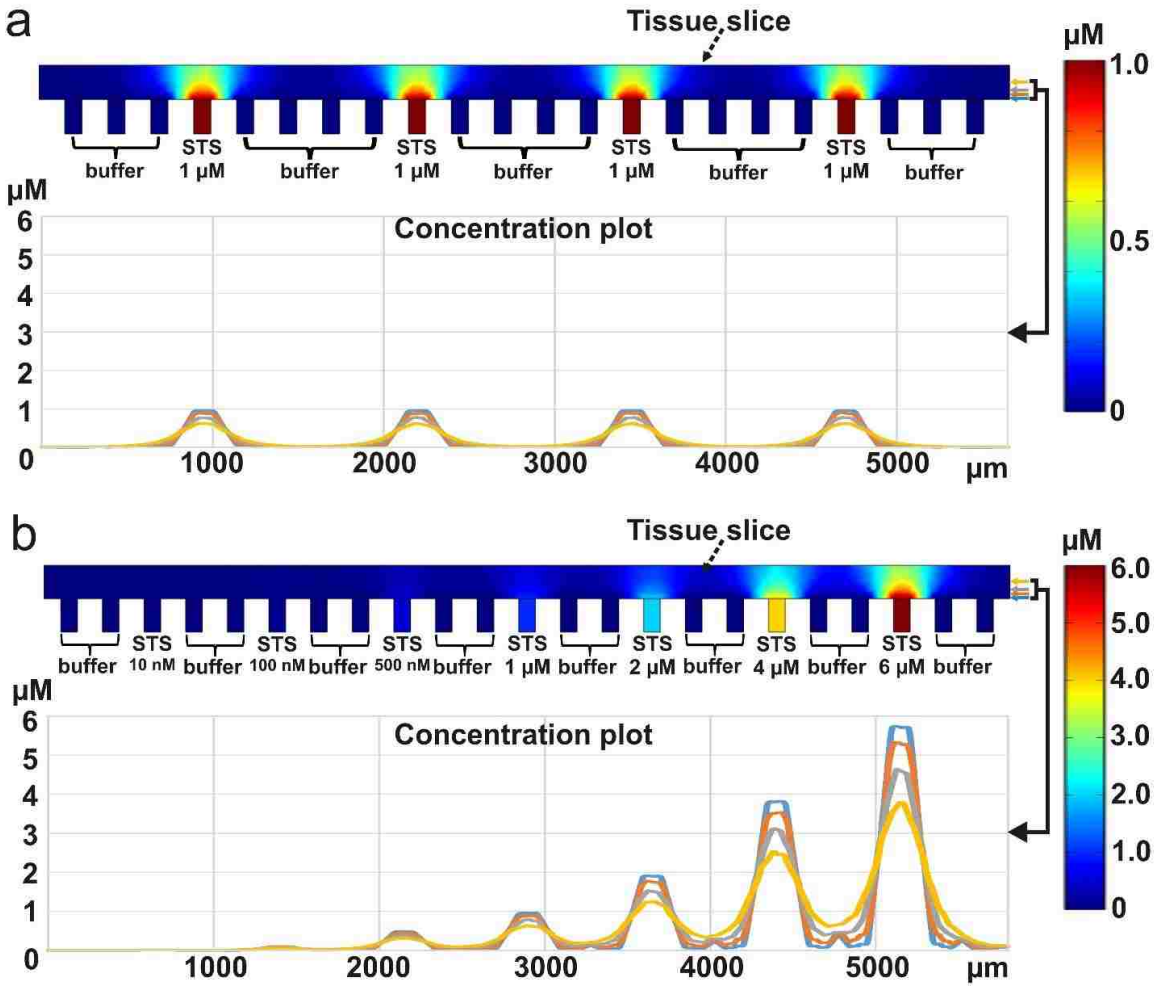

Figure 6.10: Purely diffusive model of the expected STS concentration profile corresponding to the experiments of Fig. 3.

(a) Concentration profile produced by four equal 1 µM/18 hr doses delivered through intervals of four buffer channels in between one STS delivery channel. (b) Concentration profile of different doses with intervals of two buffer channels in between one STS delivery channel. The concentration plots in (a) and (b) show the concentration experienced by the cells at 10 µm, 25 µm, 50 µm, and 100 µm above the delivery channels.

Even though we were able to quantify the tissue staining results directly from the images, but background signals from tissue slices remain unresolved. To address the background issue, we can take a fluorescence image of a tissue slice right before tissue staining as a reference image. Then the final image can substrate the reference image to eliminate the tissue background.

6.5.4 Optical Sections by Confocal for Data Quantification

Epifluorescence images (as shown in Fig. 6.11 and in Fig. 6.12a) allow for fluorescence intensity, but may not directly reflect the number of labeled cells due to variations in drug/stain penetration, optical focus, light absorption or labeling efficiency. Confocal or multi-photon microscopy can address these issues by using thin optical sections to visualize individual cells labeled with intracellular reagents. The numbers of individually labeled cells can then be counted using automated cell counting software (e.g. Image J) to provide a more accurate estimate of the number and proportion of dead cells over a perfusion channel.

In order to demonstrate the ability of confocal imaging to collect quantitative cell function data from intact perfused tissue slices, we compared STS-treated (culture medium with 1 µM STS) and buffer regions (culture medium alone) to detect cell nuclei by DAPI staining together with apoptotic and dead cells (Fig. 6.12b-c; epifluorescence images in Fig. 6.11). The cell counts of apoptotic cells and dead cells from each confocal image are expressed as percentages with respect to total cells. Each bar represents the average percentage of 5 confocal images (depth in the tissue: 0 µm, 10 µm, 20 µm, 30 µm, 40 µm) at that specific region (Fig. 6.12d-e). Our results show that the percentages of cell apoptosis and cell death were on average 7.4-fold and 6.8-fold higher, respectively, at the STS-treated regions than at the buffer regions (Fig. 6.12d-e). These results are statistically significant with the p-value < 0.001 using student t-test (two–sample assuming equal variances), and provide more detailed information than is contained in epifluorescence images (Fig. 6.12a). We directly compare the average percentages of the apoptotic cells (Fig. 6.12f) and dead cells (Fig. 6.12g) between the STS-treated and buffer regions at specific focal planes where tissue delivery of STS was equivalent. This approach – quantifying apoptosis and cell death from cell counts – allows results to be plotted as cellular percentages and thus should be less dependent on cell density than measurements obtained from epifluorescence imaging. These cell-based metrics should be especially useful for gauging drug response profiles in heterogeneous primary tumor specimens. This imaging approach can be extended by using tissue pre-

and post-labeling reagents to gauge the response to any drug, small molecule or treatment.

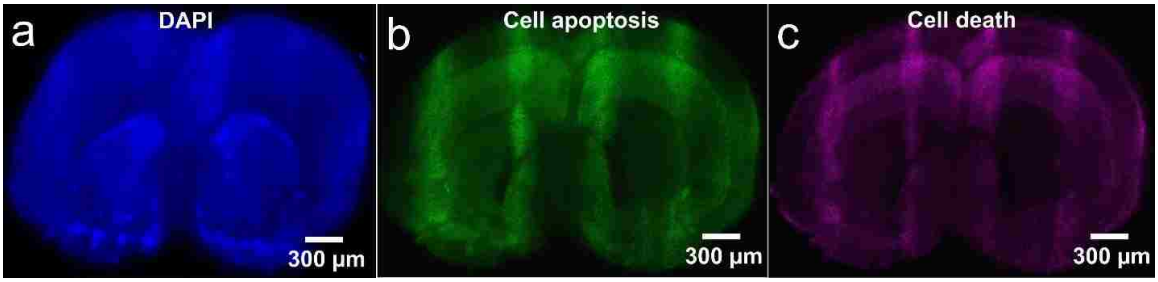

Figure 6.11: Combination of tissue staining.

(a) The brain slice was uniformly stained with DAPI which allows for recognizing the full cell population in the slice. (b) CellEvent™ staining revealed the apoptotic cells at the drug exposure regions. (c) Fixable dead cell staining revealed the dead cells at the drug exposure regions.

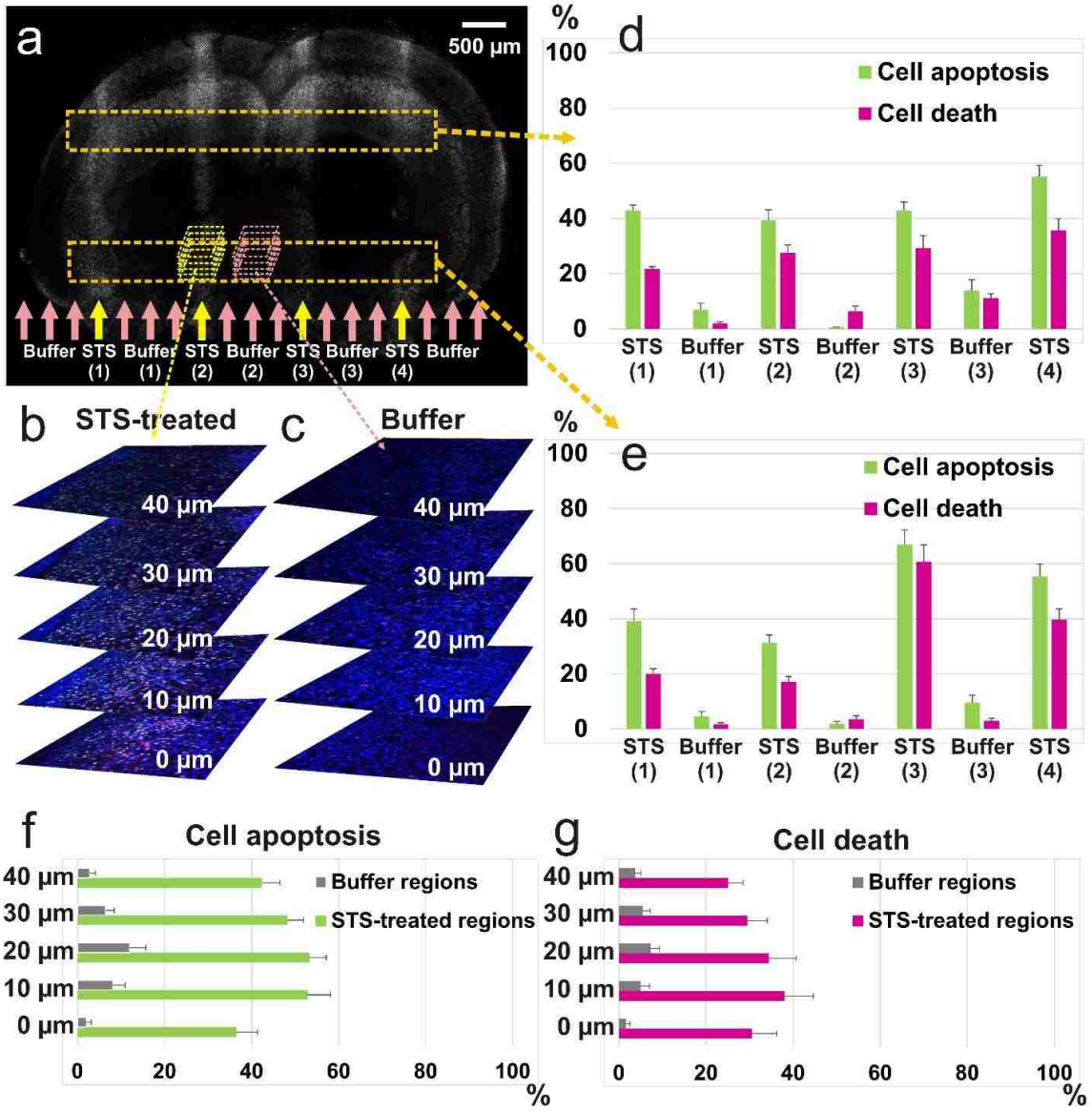

Figure 6.12: Dose-dependent cell killing in intact tissue slice cultures quantified by confocal microscopy.

(a) Epifluorescence image (dead-cell staining) of a P1 mouse brain slice after it is selectively treated with STS at four separate regions through four delivery channels (yellow arrows) for 24 hours, followed by apoptotic and dead cell staining. Four lanes of fluorescently labelled dead cells in the brain slice are visible in the STS-exposed areas. (b,c) Optical slices of STS-treated (b) and buffer (c) regions. Five optical slices are acquired at both regions of the tissue slice. Three fluorescence channels from a confocal microscope are used to detect cell nuclei (blue), cell apoptosis (green), and cell death (magenta). (d,e) Percentages of cell apoptosis and cell death across the slice (orange dashed boxes in Fig. 4a). Each error bar shows the standard error of mean. (f,g) Percentages of cell apoptosis (f) and cell death (g) at individual focal planes. Each error bar shows the standard error of mean.

Using confocal microscopy we were able to quantitatively compare the percentage of apoptosis (P_A) and cell death (P_D) at the STS-treated with those at the buffer regions (Fig. 6.12). P_A and P_D were consistently higher at the STS-treated regions than at the buffer regions. Since there is a wide interval between two drug channels, the intervening buffer regions provide within-sample and assay control regions to assess, e.g., background cell death from region to region across a tissue or biopsy slice. Heterogeneity in cell death within a sample or specimen can be assessed and controlled for by comparing treated and control regions in different areas of a tissue slice. We obtained the confocal images from two separate areas (top and bottom column boxes in Fig. 6.12) from the tissue slice to reduce the bias from our analysis and to include the importance of variability within a tissue sample. Our analysis revealed similarities between these two areas (top and bottom graphs). This multi-region analysis might potentially be useful to address tumor heterogeneity.

Both epifluorescence and confocal microscopy can be used to quantify cellular responses to drug compounds. Epifluorescence microscopy with an automated stage can rapidly acquire images of a full tissue slice from the culture surface. However, the fluorescence signal from fluorescently-labeled cells may be variable when derived from brain or tissue regions that are variable in structure or cell density. Confocal microscopy, in contrast, allows optical sectioning of tissue slices to provide high spatial resolution, though is substantially slower than simple epifluroescence imaging. Thus a hybrid imaging strategy with a customized imaging platform might provide the best combination of speed and accuracy to assess cellular response patterns in response to treatments.

Chapter 7: Regioselective Drug Delivery on Intact Mouse Xenograft Slices

7.1 Summary

In this chapter, we extended our study by testing our approach on xenograft models. We demonstrated the generation of the GBM mouse xenografts and the production of the xenograft tumor slices. We used our microfluidic device to selectively deliver a highly relevant chemotherapy drug to the xenograft tumor slices and determined the duration of the drug exposure required to obtain an adequate result. Finally, we explored the possibility of using a prostate xenograft model for extracting and culturing tumor biopsies.

7.2 Introduction

7.2.1 Motivation

Malignant gliomas constitute about 80% of the primary malignant tumors in the central nervous system and are essentially incurable [132]. Patients diagnosed with GBM, which comprise over two-thirds of all adult malignant primary brain tumors, have a median survival of about one year and overall 5-year survival rate of <5 %. Despite advances in surgical technique, delivery of chemotherapy and radiation [132] and myriad clinical trials, the dismal outcomes for GBM patients have not improved significantly in the last four decades. The advent of high-throughput genomic profiling and drug screening techniques heralds a new era of targeted cancer therapy, in which the identification of patient-specific cancer biology and drug response profiles can be used to inform therapy. However, significant challenges remain in developing more robust and practical pre-clinical drug screening techniques.

7.2.2 Glioblastoma

The American Brain Tumor Association estimates that more than 70,000 people will be diagnosed with a primary brain tumor in the United States in 2014. GBM is the most common and lethal malignant primary brain tumor and generally develops from the lineage of star-shaped glial cells called astrocytes which support nerve cells. These

tumors are normally found in the cerebral hemispheres but can also be found in other parts of the brain, brainstem, and spinal cord. This type of tumor is classified as grade IV (the most severe case) and the current standard-of-care is to apply radiation and chemotherapy with TMZ either alone or combined, despite poor prognosis (median survival rates of only 15 months). Growing evidence has shown a wide range of intratumor heterogeneity and suggests that treatment design needs to be patient-specific [133].

7.2.3 Current Drug Screening Models for GBM

The most commonly proposed screening methods for GBM utilize isolated tumor cell cultures However, cultured tumor cells disrupt interactions with the tumor microenvironment and may not retain phenotypic heterogeneity of tumor cells in situ, both critical factors in treatment response and resistance [134, 135]. The current trend of treatment to overcome the heterogeneity of GBM is based on the patient-specific xenograft model (PDX). This model recapitulates the physiological properties and maintains genomic characteristics of parental GBM tumor *in situ*. Furthermore, the treatment responses can be highly mimicked based on the same treatment options with similar dosages (irradiation or chemotherapy). As the knowledge accumulates, PDX models retain phenotypic heterogeneity and tumor microenvironment features. Therefore, this model is a potential tool for predicting drug responses in GBM patients. However, the process of generating this model is expensive, cumbersome and time-consuming, normally taking weeks to months to allow for tumor formation (the duration and success rate of tumor formation is dependent on the individual tumor cells). The PDX model is still a strong research tool with potential to assist in developing other drug screening methods.

7.2.4 Temozolomide

Temozolomide (TMZ) is an alkylating agent and is the current standard-of-care treatment for GBM patients. The biological function of TMZ is the ability to methylate DNA and trigger the death of tumor cells [136]. Despite a recent study has shown that the median survival benefit for GBM patients was only 4 months [137] and marginal improvement in

survival rate has been shown in other studies [138], TMZ in conjunction with radiation treatment is still the most widely recommended therapy for GBM patients.

7.3 Materials and Methods

7.3.1 Generation of Human GBM Mouse Xenograft

The human glioblastoma cell line GBM8 was used in the current study [139]. The cells were characterized for invasive and migratory behaviors both *in vitro* and *in vivo* and then confirmed for positive response to TMZ [139]. GBM8 cells were labeled by lentiviral GFP expression to allow for the identification of the cells prior to xenograft generation. Xenografts were generated by injecting 200,000 viable glioma cells (trypan blue, a dead cell-selective dye, was used to determine the viability of cells) orthotopically into immunodeficient nude mice [140] as described, grown *in vivo* for ~4 weeks to allow tumor formation.

7.3.2 Tissue Handling, Slicing, and Culture

In our experiment, the xenograft mouse brain was dissected and obtained in Dr. Rostomily's lab (UW south lake union). Once the xenograft mouse brain was resected, the brain was rinse with ice-cold DMEM for 2 times to wash off the blood. The whole brain was then stored in a 50 mL tube placed on ice with 5 mL of medium in the tube to barely cover the whole brain tissue. The lid of the 50 mL tube was loose to allow for oxygen (air) supply during the travel. We then transported the tissue back to our lab by a UW shuttle. Once the tissue arrived, we immediately started the tissue slicing process. The travel time should be minimized to increase the general viability of the tissue. The preparation and generation of the GBM xenograft slices followed the same protocol as mouse brain slices, except they were 400 µm thick. GBM xenograft slice cultures were performed in culture medium used for normal mouse brain slices and supplemented with epidermal growth factor (EGF; 20 ng/mL; #PHG0311 Invitrogen, Carlsbad, CA) and fibroblast growth factor (FGF; 20ng/mL; #PHG0264 Invitrogen, Carlsbad, CA). Xenograft slices were transferred to PTFE membrane well inserts for culture. The culture

medium was replaced in full volume once every two days throughout the slice culture period.

7.3.5 Device Preparation and Operation

The assembled microfluidic device was treated with oxygen plasma using the same conditions for bonding for sterilization and hydrophilization prior to use. Immediately after the plasma treatment, the device was transferred to a cell culture hood and microchannels were filled by pipetting culture medium into well reservoirs, covering the open channels with a PTFE membrane and then applying suction to the outlet. Once microchannels were filled, the device was left in a cell culture incubator for 1 hr to allow culture medium to temperature and pH equilibrate prior to use.

Tissue slices were transferred from the culture membrane well insert by first cutting PTFE membrane and placing it onto the open microchannels of the device. The full culture area of the device (80 parallel open channels) was imaged to register the position of tissue slices relative to delivery channels. Well reservoirs were then filled with either drug or buffer with the desired spacing (~2-4 buffer channels in between each of two delivery channels). Drug channels contained 1 mM TMZ (#T2577, Sigma-Aldrich, St. Louis, MO) to induce cell killing in human GBM mouse xenograft slices. Flow was initiated by connecting the device outlet to a 20 ml syringe (#302830, BD Bioscience, San Jose, CA) and syringe pump (Fusion 200, Chemyx Inc., Stafford, TX) to ensure a flow rate of 300~600 µL per hour.

7.4 Troubleshooting

For slicing xenograft mouse brains, it was difficult to produce consistent 300-µm slices. It is mainly because the tumor within the brain is softer and causes tissue jamming during slicing. Therefore, we set 400 µm as our target thickness for the GBM xenograft slices. However, it is possible to produce consistent 300-µm or thinner slices if we adapted the agarose embedding techniques.

In order to register the position of the tissue slices to the delivery channels, we imaged the full culture area of the device (80 parallel channels) prior to the experiment. However, this method takes an extra imaging step and requires a visual estimation of the drug exposure regions from a phase-contrast image. Furthermore, because the slices are thicker, the visibility of the delivery channels and the slice decreases as the thicker slice blocks the transmission of the light, resulting in dark phase-contrast images. To address this issue, we used an alternative approach by adding a small amount of Hoechst dye into the drug solution prior to filling into the wells. Hoechst 33342 nuclear staining dye acts as a tracer and has been proven for live cell culture with low cytotoxicity. Moreover, Hoechst dye has low molecular weight which is similar to most of the small-molecule kinase inhibitors or cytotoxicity drugs. As our system is highly based on diffusion, this similarity in molecular weight can potentially predict the drug diffusion in the tissue slice. This low concentration of Hoechst dye expresses fluorescence after binding to cell nuclei and gives a higher estimate of the drug exposure regions Fig. 7.1 shows an example of using a low concentration of Hoechst dye as a tracer in a GBM xenograft slice. The delivery duration was about 18 hrs and four drug delivery regions were observed on the slice as blue fluorescent lanes (Fig. 7.1). One drawback to using this alternative is the loss of one fluorescent channel. Therefore, the use of this alternative approach depends on the further imaging analysis.

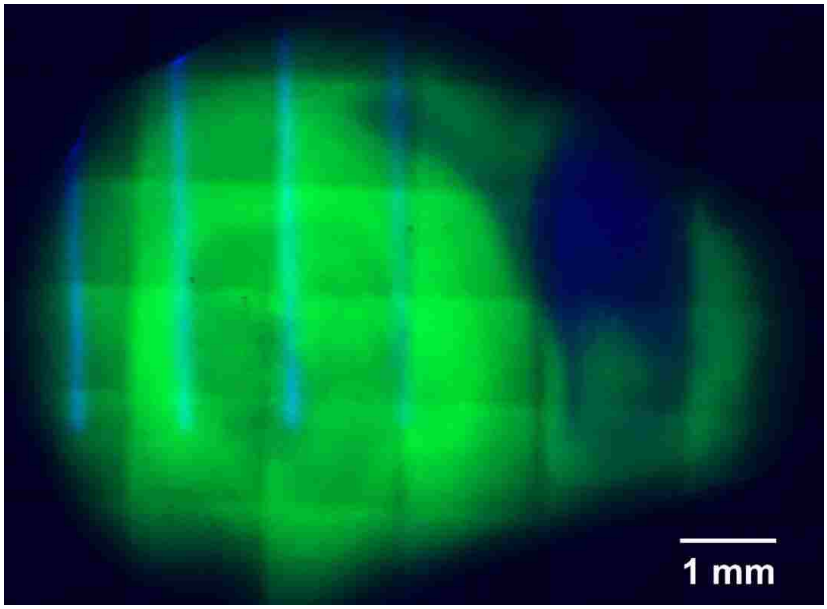

Figure 7.1: The use of Hoechst dye as a tracer to visualize the drug exposure regions on a GBM xenograft slice.

The green shows the GFP-labeled glioma cells spread throughout the full mouse brain slice. The faint blue tracks show the tracer delivered from the bottom delivery channels to the tissue.

The xenograft mouse brain slices produced from an adult mouse brain were significantly larger than the ones produced from the embryonic and neo-natal mouse brains. Therefore, the shortest dimension of the slice can still be longer than the length of the delivery channels in our device. To address this issue, we can either extend the length of the delivery channels by redesigning our microfluidic chip or shape the whole adult mouse brain to reduce in size before slicing. As the viability of the tissue slice is the only element that matters to our experiment, retaining the anatomical regions of the brain to preserve certain neural functions are not needed.

TMZ in aqueous solution can be unstable, and thus it is useful to determine whether a TMZ solution is active on cells known to respond to TMZ before using an aliquot for experimentation.

7.5 Results and Discussion

7.5.1 Tumor Formation and Distribution in GBM Xenograft Slices

The tumor cells were injected only in one hemisphere of the brain. After 4 weeks of tumor growth *in-vivo*, the xenograft mouse brain was harvested and the tumor was easily identified as shown in figure 7.2a (the right hemisphere of the brain is larger than the left). The rough center of the tumor has a small scooped hole which was caused by an injection needle from the initial tumor injection procedure. As the tumor cells were labeled with GFP, the tumor cells could easily be tracked within the brain tissue under an epifluorescence microscope once the slices were produced. Figure 7.2b shows a xenograft brain slice with GFP-labeled glioma cells growing and spreading within a mouse brain slice. The glioma cells grew on one half of the brain slice close to the injection site and infiltrated through the brain tissue. A small amount of tumor cells migrated from one side to the other through the cortex. The cause of this migration is unknown, which can either be the effect of chemotaxis or a simple artifact (cells move along anatomic planes within the brain gray or white matter.) because of the structure of the cortex.

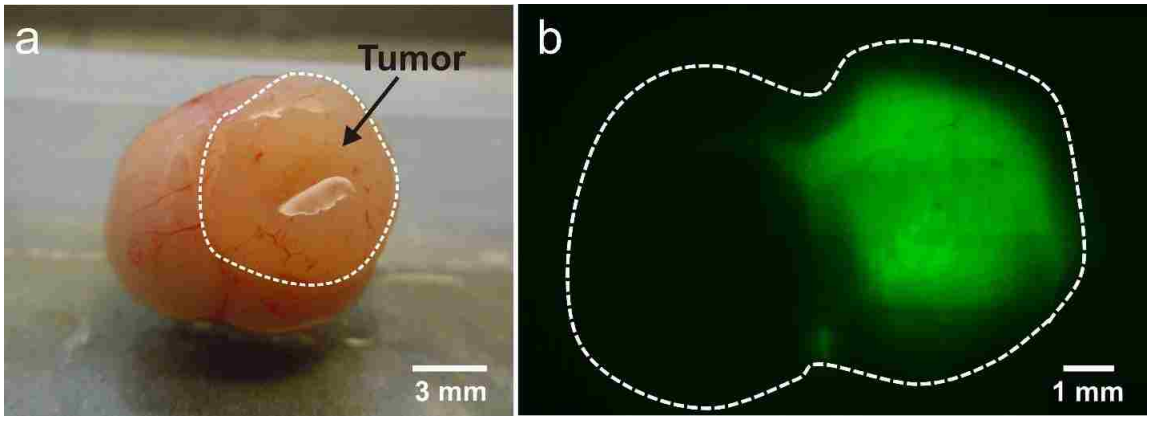

Figure 7.2: GBM xenograft mouse brain.
(a) A GBM xenograft mouse brain with a tumor on one hemisphere of the brain. (b) The GBM xenograft slice with GFP-labeled glioma cells for the identification of the tumor cell location.

7.5.2 Effect of Time on TMZ Response

From our TMZ drug testing experiment on a GBM xenograft slice, the readout is based on the disappearance of the GFP signal as the tumor cells lose their expression of GFP

after cell death. However, it is known that the half-life of GFP can last from few hours to 1 day. Therefore, we need to take this factor into account to ensure our readout is not affected by the GFP half-life.

We tested the drug exposure duration to GBM xenograft slices for 24 and 48 hours. We found that the slices with 24 hrs of TMZ exposure did not show a significant response: GFP-labeled GBM cells remained in the drug exposure areas (as evaluated by epifluorescence microscopy). When we extended the duration of the drug exposure to 48 hours, we observed a significant change in fluorescence intensity at the TMZ exposure areas, indicating that the minimal exposure of TMZ to the slice should be no less than 48 hours.

7.5.3 Selective Drug Exposure to GBM Xenograft Slices

More effective cancer therapy with better treatment outcomes will require better ways to accurately predict drug efficacy in individual cancer patients [6]. Our approach – multiplexed testing of large numbers of drugs on intact tissue slices – has the potential to identify more effective therapies for individual cancer patients. To demonstrate this potential, we used glioblastoma (GBM) mouse xenografts in which GFP-labeled glioma cells can represent glioma cell death (since the glioma cells lose GFP and stop making GFP after cell death) after treatment with TMZ. TMZ (1 mM) was delivered to GBM xenograft slice cultures in each of 7 delivery channels (buffer channels were filled with culture medium without TMZ) for 48 hours. Following drug exposure, GBM slice cultures on membranes were transferred to glass-bottom petri dishes for rinsing in PBS, fixing and imaging. After treating GBM xenograft slice cultures for 48 hrs, a significantly increased cell killing as evidenced by the loss of GFP-labeled GBM cells to TMZ, is shown in Fig. 7.3b. Our results show that glioma cell loss formed "shadow" lanes over TMZ delivery channels as compared with tissue prior to drug exposure or over channels perfused with culture medium lacking TMZ (Fig. 7.3b). Confocal imaging over TMZ-exposed regions/channels (Fig. 7.3c) further confirmed the TMZ-dependent loss of GFP-labeled cells.

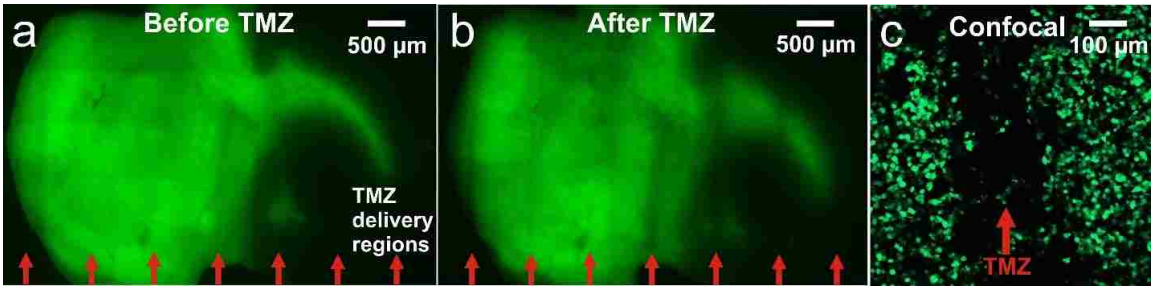

Figure 7.3: Selective killing of GFP-labeled human GBM xenograft cells by TMZ in an intact xenograft slice culture.

(a,b) Selective TMZ treatment on a GBM xenograft slice. The green areas show the GFP-labelled glioma cells within the slice. Seven parallel fluidic streams containing 1 mM TMZ (white-dashed arrows on panel a) and red arrows on panel b) were delivered to the slice with 3 buffer streams in between each of the two TMZ streams. The disappearance of GFP-labeled glioma cells was found after 48hr of TMZ delivery at the TMZ-exposed regions (b) compared to the image of the same slice before TMZ exposure (a). (c) A confocal image taken after 48hr TMZ exposure shows the loss of GFP-labeled glioma cells at the TMZ-exposed region in a spatially-defined manner.

7.5.4 Different Type of a mouse Xenograft as a drug testing model

We have also explored the possibility of using intact tumor biopsies from prostate mouse xenograft tumors for our study. The subcutaneously injected prostate xenograft tumors were provided by Dr. Robert Vessella's lab from the department of Urology. From our experience, the prostate xenograft tumors generated from different human cell lines have many differences in structure and firmness. Therefore, we chose to embed the tumor in agarose before biopsy extraction (Fig. 7.4a). Once the tumor was resected, it was quickly embedded in low-melting temperature agarose. After the agarose was solidified, the tissues were extracted from the tumor using a 600-μm or 800-μm biopsy tool (Fig. 7.4b). As a result, the core biopsies from prostate xenograft tumors have very loose structures and require careful handling in order to transfer the biopsy tissues to the membrane without falling apart.

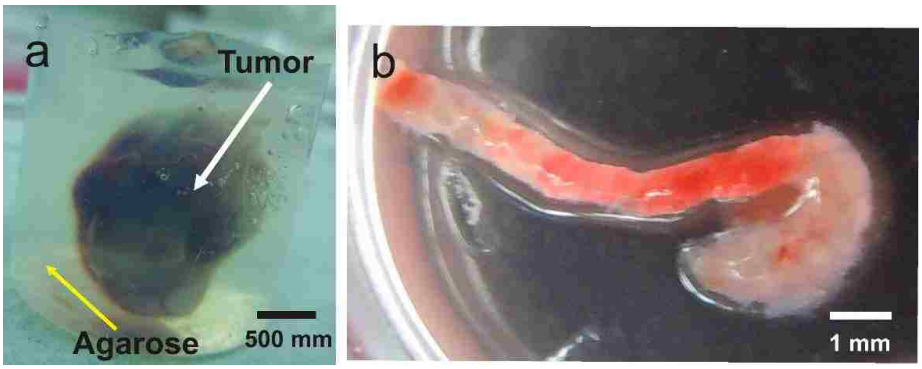

Figure 7.4: Prostate xenograft tumor biopsy.
(a) A prostate xenograft tumor was embedded in low-melting temperature agarose. (b) A prostate xenograft biopsy with a diameter of 800 µm.

To further investigate this loss structure, we sectioned the tissues and stained them with H&E to observe the morphology. For the core biopsies extracted from prostate xenograft tumors, we observed a very loose structure as the cells/tissues were barely connected within the biopsy tissue (Fig. 7.5a). The cause of the loss in structure was likely due to the acute extraction from the biopsy tool. It can also be because of the loose structure from the original tumor. Surprisingly, we found out that the continuous culture of the loose biopsy tissue allows the tumor cells to reconstruct the biopsy structure by proliferating and filling all the loose regions (Fig. 7.5b). This finding creates a potential of using prostate xenograft tumor biopsies as a model for our microfluidic high-throughput drug testing where cell proliferation is needed to reliably assess response.

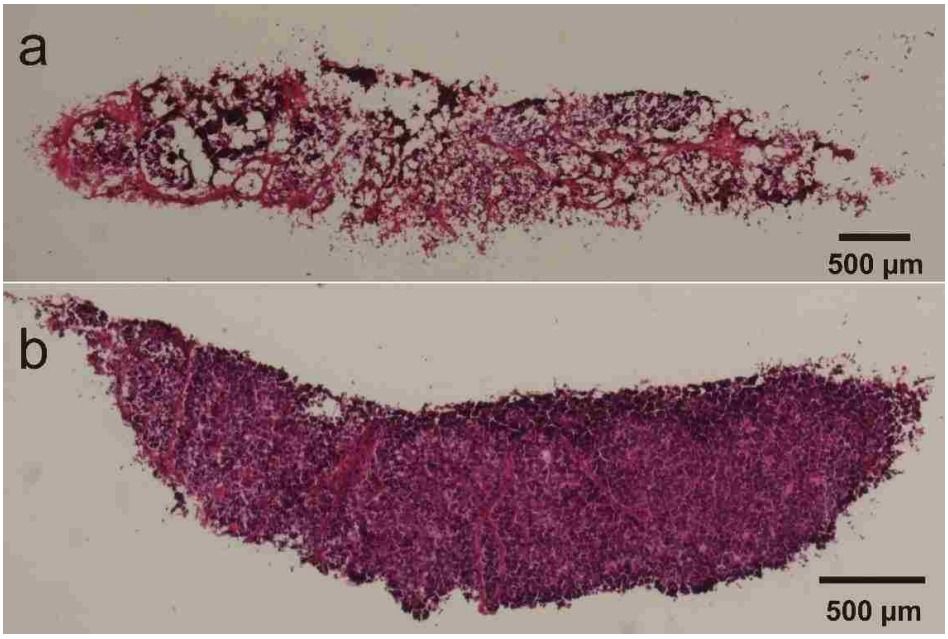

Figure 7.5: Morphology of the prostate xenograft biopsies.

Hematoxylin and eosin (H&E) staining is used to reveal the morphology of the tissue biopsies. (a) Two hours after the biopsy extraction. (b) The biopsy was cultured for a week before tissue sectioning and H&E staining.

In conclusion, mouse xenografts possess advantages to assist our study. First, the tumor cells can be characterized thoroughly before being injected in mice. Second, intact xenograft tumor tissues can be generated to mimic tumor physiology. Third, the drug testing results from intact tissues can be verified *in-vivo*. Therefore, mouse xenografts are great tools in our study for drug testing on intact tissues.

Chapter 8: Conclusions, Limitations, and Future Directions

8.1 Conclusions

The ability to identify effective treatments for individual cancer patients has the potential to improved survival and minimize toxicity. Current methods to screen drugs for patients are cumbersome, expensive and often inaccurate. Therefore, the challenge remains to develop adequate and useful methods that can rapidly test compounds on the primary tumor specimens from specific patients. As the technology advances, many methods and cell/tissue based applications have demonstrated the potential for drug screening. We demonstrated a simple microwell device to allow for accessing cell-to-cell heterogeneity from large numbers of single cells with a potential for studying tumor heterogeneity. Further, we described techniques for obtaining and culturing intact tissue slices and biopsies, which preserve the original tissue structure and have the potential to improve the accuracy of prediction in drug screening based on individual patient's tumors.

Microfluidic devices are becoming more widely used for high-throughput drug screening. In this thesis, we extended this technology and overcame many difficulties in device design by incorporating a 96-well plate and a semi-porous membrane to allow for high-throughput drug screening on intact tissues. The 96-well plate format, with all reagents loading by a pipette, resolves the traditional difficulties in interfacing a large number of inputs with a microfluidic device. This device is intuitive to operate, acts as a user-friendly tool, and is compatible with standard imaging systems. Furthermore, the integration of a semi-porous membrane in the microfluidic device enables organotypic culture, acts as an interface to separate the fluidic and culture layers, and allows for fluidic transport through the microchannels in a spatially-defined manner. In addition to the semi-porous membrane for organotypic culture, we developed a membrane transfer technique which allows the tissue culture, drug delivery and imaging to be performed on three different platforms, significantly improving the operation of each.

To demonstrate the use of our microfluidic device for drug testing on intact tissue slices, we performed chemosensitivity testing on mouse brain slices and described the complete

data analysis based on images acquired by both epifluorescent and confocal microscopy. This methodology can be easily applied to human tumor samples to quantify cell apoptosis and cell death to determine drug efficacy. We further demonstrated the feasibility of our microfluidic approach by using GBM xenograft slices and showed the drug responses in the spatially-defined exposure regions. The use of xenograft models will allow us to compare the drug responses between the *ex-vivo* slice culture model and the *in-vivo* mouse xenograft model and further accelerate the understanding of key elements related to tumor microenvironment.

In conclusion, we have overcome the key challenges involved with traditional microfluidic devices by designing an integrated device to allow large-scale drug delivery to intact tissues. Our drug testing results on mouse brain slices in conjunction with imaging acquisitions and data analysis demonstrate the feasibility of our approach. We believe this novel microfluidic approach using intact tumor tissues has the potential to replace current drug screening models with more accurate predictive power and represents a new paradigm for providing guidance to individual patients.

8.2 Limitations

For tissue extraction, we have successfully produced tissue slices and biopsies from mouse brains and livers. However, human tumor samples can be very different from these homogeneous organs. The slices and biopsies can be very difficult to produce from certain tumor samples with very soft structures. In this case, other sampling techniques should be tested (smear).

Our microfluidic device adapts the organotypic culture by interfacing a porous membrane to create an air-fluid interface to allow a high efficiency of oxygen and nutrient transport to the tissue under normoxia conditions. However, it is well known that this membrane interface method only maintains the culture of the tissue slice with a thickness less than 200 μm (the slice is initially produced at a thickness of 300~400 μm and gets thinner overtime during the culture). This limited culture thickness is because of the limitation of diffusion in oxygen and nutrients transport to the tissue. This implies that the thickness of

the cultured tissue is determined by the culture method. Note that it is difficult to produce tissue slices thinner than 200 µm.

Our 96-well plate-based microfluidic device has 80 inputs and allows the multiplexed screening of up to 80 different drugs or drug combinations. However, the size of the tissue slice might not cover the full culture area with 80 delivery channels below. For example, the size of an embryonic mouse brain slice normally covers a quarter of the culture area with only 20 delivery channels underneath. This limitation is based on the original size of the tissue before slicing and is certainly difficult to control. Furthermore, the capacity of each well reservoir in a 96-well plate is about 400 µL which can sustain the drug delivery up to 2 days under our flow rate setting. If longer drug delivery is required, refilling the wells with fresh solutions is needed.

The concept of using intact tumor tissue for drug testing is to preserve the tissue integrity with the original tumor microenvironment. However, the lack of microvasculature and the potential loss of cell function are definitely concerns. Unlike other *in-vitro* culture models, the complexity of the cell types and structures in an intact tumor tissue makes them difficult to understand the pathways associated with the suppression of the tumor cell growth. To address this issue, additional efforts in molecular cell studies should provide more information.

8.3 Future directions

Here we discuss future directions based on our preliminary work, and indicate how what we have learned can better inform the design, fabrication and use of microfluidic platforms to use to determine drug response profiles. In the device technology, we discuss the possibility of increasing the drug delivery throughput by using a 384 well-plate. Further, we describe the potential of using 3D printing technology to replace the traditional soft lithography technique for easier device fabrication. From the preclinical aspect, we provide experiences in slicing human tumors for further drug testing experiments.

8.3.1 Limitations in Device Design

In our device design, the width of the delivery channels and the distance between each of two channels are based on several considerations, including the fabrication limit (soft lithography), the size of the culture area and the selective drug exposure area from each delivery channel. In principle, the smaller the channels are (smaller channel and gap widths), the more compounds can be screened on a tissue slice. However, the limited numbers of cells at small drug exposure areas might be difficult to provide statistically reliable response data. In addition to the numbers of cells that can be used for data analysis, the difficulty in fabricating small open channels (less than 100 μm in channel width) using soft lithography and exclusion molding technique remains as a major limitation. Based on our prior experience, we suggest the design of the channel width to be 100 μm and the gap in between each of two channels to be 50~150 μm. In this design, the numbers of cells at each drug exposed area should be sufficient for data analysis and the fabrication of the open channels can still be achieved with a high yield.

8.3.2 Tissue heterogeneity

To address tissue heterogeneity, acquiring data from different regions of a slice which have been delivered the same compound can potentially reduce the concern of tissue heterogeneity to the drug response result. In order to deliver the same compound to multiple regions of a slice, we can either use multiple delivery channels to flow the same compound or take an advantage of our culture membrane transfer technique to simply rotate the tissue slice to increase the drug exposure area at different regions. In both cases, the data can be acquired from multiple regions of the slice and can be analyzed by averaging to determine the final result.

8.3.3 Expand Drug Delivery Throughput Using a 384-Well Plate

Increasing throughput is always beneficial as we can test more compounds from the same amount of tissue samples. Based on our preliminary testing, we found that it is possible to increase throughput by integrating a bottomless 384-well plate with a redesigned microfluidic chip as shown in Fig. 8.1. We adopted the same concept by sacrificing 96 wells at the central region of the 384-well plate for creating a culture space. Therefore,

the device has 288 inputs (Fig. 8.1a). Two interface layers (thin PDMS through hole and channel network) were created by exclusion molding directly from the SU8 masters (Fig. 8.1a) to ensure accurate positions of all the connection holes, rather than punching them manually. The microfluidic chip was fabricated using the same exclusion molding technique with a divided culture areas (Fig. 8.1a) to allow for the full coverage of each culture area by a 30-mm PTFE porous membrane. Each culture area contains 144 open microchannels and each channel is 50-µm wide with the spacing of 90 µm in between each of two open microchannels. All the resistances of the channels are balanced to allow for a simple operation by one outlet. Figure 8.1b shows the prototype of a 384-well plate-based microfluidic device.

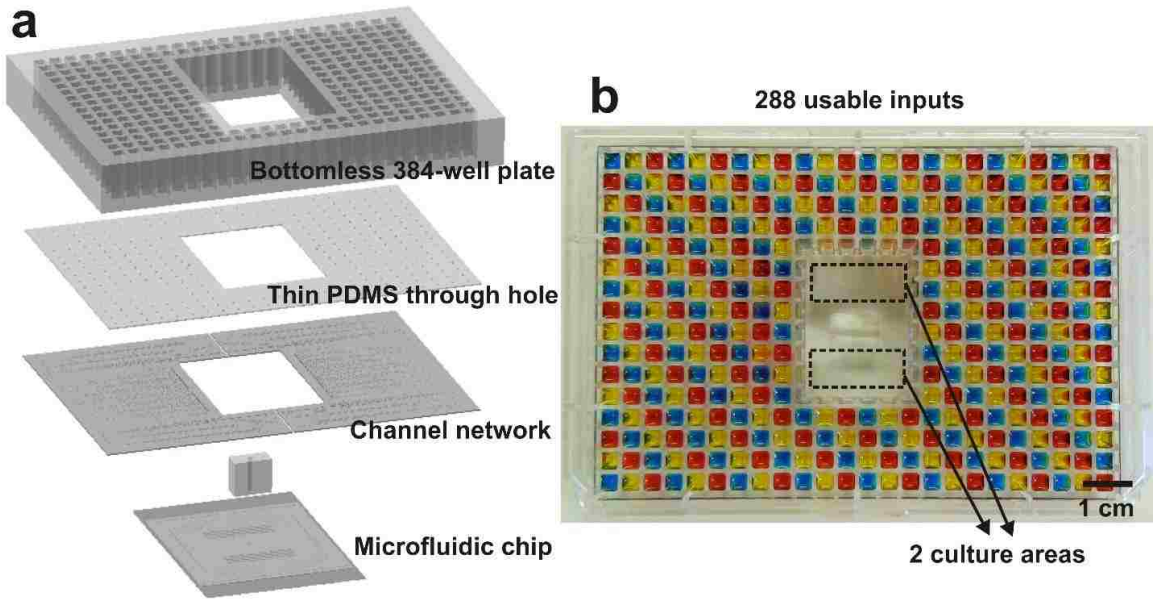

Figure 8.1: 384-well plate-based microfluidic device design.
(a) Layer-by-layer schematic view of the device. The device includes (from top to bottom) a modified bottomless 384-well plate featuring 288 inlet wells after the central 96 wells have been removed; an exclusion-molded PDMS through hole layer; a PDMS channel network layer; and the microfluidic chip. (b) Microfluidic platform loaded with three dyes (yellow, blue and red) in sequence to demonstrate an increase in throughput by 3.5 times from the prior device.

8.3.4 3D Printing to Facilitate Device Fabrication

One major hurdle to using our microfluidic technology for drug testing is the difficulty in the device fabrication process. Our 96-well plate-based device offers simple and reliable operations. However, the fabrication process not only requires experienced microfluidic specialists but is very time consuming. Therefore, advanced fabrication techniques allowing for simpler integration with the 96-well plate to improve the speed of the fabrication process are urgently needed.

To address this fabrication concern, our laboratory has been exploring the possibility of fabricating the 96-well plate-based device using stereolithography. Stereolithography is a manufacturing process which uses an UV laser to cure liquid curable photopolymers (resin) layer-by-layer to build a 3D object. Unlike soft lithography which is labor-intensive with many assembling processes to build an integrated device, 3D printing technique allows to use 3-D computer aided design (CAD) software to design a version of the proposed microfluidic device and fabricate the full device with all the fluidic layers interconnected in one printing process.

We have explored 3D printing techniques in small scales and prepared for two alternatives to overcome the limitation of the current printing resolution for our microfluidic device. First, the resolution of closed features in 3D printing is significantly less than the resolution of open features (500 µm for closed features vs 100 µm for open features). In our device, the channel network layer contains small channel features which are embedded in the middle of the device and required to be printed as closed features (closed channels). To our knowledge, it is impossible to print all the fluid channels on one layer as the resolution of 3D printing in closed channels is limited (Fig. 8.2a). To resolve this issue, we take an advantage of the three dimensional design space to create a network of channels that exist on multiple planes (Fig. 8.2b). We divide a single channel network layer (Fig. 8.2a) into four layers (Fig. 8.2b) to achieve the same purpose. Second, our microfluidic chip has small channel features at the bottom of the device. We purpose to create a high-resolution stencil using PDMS to integrate with the existing 3D printing technique. The stencil will be positioned in respect to the orientation of the

device prior to printing. Then the stencil will be filled and cured with resin before the rest of the layers printed to build up on top of the stencil. Once the 3D printed device is completed and the stencil is removed (stencil can be reused), the bottom of the device will be bonded onto a flat PDMS substrate to complete the fabrication process.

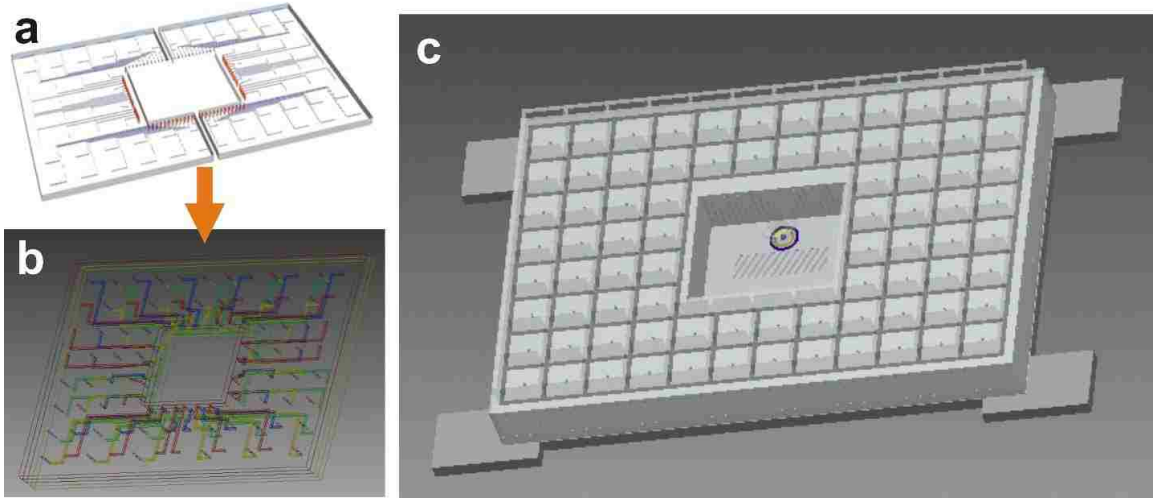

Figure 8.2: The concept of a 3D printed 96-well plate-based microfluidic device.
(a) The original channel network layer fabricated by PDMS soft lithography. (b) The channel network layer designed for the fabrication of 3D printing. Different colors represent the design of the channels at different layers (c) A conceptual 3D printed 96-well plate-based microfluidic device.

8.3.5 Human Glioblastoma

One of the major advantages in using our approach is the ability to directly use patient's tumor samples for testing large numbers of drugs in our microfluidic device. We attempted to use patient's GBM tumor samples in a pilot study, which provided us with valuable experience for future preparations.

Based on our pilot study, human tumor tissues have less defined shapes and can be very soft in structure. We have tried to directly slice the tumor samples using the same technique for producing mouse brain slices and the result was unsuccessful as the tumor sample was consistently jammed by the cutting blade during slicing, resulting in a failure

to produce tissue slices (Fig. 8.3a). Therefore, we recommend embedding the tissue sample in low-melting temperature agarose gel prior to slicing. The tissue with agarose gel support is more likely to allow for producing slices with a defined thickness for organotypic culture (Fig. 8.3b).

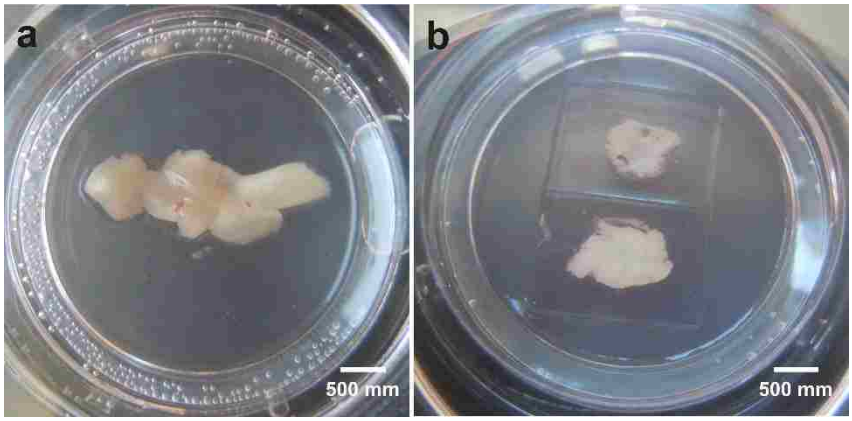

Figure 8.3: Tumor slices produced by vibratome with and without agarose support. (a) Without agarose embedding, we were not able to produce tissue slices from a small human GBM tumor chunk. The resulting tissue after sliced turned into a thick tissue. (b) The tumor slice was produced with agarose embedding. The resulting slices have well-defined thickness with agarose frames around the tissue. Sometimes, it is be hard to remove the tissue slice from the supporting agarose. In this case, the full piece of tissue slice with the surrounding agarose can be directly cultured on the porous membrane.

We have made some attempts to use human GBM samples for drug screening. For each experiment, we were able to obtain 5~6 quality slices from a human GBM tumor sample provided by Dr. Robert Rostomily. We then we performed our microfluidic drug testing experiment using TMZ on each slice once every two days, starting on the second day of culture. After treatment, we did not see any difference between the control and the TMZ treated regions. However, we could not make any further conclusions based on this study as the culture conditions were not optimized (the tumor slices were unhealthy based on our controls). These pilot studies allowed us to better understand the practical issues involved with testing human samples, including obtaining the slices, culture conditions, and readouts, which can be useful for further human experiments.

For future drug testing on human samples, we recommend optimizing culture conditions using vital dye staining based on the interval for medium replacement during culture and the duration of the slice culture prior to being tested. Despite the high variability in tissue samples can be very different among patients, well-designed experiments for evaluating the culture conditions should still provide an optimal protocol for general culture of human tissue samples. Without an establishment of a healthy culture, readouts from our direct viability assessment become meaningless.

The tumor heterogeneity within each tumor sample/slice is unavoidable. To address this issue, we can use our device to expose the same drug to multiple spots of the same tumor slice and conclude the result based on multiple regions, in which the traditional slice culture technique cannot achieve. We believe the readouts from multiple regions will decrease the chance of false results from the tumor heterogeneity.

To further extract more therapeutic information from the tumor slice culture system, molecular analysis should be incorporated to confirm the types of tumors with known molecular biomarkers to assist our study. We believe the advance of this intact tumor tissue model will allow us to identify effective therapies for individual tumors and patients, minimize avoidable toxicity, and ultimately benefit the patients.

Bibliography

1. Siegel, R., D. Naishadham, and A. Jemal, *Cancer statistics, 2013.* CA: a cancer journal for clinicians, 2013. **63**(1): p. 11-30.
2. Adams, C.P. and V.V. Brantner, *Estimating the cost of new drug development: is it really $802 million?* Health Affairs, 2006. **25**(2): p. 420-428.
3. Hutchinson, L. and R. Kirk, *High drug attrition rates—where are we going wrong?* Nature Reviews Clinical Oncology, 2011. **8**(4): p. 189-190.
4. Francia, G. and R.S. Kerbel, *Raising the bar for cancer therapy models.* Nature biotechnology, 2010. **28**(6): p. 561-562.
5. Suggitt, M. and M.C. Bibby, *50 years of preclinical anticancer drug screening: empirical to target-driven approaches.* Clinical Cancer Research, 2005. **11**(3): p. 971-981.
6. *Provocative Questions*. 2011; Available from: http://provocativequestions.nci.nih.gov/rfa.
7. Bild, A.H., et al., *Oncogenic pathway signatures in human cancers as a guide to targeted therapies.* Nature, 2006. **439**(7074): p. 353-357.
8. Peehl, D., *Primary cell cultures as models of prostate cancer development.* Endocrine-related cancer, 2005. **12**(1): p. 19-47.
9. Hoffman, R.M., *Orthotopic transplant mouse models with green fluorescent protein-expressing cancer cells to visualize metastasis and angiogenesis.* Cancer and Metastasis Reviews, 1998. **17**(3): p. 271-277.
10. Onn, A., et al., *Development of an orthotopic model to study the biology and therapy of primary human lung cancer in nude mice.* Clinical Cancer Research, 2003. **9**(15): p. 5532-5539.
11. Gillet, J.-P., S. Varma, and M.M. Gottesman, *The clinical relevance of cancer cell lines.* Journal of the National Cancer Institute, 2013. **105**(7): p. 452-458.
12. Gazdar, A.F., et al., *Lung cancer cell lines as tools for biomedical discovery and research.* Journal of the National Cancer Institute, 2010. **102**(17): p. 1310-1321.
13. Kao, J., et al., *Molecular profiling of breast cancer cell lines defines relevant tumor models and provides a resource for cancer gene discovery.* PloS one, 2009. **4**(7): p. e6146.
14. Fang, Y., et al., *Molecular characterization of permanent cell lines from primary, metastatic and recurrent malignant peripheral nerve sheath tumors (MPNST) with underlying neurofibromatosis-1.* Anticancer research, 2009. **29**(4): p. 1255-1262.
15. Tomlinson, G.E., et al., *Characterization of a breast cancer cell line derived from a germ-line BRCA1 mutation carrier.* Cancer research, 1998. **58**(15): p. 3237-3242.
16. Daenen, L.G.M., *Host-Mediated Mechanisms of Resistance to Antitumor Therapies*2013: Utrecht University.
17. Bissell, M.J., H.G. Hall, and G. Parry, *How does the extracellular matrix direct gene expression?* Journal of theoretical biology, 1982. **99**(1): p. 31-68.
18. Cukierman, E., R. Pankov, and K.M. Yamada, *Cell interactions with three-dimensional matrices.* Current opinion in cell biology, 2002. **14**(5): p. 633-640.

19. Pampaloni, F., E.G. Reynaud, and E.H. Stelzer, *The third dimension bridges the gap between cell culture and live tissue.* Nature reviews Molecular cell biology, 2007. **8**(10): p. 839-845.
20. Ghosh, S., et al., *Three-dimensional culture of melanoma cells profoundly affects gene expression profile: A high density oligonucleotide array study.* Journal of cellular physiology, 2005. **204**(2): p. 522-531.
21. Abbott, A., *Cell culture: biology's new dimension.* Nature, 2003. **424**(6951): p. 870-872.
22. Lee, J., M.J. Cuddihy, and N.A. Kotov, *Three-dimensional cell culture matrices: state of the art.* Tissue Engineering Part B: Reviews, 2008. **14**(1): p. 61-86.
23. Morton, C.L. and P.J. Houghton, *Establishment of human tumor xenografts in immunodeficient mice.* Nature protocols, 2007. **2**(2): p. 247-250.
24. McCutcheon, I.E., et al., *Intracranial injection of human meningioma cells in athymic mice: an orthotopic model for meningioma growth.* Journal of neurosurgery, 2000. **92**(2): p. 306-314.
25. Euhus, D.M., et al., *Tumor measurement in the nude mouse.* Journal of surgical oncology, 1986. **31**(4): p. 229-234.
26. Tomayko, M.M. and C.P. Reynolds, *Determination of subcutaneous tumor size in athymic (nude) mice.* Cancer chemotherapy and pharmacology, 1989. **24**(3): p. 148-154.
27. Demetrius, L., *Of mice and men.* EMBO reports, 2005. **6**(1S): p. S39-S44.
28. Killion, J.J., R. Radinsky, and I.J. Fidler, *Orthotopic models are necessary to predict therapy of transplantable tumors in mice.* Cancer and Metastasis Reviews, 1998. **17**(3): p. 279-284.
29. Scholz, C.C., et al., *Correlation of drug response in patients and in the clonogenic assay with solid human tumour xenografts.* European Journal of Cancer and Clinical Oncology, 1990. **26**(8): p. 901-905.
30. Johnson, J., et al., *Relationships between drug activity in NCI preclinical in vitro and in vivo models and early clinical trials.* British journal of cancer, 2001. **84**(10): p. 1424.
31. Kerbel, R.S., *Human tumor xenografts as predictive preclinical models for anticancer drug activity in humans: better than commonly perceived—but they can be improved.* Cancer biology & therapy, 2003. **2**: p. 133-138.
32. Nyberg, P., T. Salo, and R. Kalluri, *Tumor microenvironment and angiogenesis.* Frontiers in bioscience: a journal and virtual library, 2007. **13**: p. 6537-6553.
33. Hazlehurst, L.A. and W.S. Dalton, *Mechanisms associated with cell adhesion mediated drug resistance (CAM-DR) in hematopoietic malignancies.* Cancer and Metastasis Reviews, 2001. **20**(1-2): p. 43-50.
34. Flach, E.H., et al., *Fibroblasts contribute to melanoma tumor growth and drug resistance.* Molecular pharmaceutics, 2011. **8**(6): p. 2039-2049.
35. Kim, S.-J., et al., *Astrocytes upregulate survival genes in tumor cells and induce protection from chemotherapy.* Neoplasia (New York, NY), 2011. **13**(3): p. 286.
36. Hida, K., et al., *Tumour endothelial cells acquire drug resistance in a tumour microenvironment.* Journal of biochemistry, 2013. **153**(3): p. 243-249.

37. Straussman, R., et al., *Tumour micro-environment elicits innate resistance to RAF inhibitors through HGF secretion.* Nature, 2012. **487**(7408): p. 500-504.
38. Huang, Q., et al., *Caspase 3-mediated stimulation of tumor cell repopulation during cancer radiotherapy.* Nature medicine, 2011. **17**(7): p. 860-866.
39. Hanahan, D. and R.A. Weinberg, *Hallmarks of cancer: the next generation.* Cell, 2011. **144**(5): p. 646-674.
40. Warburg, O., *Experiments on surviving carcinoma tissue: methods.* Biochem Z, 1923. **142**: p. 317-330.
41. Gähwiler, B., et al., *Organotypic slice cultures: a technique has come of age.* Trends in neurosciences, 1997. **20**(10): p. 471-477.
42. Haas, H., B. Schaerer, and M. Vosmansky, *A simple perfusion chamber for the study of nervous tissue slices in vitro.* Journal of neuroscience methods, 1979. **1**(4): p. 323-325.
43. Stoppini, L., P.-A. Buchs, and D. Muller, *A simple method for organotypic cultures of nervous tissue.* Journal of neuroscience methods, 1991. **37**(2): p. 173-182.
44. Benbrook, D.M., *Organotypic cultures represent tumor microenvironment for drug testing.* Drug Discovery Today: Disease Models, 2006. **3**(2): p. 143-148.
45. Haas, H.L., B. Schaerer, and M. Vosmansky, *A simple perfusion chamber for the study of nervous tissue slices in vitro.* Journal of Neuroscience Methods, 1979. **1**(4): p. 323-325.
46. Merz, F., et al., *Organotypic slice cultures of human glioblastoma reveal different susceptibilities to treatments.* Neuro-oncology, 2013. **15**(6): p. 670-681.
47. de Graaf, I.A.M., et al., *Preparation and incubation of precision-cut liver and intestinal slices for application in drug metabolism and toxicity studies.* Nat. Protocols, 2010. **5**(9): p. 1540-1551.
48. Vaira, V., et al., *Preclinical model of organotypic culture for pharmacodynamic profiling of human tumors.* Proceedings of the National Academy of Sciences, 2010. **107**(18): p. 8352-8356.
49. Noraberg, J., et al., *Organotypic hippocampal slice cultures for studies of brain damage, neuroprotection and neurorepair.* Curr Drug Targets CNS Neurol Disord, 2005. **4**(4): p. 435-52.
50. Murry, B.P., et al., *Heparanase mechanisms of melanoma metastasis to the brain: Development and use of a brain slice model.* Journal of Cellular Biochemistry, 2006. **97**(2): p. 217-225.
51. Vaira, V., et al., *Preclinical model of organotypic culture for pharmacodynamic profiling of human tumors.* Proceedings of the National Academy of Sciences, 2010. **107**(18): p. 8352-8356.
52. Donson, A.M., et al., *MGMT promoter methylation correlates with survival benefit and sensitivity to temozolomide in pediatric glioblastoma.* Pediatric blood & cancer, 2007. **48**(4): p. 403-407.
53. Hegi, M.E., et al., *MGMT gene silencing and benefit from temozolomide in glioblastoma.* New England Journal of Medicine, 2005. **352**(10): p. 997-1003.

54. Kim, Y.S., et al., *MGMT gene promoter methylation as a potent prognostic factor in glioblastoma treated with temozolomide-based chemoradiotherapy: a single-institution study.* International Journal of Radiation Oncology* Biology* Physics, 2012. **84**(3): p. 661-667.
55. Whitesides, G.M., *The origins and the future of microfluidics.* Nature, 2006. **442**(7101): p. 368-373.
56. Huang, Y., J.C. Williams, and S.M. Johnson, *Brain slice on a chip: opportunities and challenges of applying microfluidic technology to intact tissues.* Lab on a Chip, 2012. **12**(12): p. 2103-2117.
57. Webster, A., et al., *A microfluidic device for tissue biopsy culture and interrogation.* Analytical Methods, 2010. **2**(8): p. 1005-1007.
58. Hattersley, S.M., et al., *A microfluidic system for testing the responses of head and neck squamous cell carcinoma tissue biopsies to treatment with chemotherapy drugs.* Annals of biomedical engineering, 2012. **40**(6): p. 1277-1288.
59. Blake, A., et al., *Multilayer PDMS microfluidic chamber for controlling brain slice microenvironment.* Lab on a Chip, 2007. **7**(7): p. 842-849.
60. Kaigala, G.V., R.D. Lovchik, and E. Delamarche, *Microfluidics in the "Open Space" for Performing Localized Chemistry on Biological Interfaces.* Angewandte Chemie International Edition, 2012. **51**(45): p. 11224-11240.
61. Wang, B., et al., *A microfluidic approach to pulsatile delivery of drugs for neurobiological studies.* Microelectromechanical Systems, Journal of, 2012. **21**(1): p. 53-61.
62. Queval, A., et al., *Chamber and microfluidic probe for microperfusion of organotypic brain slices.* Lab on a Chip, 2010. **10**(3): p. 326-334.
63. Kamiyama, H., et al., *Personalized chemotherapy profiling using cancer cell lines from selectable mice.* Clinical Cancer Research, 2013. **19**(5): p. 1139-1146.
64. Dong, X., et al., *Patient-Derived First Generation Xenografts of Non–Small Cell Lung Cancers: Promising Tools for Predicting Drug Responses for Personalized Chemotherapy.* Clinical Cancer Research, 2010. **16**(5): p. 1442-1451.
65. Kamb, A., *What's wrong with our cancer models?* Nature reviews Drug discovery, 2005. **4**(2): p. 161-165.
66. Steel, G.G., *Growth kinetics of tumours: cell population kinetics in relation to the growth and treatment of cancer.* 1977.
67. Wright, N.A. and M. Alison, *The biology of epithelial cell populations*. Vol. 2. 1984: Clarendon press Oxford.
68. Campisi, J., *Aging, cellular senescence, and cancer.* Annual review of physiology, 2013. **75**: p. 685-705.
69. Fisher, R., L. Pusztai, and C. Swanton, *Cancer heterogeneity: implications for targeted therapeutics.* British journal of cancer, 2013. **108**(3): p. 479-485.
70. Franken, N.A., et al., *Clonogenic assay of cells in vitro.* Nature protocols, 2006. **1**(5): p. 2315-2319.
71. Terasaki, P.I. and J.D. McClelland, *Microdroplet assay of human serum cytotoxins.* 1964.

72. Kueng, W., E. Silber, and U. Eppenberger, *Quantification of cells cultured on 96-well plates.* Analytical biochemistry, 1989. **182**(1): p. 16-19.
73. Thangavel, S., et al., *Human RECQ1 and RECQ4 helicases play distinct roles in DNA replication initiation.* Molecular and cellular biology, 2010. **30**(6): p. 1382-1396.
74. Singh, D.K., et al., *RecQ helicases in DNA double strand break repair and telomere maintenance.* Mutation Research/Fundamental and Molecular Mechanisms of Mutagenesis, 2012. **736**(1): p. 15-24.
75. Sidorova, J.M., et al., *Distinct functions of human RECQ helicases WRN and BLM in replication fork recovery and progression after hydroxyurea-induced stalling.* DNA repair, 2013. **12**(2): p. 128-139.
76. Monnat Jr, R.J. *Human RECQ helicases: roles in DNA metabolism, mutagenesis and cancer biology*. in *Seminars in cancer biology*. 2010. Elsevier.
77. Mao, F.J., et al., *The human WRN and BLM RecQ helicases differentially regulate cell proliferation and survival after chemotherapeutic DNA damage.* Cancer research, 2010. **70**(16): p. 6548-6555.
78. Tyson, D.R., et al., *Fractional proliferation: a method to deconvolve cell population dynamics from single-cell data.* Nature methods, 2012. **9**(9): p. 923-928.
79. Hsu, C.-H., C. Chen, and A. Folch, *"Microcanals" for micropipette access to single cells in microfluidic environments.* Lab Chip, 2004. **4**(5): p. 420-424.
80. Sunkara, V., et al., *Simple room temperature bonding of thermoplastics and poly (dimethylsiloxane).* Lab on a Chip, 2011. **11**(5): p. 962-965.
81. Debacq-Chainiaux, F., et al., *Protocols to detect senescence-associated beta-galactosidase (SA-βgal) activity, a biomarker of senescent cells in culture and in vivo.* Nature protocols, 2009. **4**(12): p. 1798-1806.
82. Ly, D.H., et al., *Mitotic misregulation and human aging.* Science, 2000. **287**(5462): p. 2486-2492.
83. Chen, C. and A. Folch, *A high-performance elastomeric patch clamp chip.* Lab on a Chip, 2006. **6**(10): p. 1338-1345.
84. Rettig, J.R. and A. Folch, *Large-scale single-cell trapping and imaging using microwell arrays.* Analytical chemistry, 2005. **77**(17): p. 5628-5634.
85. Di Carlo, D., L.Y. Wu, and L.P. Lee, *Dynamic single cell culture array.* Lab on a Chip, 2006. **6**(11): p. 1445-1449.
86. Jackson, A.L. and P.S. Linsley, *Recognizing and avoiding siRNA off-target effects for target identification and therapeutic application.* Nature reviews Drug discovery, 2010. **9**(1): p. 57-67.
87. Saintigny, Y., et al., *Homologous recombination resolution defect in Werner syndrome.* Molecular and cellular biology, 2002. **22**(20): p. 6971-6978.
88. Marx, U. and V. Sandig, *Drug Testing in Vitro: Breakthroughs and Trends in Cell Culture Technology*2007: John Wiley & Sons.
89. Gähwiler, B., *Organotypic monolayer cultures of nervous tissue.* Journal of neuroscience methods, 1981. **4**(4): p. 329-342.

90. Lindner, G. and G. Grosse, *[Morphometric studies of the rat hippocampus after static and dynamic cultivation].* Zeitschrift fur mikroskopisch-anatomische Forschung, 1981. **96**(3): p. 485-496.
91. Koerner, J.F. and C.W. Cotman, *A microperfusion chamber for brain slice pharmacology.* Journal of neuroscience methods, 1983. **7**(3): p. 243-251.
92. Gähwiler, B., *Organotypic cultures of neural tissue.* Trends in neurosciences, 1988. **11**(11): p. 484-489.
93. Johnson, S. and P. Rabinovitch, *Ex vivo imaging of excised tissue using vital dyes and confocal microscopy.* Current Protocols in Cytometry, 2012: p. 9.39. 1-9.39. 18.
94. Monette, R., et al., *A fluorescence confocal assay to assess neuronal viability in brain slices.* Brain Research Protocols, 1998. **2**(2): p. 99-108.
95. Adamchik, Y., et al., *Methods to induce primary and secondary traumatic damage in organotypic hippocampal slice cultures.* Brain Research Protocols, 2000. **5**(2): p. 153-158.
96. Birgbauer, E., T.S. Rao, and M. Webb, *Lysolecithin induces demyelination in vitro in a cerebellar slice culture system.* Journal of neuroscience research, 2004. **78**(2): p. 157-166.
97. Krassioukov, A.V., et al., *An in vitro model of neurotrauma in organotypic spinal cord cultures from adult mice.* Brain Research Protocols, 2002. **10**(2): p. 60-68.
98. Newell, D., et al., *Glutamate and non-glutamate receptor mediated toxicity caused by oxygen and glucose deprivation in organotypic hippocampal cultures.* The Journal of neuroscience, 1995. **15**(11): p. 7702-7711.
99. Østergaard, K., B. Finsen, and J. Zimmer, *Organotypic slice cultures of the rat striatum: an immunocytochemical, histochemical and in situ hybridization study of somatostatin, neuropeptide Y, nicotinamide adenine dinucleotide phosphate-diaphorase, and enkephalin.* Experimental brain research, 1995. **103**(1): p. 70-84.
100. Rytter, A., et al., *Mouse hippocampal organotypic tissue cultures exposed to in vitro "ischemia" show selective and delayed CA1 damage that is aggravated by glucose.* Journal of Cerebral Blood Flow & Metabolism, 2003. **23**(1): p. 23-33.
101. Hama, H., et al., *Scale: a chemical approach for fluorescence imaging and reconstruction of transparent mouse brain.* Nature neuroscience, 2011. **14**(11): p. 1481-1488.
102. Kuwajima, T., et al., *ClearT: a detergent-and solvent-free clearing method for neuronal and non-neuronal tissue.* Development, 2013. **140**(6): p. 1364-1368.
103. Chung, K., et al., *Structural and molecular interrogation of intact biological systems.* Nature, 2013.
104. Dittrich, P.S. and A. Manz, *Lab-on-a-chip: microfluidics in drug discovery.* Nature reviews Drug discovery, 2006. **5**(3): p. 210-218.
105. Hung, P.J., et al., *Continuous perfusion microfluidic cell culture array for high-throughput cell-based assays.* Biotechnology and bioengineering, 2005. **89**(1): p. 1-8.
106. Fernandes, T.G., et al., *High-throughput cellular microarray platforms: applications in drug discovery, toxicology and stem cell research.* Trends in biotechnology, 2009. **27**(6): p. 342-349.

107. van Midwoud, P.M., et al., *Microfluidic biochip for the perifusion of precision-cut rat liver slices for metabolism and toxicology studies.* Biotechnology and bioengineering, 2010. **105**(1): p. 184-194.
108. Hattersley, S.M., J. Greenman, and S.J. Haswell, *Study of ethanol induced toxicity in liver explants using microfluidic devices.* Biomedical microdevices, 2011. **13**(6): p. 1005-1014.
109. Folch, A., et al., *Microfabricated elastomeric stencils for micropatterning cell cultures.* Journal of biomedical materials research, 2000. **52**(2): p. 346-353.
110. Duffy, D.C., et al., *Rapid prototyping of microfluidic systems in poly (dimethylsiloxane).* Analytical chemistry, 1998. **70**(23): p. 4974-4984.
111. Di Carlo, D., *Inertial microfluidics.* Lab on a Chip, 2009. **9**(21): p. 3038-3046.
112. Folch, A., *Introduction to BioMEMS*2012: CRC Press.
113. Mohamed, H., *Use of Microfluidic Technology for Cell Separation.* blood, 2012. **1**: p. 3.
114. Cooksey, G.A., A.L. Plant, and J. Atencia, *A vacuum manifold for rapid world-to-chip connectivity of complex PDMS microdevices.* Lab on a Chip, 2009. **9**(9): p. 1298-1300.
115. Kalyanasundaram, S., V. Calhoun, and K. Leong, *A finite element model for predicting the distribution of drugs delivered intracranially to the brain.* American Journal of Physiology-Regulatory, Integrative and Comparative Physiology, 1997. **273**(5): p. R1810-R1821.
116. Choi, C.J. and B.T. Cunningham, *A 96-well microplate incorporating a replica molded microfluidic network integrated with photonic crystal biosensors for high throughput kinetic biomolecular interaction analysis.* Lab on a Chip, 2007. **7**(5): p. 550-556.
117. Lee, M.J., et al., *Sequential application of anticancer drugs enhances cell death by rewiring apoptotic signaling networks.* Cell, 2012. **149**(4): p. 780-794.
118. Meads, M.B., L.A. Hazlehurst, and W.S. Dalton, *The bone marrow microenvironment as a tumor sanctuary and contributor to drug resistance.* Clinical Cancer Research, 2008. **14**(9): p. 2519-2526.
119. Pampaloni, F., E.H. Stelzer, and A. Masotti, *Three-dimensional tissue models for drug discovery and toxicology.* Recent patents on biotechnology, 2009. **3**(2): p. 103-117.
120. Stoff-Khalili, M.A., et al., *Preclinical evaluation of transcriptional targeting strategies for carcinoma of the breast in a tissue slice model system.* Breast Cancer Res, 2005. **7**(6): p. R1141-R1152.
121. Omura, S., et al., *A new alkaloid AM-2282 OF Streptomyces origin. Taxonomy, fermentation, isolation and preliminary characterization.* The Journal of antibiotics, 1977. **30**(4): p. 275-282.
122. Karaman, M.W., et al., *A quantitative analysis of kinase inhibitor selectivity.* Nature biotechnology, 2008. **26**(1): p. 127-132.
123. Koh, J.-Y., et al., *Staurosporine-induced neuronal apoptosis.* Experimental neurology, 1995. **135**(2): p. 153-159.
124. Gescher, A., *Analogs of staurosporine: potential anticancer drugs?* General Pharmacology: The Vascular System, 1998. **31**(5): p. 721-728.

125. Crump, K., et al., *Fundamental carcinogenic processes and their implications for low dose risk assessment.* Cancer research, 1976. **36**(9 Part 1): p. 2973-2979.
126. Eaton, D.L. and C.D. Klaassen, *Principles of toxicology.* Casarett and Doull's Toxicology: The basic science of poisons, 1996. **1**: p. 13-48.
127. Sebaugh, J., *Guidelines for accurate EC50/IC50 estimation.* Pharmaceutical statistics, 2011. **10**(2): p. 128-134.
128. Tchoukalova, Y.D., et al., *A quick, reliable, and automated method for fat cell sizing.* Journal of lipid research, 2003. **44**(9): p. 1795-1801.
129. Girish, V. and A. Vijayalakshmi, *Affordable image analysis using NIH Image/ImageJ.* Indian journal of cancer, 2004. **41**(1): p. 47.
130. Wu, K., et al., *Differential expression of GFAP in early v late AMD: a quantitative analysis.* British journal of ophthalmology, 2003. **87**(9): p. 1159-1166.
131. Katayama, A., et al., *Expressions of matrix metalloproteinases in early-stage oral squamous cell carcinoma as predictive indicators for tumor metastases and prognosis.* Clinical Cancer Research, 2004. **10**(2): p. 634-640.
132. (CBTRUS), C.B.T.R.o.t.U.S., *CBTRUS Statistical Report: Primary Brain and Central Nervous System Tumors Diagnosed in Eighteen States in 2002–2006.*, 2009.
133. Sottoriva, A., et al., *Intratumor heterogeneity in human glioblastoma reflects cancer evolutionary dynamics.* Proceedings of the National Academy of Sciences, 2013. **110**(10): p. 4009-4014.
134. Sun, Y., et al., *Treatment-induced damage to the tumor microenvironment promotes prostate cancer therapy resistance through WNT16B.* Nature medicine, 2012. **18**(9): p. 1359-1368.
135. Nakasone, E.S., et al., *Imaging tumor-stroma interactions during chemotherapy reveals contributions of the microenvironment to resistance.* Cancer cell, 2012. **21**(4): p. 488-503.
136. Newlands, E., et al., *Temozolomide: a review of its discovery, chemical properties, pre-clinical development and clinical trials.* Cancer treatment reviews, 1997. **23**(1): p. 35-61.
137. Van Genugten, J., et al., *Effectiveness of temozolomide for primary glioblastoma multiforme in routine clinical practice.* Journal of neuro-oncology, 2010. **96**(2): p. 249-257.
138. Johnson, D.R. and B.P. O'Neill, *Glioblastoma survival in the United States before and during the temozolomide era.* Journal of neuro-oncology, 2012. **107**(2): p. 359-364.
139. Wakimoto, H., et al., *Human glioblastoma–derived cancer stem cells: establishment of invasive glioma models and treatment with oncolytic herpes simplex virus vectors.* Cancer research, 2009. **69**(8): p. 3472-3481.
140. Mikheeva, S.A., et al., *TWIST1 promotes invasion through mesenchymal change in human glioblastoma.* Mol Cancer, 2010. **9**(194): p. 10.1186.